Surface Engineering of Colloidal Group IV Nanocrystals for Optoelectronics

A THESIS
SUBMITTED TO THE FACULTY OF THE GRADUATE SCHOOL
OF THE UNIVERSITY OF MINNESOTA
BY

Lance Michael Wheeler

IN PARTIAL FULFILLMENT OF THE REQUIREMENTS
FOR THE DEGREE OF
DOCTOR OF PHILOSOPHY

Uwe R. Kortshagen, Advisor

June, 2014

Acknowledgements

This was one hell of a journey. I have many people to thank for their help along the way. Most importantly, I would like to acknowledge my friends and family (you too, Miss Leems). Even when I disappeared into the black hole that often embodies graduate student life, you were always there to provide love, support, and a constant reminder that there are more important things in life than the lab. This thesis is dedicated to all of you. I want to thank my advisor, Uwe Kortshagen, for allowing me the freedom to explore my own ideas and providing me the unique opportunity to frequently travel and present my research. I thank my lab mates, past and present, as well as John Gardner and the rest of the department and university staff for their support in my research endeavors. Finally, I would like to acknowledge the US Department of Energy and the Center for Advanced Solar Photophysics for funding the majority of this work as well as the University of Minnesota and the Doctoral Dissertation Fellowship for funding my final year of research.

Abstract

Colloidal nanocrystals (NCs), often synonymous with "quantum dots," represent a burgeoning class of next-generation optoelectronic materials. The promise of NCs is twofold: (i) Their optical properties are tunable and offer unique opportunities for enhanced energy conversion due to quantum confinement effects. (ii) The NCs can be processed into thin films using cost-efficient roll-to-roll printing techniques for large-scale integration into devices. Taken together, these two attributes enable a new platform for optoelectronic technology where energy-efficient devices can be produced at low costs. There is an array of research efforts to produce NC-based optoelectronic devices such as photovoltaic cells, light emitting devices, and photodetectors.

Much of the recent progress in this direction hinges on the ability to manipulate the NC surface. Conventional solution synthesis yields NCs with ligands bound to metal surface atoms through a labile acid-base complex. The electrically-insulating native ligands are thus routinely exchanged to produce conductive NC arrays for devices integration. Just as surface manipulation has launched metal-based NCs to the forefront of optoelectronic technology, it is the inability to do so with the covalent surface of group IV (germanium and silicon) NCs that has greatly hindered progress. The motivation of this research is to bridge the gap between group IV and metal-based NCs in order to establish an abundant, non-toxic alternative to NCs that contain toxic lead or cadmium. The bridge is built by developing new Si NC surface chemistries, understanding how they interact with molecules, and applying chemical and physical models to uncover the mechanism of NC colloidal stability.

The research begins by developing nonthermal plasma synthesis of Si NCs from a new precursor, silicon tetrachloride ($SiCl_4$). This work builds on previous studies on chlorine-terminated germanium NCs synthesized from $GeCl_4$, which

were observed to form stable colloids without covalent ligand attachment. Synthesis from $SiCl_4$ offers the same flexibility for tuning size and crystallinity as typical silane synthesis but yields a new chlorinated surface chemistry.

Si-Cl surface groups of the NCs are shown to be crucial for achieving the same colloidal stability observed in Ge NCs. It was determined spectroscopically the polarized Si-Cl surface bond renders the surface Si atoms Lewis acidic and capable of hypervalent interactions with Lewis basic molecules. The NCs were thus dispersible in select Lewis basic solvents. Interestingly, these interactions are also shown to be responsible for a reversible "surface doping" effect, which was also explored spectroscopically and by electrical characterization of a thin film device.

The notion of a Lewis acidic surface gave rise to the development of a more robust Si NC surface chemistry. In this work, plasma synthesis that includes diborane is applied. The resulting Si NC surface is then terminated by a classic Lewis acid, boron, which is demonstrated to be an even more versatile chemistry than the Si-Cl surface. These NCs are also used as a model system for uncovering the mechanism of colloidal stability due to these surface interactions with solvent molecules. It is found that conventional theory cannot account for the stability observed, and a simple alternative model is developed. In light of this model, we are able to demonstrate stable Si NC colloids in media that spans hexane to water.

The thesis concludes with a peripheral effort on Ge NCs, a material lacking in maturity even to Si NCs. In this work, the NC surface is modified to enhance the optical properties of the material as opposed to the ability to process the NCs into films from solution. Size-tunable band gap emission is demonstrated for the first time in gas-phase synthesized Ge NCs by applying Grignard chemistry to the Ge-Cl surface groups. The emission is narrower than any previous report, and emission near the bulk band gap of Ge is attained for the first time.

Contents

List of Tables

List of Figures

Chapter 1

Introduction

"Science is the belief in the ignorance of experts."
-Richard P. Feynman

1.1 Perspective

In the last decade, optoelectronic devices have become ubiquitous in everyday life. According to a 2013 poll by the Pew Research Center, 56% of all Americans carry an optoelectronic device in their pocket[12]; we live in the "smartphone era." I will leave it to my sociology colleagues to comment on the social consequences of such a statistic. The bottom line is this: Optoelectronic technology has become an integral part of the way we live.

The promise of research in new optoelectronic materials goes well beyond smartphone technology. Optoelectronics encompass any device that can manipulate and interconvert light and electrical energy. This includes: photovoltaics, photodetectors, integrated optical circuits, lasers, and light-emitting diodes (LEDs). It is these devices that motivate the work contained in this thesis.

The implication for innovative optoelectronic materials is great. For instance, cheap, efficient solar energy will illuminate a path away from the world's

dependence on burning fossil fuels and provide a mobile source of renewable energy. This, in turn, lowers green house gas emissions to counteract the devastation a changing climate can bring. Cheaper, more energy-efficient mobile electronics make them more accessible to the underprivileged and bring education to even the poorest corners of the planet. I paint a grand picture, but efficient use of energy is indeed one of the grandest challenges to mankind today.

Realizing this "utopian" technology age requires a significant paradigm shift in the materials that go into optoelectronics. The ideal optoelectronic material is one that is safe, abundant, inexpensive, and efficient at converting energy. Nanocrystals (NCs), often synonymous with "quantum dots," are uniquely suited for this. This chapter will illustrate the unique qualities of colloidal nanocrystals for optoelectronics, provide a brief overview of the current status of the technology, and finally describe the contribution to this technology that is contained in the remaining sections of this thesis.

1.2 The case for colloidal nanocrystals

The promise of nanocrystals for optoelectronics is grounded in two fundamental attributes: (i) Their optical properties are tunable and offer unique opportunities for enhanced energy conversion, and (ii) The NCs can be processed into thin film devices using technology that dates back to the 15th century.

The enhanced optical properties of NCs is simply a size effect. As a semiconductor is shrunk to scales that approach the exciton Bohr radius of the material, it begins to exhibit quantum properties. That is, it begins to behave more like an atom and less like a collection of atoms. This is due to the electronic wave function of the NC extending spatially beyond the physical volume of the NC. The wave function is thus "confined" to a small volume in space; it is an effect known as "quantum confinement." As a consequence, the electronic structure of a material is transformed from the continuous band of energy states found in bulk materials to more discrete states found in atoms[13].

A smaller NC size leads to a larger separation of quantized states. The optical properties of the NC can thus be tuned by simply changing its size.

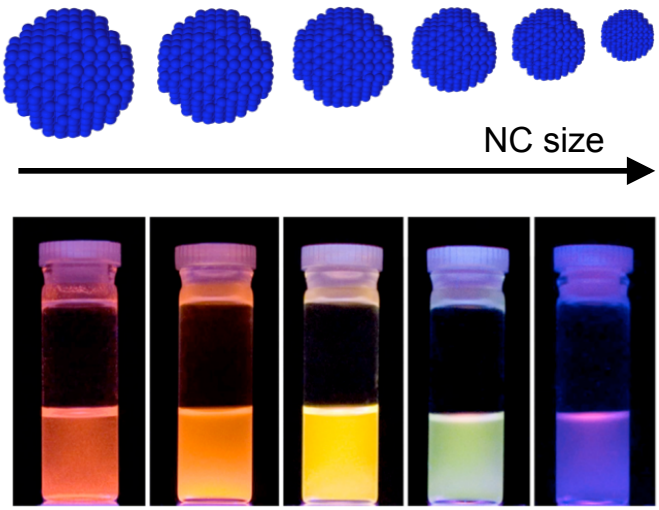

Figure 1.1: **Quantum confinement.** A series of NCs suspended in a liquid. The optical emission observed is dictated by the quantum-confined band gap energy. By decreasing the Si NC size, the optical emission is tuned across the visible spectrum[1].

This effect is nicely illustrated in figure 1.1; NCs absorb high energy blue light and reemit (photoluminesce) light at an energy characteristic to its quantum-confined band gap. It is interesting to note that the NCs displayed are composed of silicon (Si)[1]. Bulk Si has an indirect band gap, and, as a consequence, is an inefficient light-emitter. Light emission is a low-probability multi-particle process (a phonon is needed for radiative recombination of an electron with a hole). When Si is quantum confined, however, quantum yields exceeding 60%[14] have been demonstrated. This is due to the relaxation of crystal momentum conservation (the k quantum number is no longer good)[15,16]. Quantum confinement in Si NCs provides an excellent example of why NCs are interesting for optoelectronics. Efficient, tunable light emission can be achieved in a material that cannot do so in the bulk. It is this effect that today's

commercial technology in displays is built on.

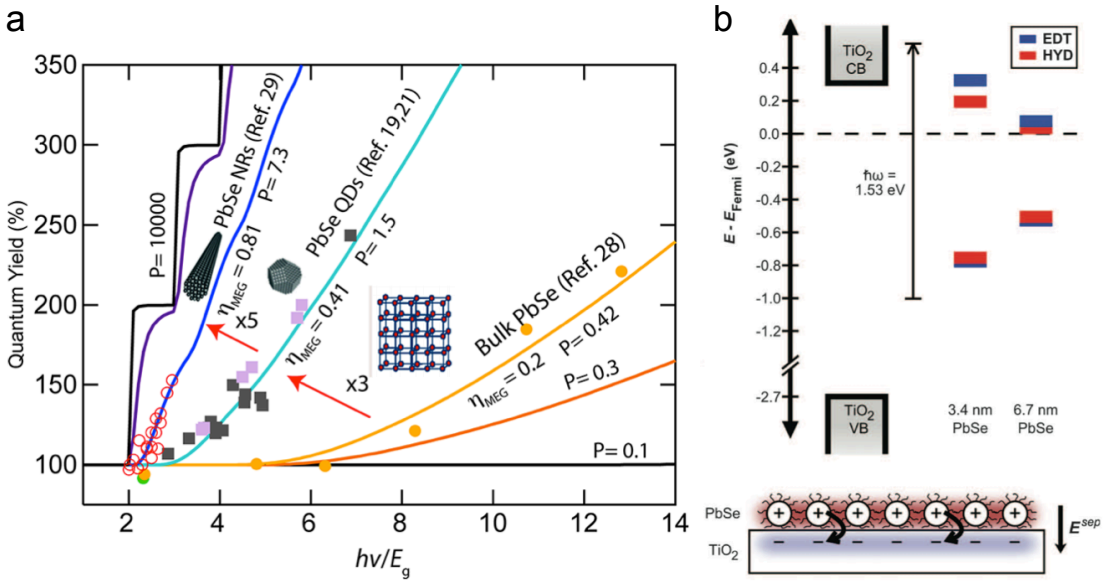

Figure 1.2: **Enhanced energy conversion** Figures extracted from Beard *et al.*[2] and Tisdale *et al.*[3] to represent novel energy conversion strategies that leverage quantum confinement effects by using hot electrons for multiple exciton generation (**a**) or "hot carrier extraction" (**b**).

The discretization of energy states in NCs also leads to additional effects that could make NCs a "game-changer" in photovoltaics. When an electron-hole pair (exciton) is excited by a photon with energy larger than the band gap in a traditional bulk semiconductor, the excited carriers quickly relax (∼1 ps) to the conduction and valence band edges *via* sequential emission of phonons. This thermalization represents a large component of the ∼33% thermodynamic limit on power conversion efficiency of a photovoltaic cell[17]. In the quantum-confinement regime, however, the energy spacing between the quantum energy states can be much larger than the highest phonon frequency of the lattice. This is know as a "phonon bottleneck." The phonon bottleneck thus dramatically slows band edge relaxation of excited carriers (∼1 ns), as the only relaxation mechanism is now a slower multi-phonon emission (Auger

recombination)[18].

The long lifetime of excited carriers has two exciting implications for NC-based photovoltaics: (i) An increased probability of exciting additional excitons, an effect known as multiple exciton generation (MEG) or carrier multiplication (CM)[19], and (ii) the long-lived excited (hot) carriers can be extracted as usable photocurrent before the energy is lost to relaxation - a strategy called "hot carrier extraction." Utilizing either of these strategies boost the theoretical efficiency of photovoltaic cell up to $\sim$66%[20].

Over the course of this PhD, experimental proof for both of these phenomena have been solidified. Figure 1.2a compiles MEG quantum yield measurements for a lead selenide (PbSe)[2]. Additionally, MEG has been demonstrated in CdSe, InAs, Si, InP, CdTe, CdSe/CdTe core/shell NCs as well as in single-walled carbon nanotubes[21]. A similar effect was recently measured in Si NCs embedded in a SiO_2 matrix. Gregorkiewicz *et al.* demonstrated "quantum cutting" where a single high-energy exciton is excited in a Si NC and a second exciton is generated in an adjacent nanocrystal through a similar process to MEG[22,23]. These demonstrations are a significant step toward the realization of photovoltaic devices with efficiencies exceeding the Shockley-Queisser limit[17].

Figure 1.2b highlights work that demonstrated the first ever report of hot carrier extraction[3]. This was again achieved utilizing PbSe NCs by applying a heterojunction with TiO_2. Hot carriers were probed using pump-probe spectroscopy where light is used to both to photo-excite (pump) the NCs and detect (probe) the second harmonic response. This effect was also later demonstrated in the photocurrent of a photovoltaic device based on the "quantum-dot sensitized" architecture[24], but device efficiency improvements are yet to be realized as a result. "Hot carrier extraction," in addition to MEG, nicely demonstrates the promise of NCs as an optical material.

If enhanced optical properties are the fist pillar of NCs for optoelectronics, the cost-efficient processing is the second. From the invention of the solid state transistor in 1947 to the emergence of modern-day Silicon Valley, high quality

electronic materials have required energy-intensive processing. While processing efficiency gains have been made, the semiconductor industry still relies on decades-old batch processes that require at least one of the following: High temperatures, low pressures, or long processing times[25].

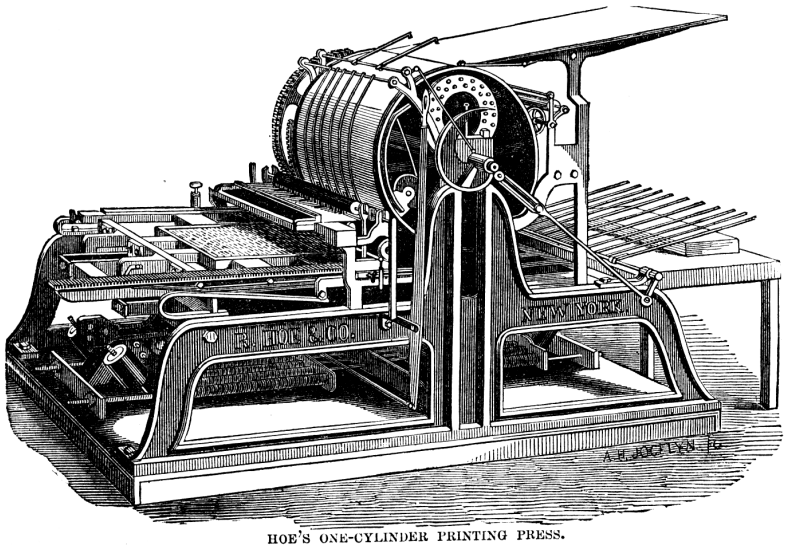

Figure 1.3: **The printing press analogy.** Richard March Hoe's printing press from 1864[4].

In contrast, NCs can be synthesized in solution using common chemistry techniques to obtain a stable colloidal dispersion of increasingly high-quality materials[26]. In essence, the process produces an "ink," that can be printed into optoelectronic devices using an array of inexpensive techniques that have been established over the last six centuries. Figure 1.3 depicts a printing press from 1864. The printing press was invented in 1439 by Johannes Gutenberg. It has come to represent an information revolution, as the written word could be cost-effectively produced in mass quantities. Literacy rates skyrocketed as a result of increased accessibility.

While the printing press analogy is likely infringing on hyperbole, the ability to

print optoelectronics using inexpensive, printing techniques would be a significant paradigm shift away from conventional energy-intensive methods currently used. The result may indeed contribute to a new information revolution where education and the information provided by the internet could be accessed using devices that cost a fraction of what they do now. Realizing this optoelectronic "revolution" is certainly contingent on other technologies—most notably, batteries[27]. Still, the ability to process NCs from solution make them a uniquely promising candidate for next-generation optoelectronics.

Colloidal nanocrystal synthesis has become quite mature, with the ability to precisely control of size[26], shape[28], stoichiometry[29], and doping[30] in addition to the ability to grow heterojunction shells[31]. With synthesis and enhanced energy conversion processes now experimentally validated, much of the recent focus has been on casting the nanocrystals from the colloid into high-quality thin films for device integration. This is truly the heart of this thesis, and the stage will be set in the remainder of this section.

1.3 The current status of nanocrystal optoelectronics

After over three decades of research, nanocrystals have gone from laboratory novelty to a legitimate industry. In fact, this year, 2014, is the first time NCs can be found in displays sold by commercial giants Sony and Amazon. The global market for quantum dots is predicted to reach $2.85 billion by 2018[32].

In these display applications, the NC optical properties are leveraged as down-converting white-light phosphors. Similar areas of research have garnered excitement but are yet to find commercial implementation. For instance, a recent result shows NCs can be effectively applied to large-area solar concentrators by using "stoke-shift-engineered" nanocrystals[33]. This scheme allows for unique integration of photovoltaics into buildings and windows that is

typically not feasible.

Whereas downconversion in displays and solar concentrator applications rely only on efficiently absorbing and reemitting light in isolated NCs, the underlying challenge for the many other applications is to efficiently manipulate electrical charger carriers (electrons and holes) in addition to maintaining optical performance. A central difficulty arises due to ligands at the NC surface. The ligands are composed of a Lewis basic heteroatom bonded to an aliphatic chain. The heteroatom typically binds to the metal atoms of the NC surface, and the aliphatic chain hangs off of the NC in solution where it provides a steric barrier to agglomeration caused by Van der Waals attraction between the NCs. The NCs are thus dispersible in nonpolar solvents. The ligands play a similar role during synthesis, as they are needed for isolating the nucleation and growth sites in addition to a multitude of synthetic controls now established in the community[34]. Unfortunately, the ligands are electrically insulating. Therefore, ligands are needed for synthesis and colloidal stability, but they greatly inhibit charge transport in the resulting films. It would seem ligands are a necessary evil. This predicament is known as "the ligand problem."

In the past six years, the development of ligand exchange strategies has all but solved this issue. In this scheme, native ligands from synthesis are exchanged for shorter, more conductive ones. Initial efforts achieved this in a layer-by-layer strategy during film assembly[35]. Using ligand exchange with 1,2-ethandithiol (EDT), Luther *et al.* were able to establish a new trend line on NREL's iconic Photovolataic efficiency chart with a certified 3%-efficient colloidal nanocrystal solar cell.[36]. This technique has since advanced to the shortest conceivable ligand, the atom[37], and photovoltaic efficiencies have climbed as a result[5]. The current-voltage curve of a record-setting NC solar cell is shown in figure 1.4a. During the short 5-year period of this PhD research, NC-based photovaltaics has improved to a close-to-commercially viable efficiency of 8.2% certified and 8.5% uncertified[38]. Perhaps even more exciting is the first experimental proof of MEG in the photocurrent of a photovoltaic device. Again,

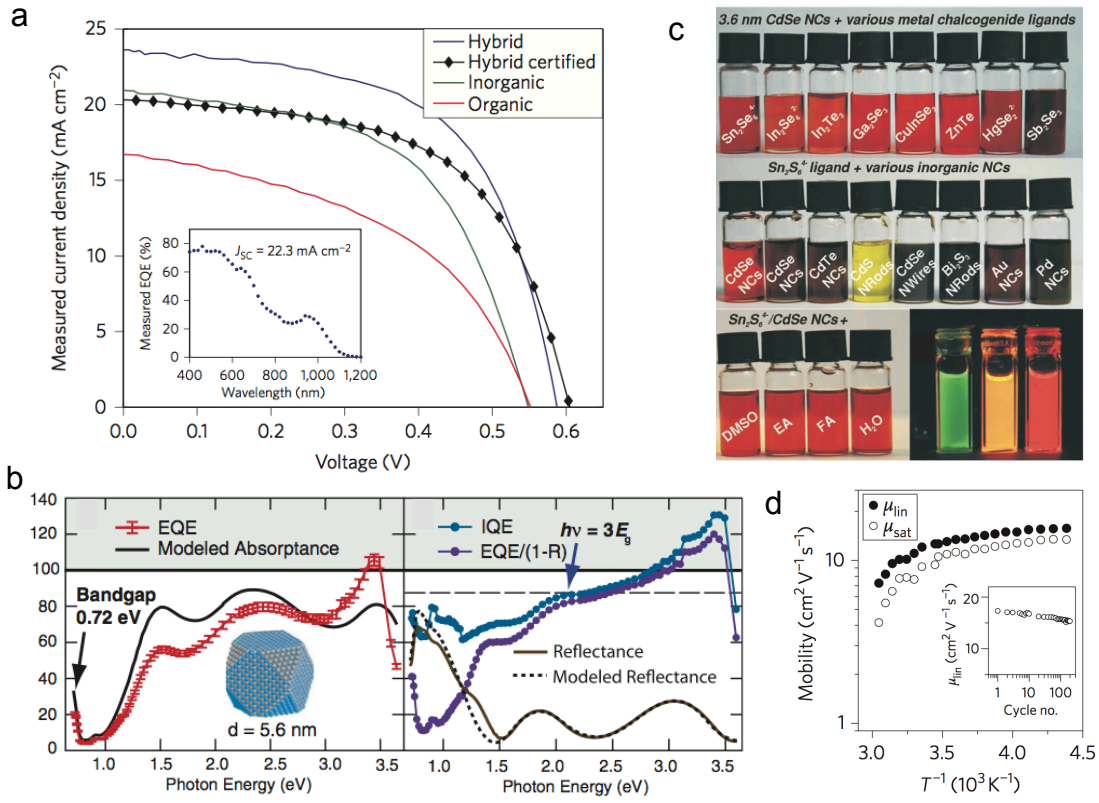

Figure 1.4: **Ligand exchange.** Representative figures compiled from a variety of sources to demonstrate the versatility and value of the ligand exchange strategy for achieving high-performance optoelectronics. **a,** Sargent and coworkers have been continuously pushing the record efficiency of NC-based devices. Here, a 7.0% certified device is shown[5]. **b,** Talapin *et al.*[6] demonstrated ligands can be exchanged in solution to enable direct deposition of conductive thin films. **c,** Ligand exchange in a film and during film assembly lead to the first observation of MEG in a photovoltaic device by exceeding unity in the external quantum efficiency[7]. **d,** Talapin *et al.* later showed that films cast from NCs with solution-exchanged ligands can exhibit band-like transport as shown by the lack of temperature dependance in the mobility plot[8].

this is enabled by ligand exchange with EDT and hydrazine[7]. An external quantum efficiency exceeding unity can be seen in figure 1.4b.

Ligand exchange has inspired a significant body of work in addition to photovoltaic devices. Perhaps most notably, ligand exchange can now be performed while the NCs are still in a colloidal dispersion[6,8,39–43]. The key insight for this development is the use of inorganic "ionic ligands." It has been shown to be incredibly versatile. It is effective for an array of materials with many different ligands. An example of this is demonstrated in figure 1.4c, which is a figure extracted from the original research on molecular metal chalcogenides[6]. With this technique, NCs can be assembled into conductive thin films without any secondary thermal or chemical processing. The ionic ligand can even be chemically tuned to optimize charge transport after film assembly[44].

The films cast from these colloids have indeed demonstrated promising results for electronic transport. In fact, there have now been two reports of band-like transport through a NC film[8,43]. Until now, this was a property found only in bulk materials. A plot of temperature-independant electron and hole mobility is shown in figure 1.4d. Researchers have also shown that high mobilities can be achieved while maintaing quantum confinement[8]. This quite literally represents an exciting new class of materials–the "nanocrystal solid" in which bulk-like transport and quantized optical effects are achieved in tandem.

As impressive progress continues to be made in NC-based optoelectronics, there remains an elephant in the room. The NC systems that have demonstrated the most promising results are also those that rely on toxic and scarce metals such as lead or cadmium. This represents a significant opportunity for alternative materials. In particular group IV NCs are non-toxic and abundant. It is interesting that group IVs have been essentially ignored within the community working on the metal-based NCs just described. Much of this is understandable and is briefly considered next.

1.4 The difficulty of group IV nanocrystals

Group IV NCs, Si in particular, are historically difficult to synthesize. High-quality free-standing Si NCs have yet to be produced using the same solvothermal techniques used for metal-based NCs. This is greatly due to the high crystallization energies needed for a covalent crystal, which exceed what a typical liquid system can endure[45]. When they are synthesized in solution, they are of poor optical quality with optical emission derived from trap states[46] Alternative gas-phase processes employing thermal[47,48] or laser[49] pyrolysis suffer from lack of monodisperse sizes and crystal quality while matirix-embedded NCs[50–52] do not offer the ability to inexpensively solution-process thin films.

Previous work in the Kortshagen group has greatly solved the issue of group IV synthesis using a flow-through, non-thermal plasma technique[53]. It has demonstrated free-standing, monodisperse Si[54], Ge[55], and SiGe[56] NCs of high crystal quality. With a reliable synthetic technique available, efforts toward optoelectronic devices have been undertaken. Each material system, Si and Ge, have unique challenges:

1. The optical properties of Si NCs are now well characterized[1,14,57,58], and significant success has been realized in LEDs using Si NCs as the active material[59–61]. However, these devices do not rely on the Si NC film for transport. A similar effort toward fabricating a photovoltaic device used P3HT, a semiconducting polymer, to enhance charge transport[62]. Overall, research toward achieving a high-quality electronic film of Si NCs has been plagued with difficulties[63,64].

2. The case of Ge NCs is much the opposite. Some success has been achieved in fabricating films with favorable electronic transport properties. Holman *et al.* were able to demonstrate highly conductive films[65] and field effect transistor mobilities that are as high as some of the best performing NC-based solar cells[5,64]. The issue with Ge NCs are their optical properties. While confinement has been demonstrated in their optical

absorption[66,67], an optical device based on Ge NCs of any kind has not been demonstrated. In fact, before the work in this thesis, even photoluminescence had not been observed in Ge NCs synthesized from a nonthermal plasma.

This thesis boasts contributions toward solving both of the issues outlined. High-quality, conductive thin films of Si NCs are enabled by the development of new Si NC colloids, and tunable photoluminescence is demonstrated from Ge NCs. In both cases, issues were resolved by engineering the NC surface.

1.5 Scope of this research

We have now retreated from the global-scale of optoelectronics and arrived at a nanoscale problem. The breadth of the work needed to address this problem is quite large. At a basic level, the knowledge needed in solid-state physics has been covered in the introduction. However, before moving on to original experimental research, there is one short chapter dedicated to original analysis on the differences in surface chemistry between typical metal-based NCs and the group IV NCs explored in this work. This is fundamental knowledge needed for this research.

Yet another component of this research is plasma chemistry. Chapter 3 describes original research on the development of a new precursor for nonthermal plasma synthesis of Si NCs. Silicon tetrachloride ($SiCl_4$) is explored as an alternative to silane, its pyrophoric hydride counterpart. Most of the work is focused on achieving a controlled surface chemistry, but plasma parameters and their impact on crystallinity and photoluminescence from the resulting Si NCs are also briefly discussed. This is unpublished work that laid the groundwork for later investigations on Si NC surface chemistry and colloidal stability.

Chapter 4 is an extensive one. The content is adapted from a publication in Nature Communications[68] entitled: "Hypervalent Surface Interactions for Colloidal Stability and Doping of Silicon Nanocrystals." Ting Chen, Uwe Kortshagen, and Nate Neale, a collaborating chemist at the National Renewable

Energy Laboratory, are also authors on this work. Ting provided electrical characterization of Si NC thin film devices, and Nate contributed knowledge in chemistry and assistance in experimental strategy. The chapter investigates the interaction of Lewis basic molecules at the Cl-terminated Si NC surface using a variety of spectroscopic techniques. We demonstrate these interactions are important for two interesting phenomena—colloidal stability and "surface doping" of Si NCs. Both of these observations are rationalized using a qualitative molecular orbital theory model.

Chapter 5 builds on the initial efforts of chapter 4 to establish NC colloids that circumvent the need for insulating ligands. A similar approach is taken by exploiting a Lewis acidic surface chemistry, but the colloids formed using a boronated Si NC surface trumps what is achievable by the Cl-terminated surface due to the chemical robustness. Moreover, these Si NCs provide the same solution-phase versatility as their metal-based counterparts. This represents an immense step toward an abundant, non-toxic alternative to Pb and Cd-based NCs. These Si NCs are also uniquely suited for investigating the mechanism of colloidal stability that has been observed after metal-based NCs are exchanged for the ionic ligands discussed above. We find the colloidal forces needed for stability are contrary to the mechanism that has been previously invoked and propose an alternative model for achieving NC colloidal stability. Using this model, we demonstrate stable Si NC colloids in media that runs the gamut from hexane to water. A modified form of this chapter will be submitted for publication under the title: "Surface Chemistry and Colloidal Forces for Nanocrystal Stability in Media Spanning Hexane to Water." Uwe Kortshagen and Nicolaas Kramer, who developed the Si NC synthesis in this work, will be a co-authors on the paper. TEM images are also provided by Ting Chen.

Chapter 6 addresses the issue of photoluminescence from Ge NCs. The Lewis acid interpretation of the NC surface remains important. In this chapter, we employ a secondary passivation chemistry to plasma-synthesized Ge NCs. Ge-Cl groups at the NC surface are exchanged for alkyl groups using Grignard

chemistry. The result is a well-passivated Ge NC that demonstrates tunable bandgap photoluminescence. It is only the fourth time this has ever been observed and the first time from Ge NCs synthesized in the gas-phase. In addition to photoluminescence spectroscopy, the surface chemistry, crystallinity, and absorption properties of the Ge NCs are also explored. This work is published in the Journal of Physical Chemistry Letters[69] under the title: "Tunable Bandgap Emission and Surface Passivation of Germanium Nanocrystals Synthesized in the Gas Phase." Uwe Kortshagen and Laszlo Levij are also authors on this work, and much of the credit should be Laszlo's. He took most of the data shown in pursuit of his master's thesis as a visiting student from Eindhoven University of Technology in the Netherlands.

Chapter 2

The Nanocrystal Surface

> "*Tiger got to hunt, bird got to fly; Man got to sit and wonder, 'Why, why, why?' Tiger got to sleep, bird got to land; Man got to tell himself he understand.*"
> -Kurt Vonnegut

2.1 Introduction

As a bulk material is shrunk to the nanoscale, the surface becomes increasingly important in determining its chemical, optical, and electronic properties. Figure 2.1 makes this notion easy to reconcile; a 2 nm diameter particle has ∼60% of its atoms at the surface.

In this section, the nanocrystal surface is discussed with a focus on illuminating the chemical difference between metal-based NCs and group IV NCs. This is knowledge that is lacking in the area of group IV NCs, and it is is critical for progress in optoelectronics. To be clear, we are limiting the definition of group IV to Si and Ge.

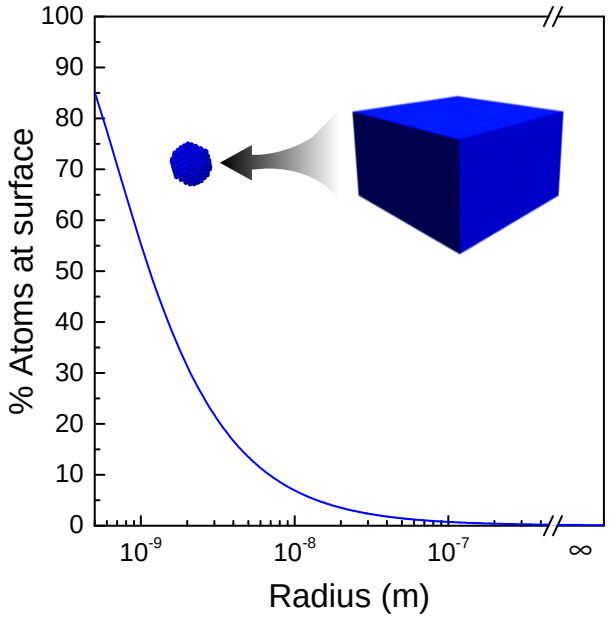

Figure 2.1: **Atoms at the NC surface.**The importance of the NC surface is illustrated with a simple plot of % atoms at a particle surface as a function of radius. A silicon particle is assumed.

2.2 Metal-based versus group IV nanocrystals

There is a fundamental difference between group IV NCs and that of the heavily-researched metal-based NCs. To a first approximation, the difference is easily described using information from any undergraduate general chemistry textbook: Metal chalcogenides and oxides form more ionic bonds, and group IV nanocrystals form more covalent bonds. Certainly this is a general statement. All bonds reside on a spectrum. This is illustrated in figure 2.2. Common bonds encountered for each system are qualitatively labeled on the ionic-to-covalent spectrum. Metals tend to form ionic or polar covalent bonds with oxygen and chalcogens. The more polar bonds reside toward the ionic end of the spectrum. Silicon, on the other hand, bonds with itself to form one of the most nonpolar covalent bonds on the periodic table[70]. More electronegative atoms, such as Cl,

bonded to Si will form a more ionic bonds, but never to the degree that can be achieved by metal-chalcogenide bonds.

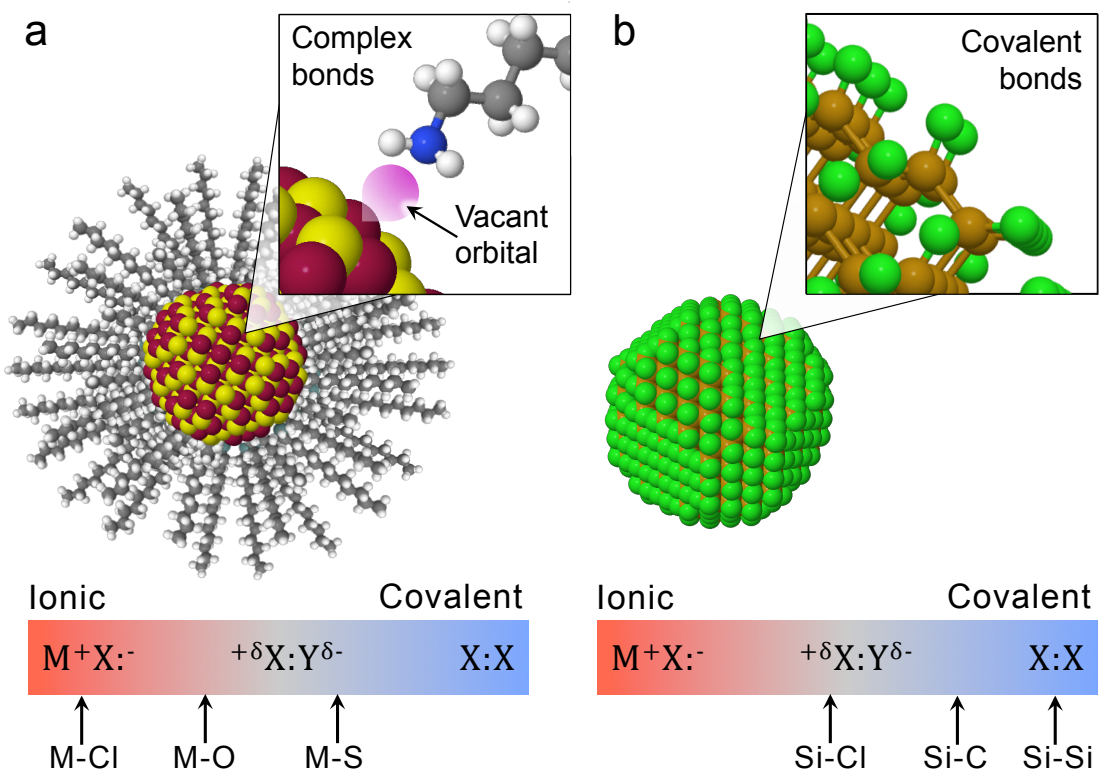

Figure 2.2: **NC chemistry.** A cartoon illustrating the fundamental chemical differences between the metal-based (**a**) and group IV NCs (**b**).

As outlined in the introduction, the surface atoms are the more important distinction for NC systems. In general, metal-based NCs are synthesized in solution with a metal-rich surface as a result[71]. Metal atoms at the NC surface are more cationic, with fewer valence electrons than group IV elements (Pb, of course, is the exception here). The most common cations in metal-based NCs are lead (Pb) and cadmium (Cd), which are much heavier atoms than Si and Ge, so they also have more diffuse vacant orbitals. A metal atom with vacant orbitals at the NC surface is, by definition, a Lewis acid because it is deficient in

electron density[72]. A Lewis base is thus an atom that is rich in electron density and capable of donating it. The general definition of Lewis acid and base is an important concept throughout this work.

Being electron-deficient, the metal surface atoms typically engage in two types of bonds: (i) An ionic complex with the anionic heteroatom of a ligand (these herteroatoms are typically strong Lewis bases), and (ii) a charge-neutral complex with a Lewis basic heteroatom of a ligand[73,74]. A neutral complex between a metal atom and an amine (NH_2) heterogroup is depicted in the inset of figure 2.2a. A similar bonding scheme occurs for trioctylphosphine (TOP) and trioctylphosphine oxide (TOPO), which are also commonly employed for synthesis of metal-based NCs[26]. An example of an ionic complex is found in the common oleic acid ligand, which is deprotonated to form an anionic oleate. The anionic oleate then forms an ionic complex with a metal atom at the NC surface.

Both bonds described will bind aliphatic ligands to the NC surface. The nature of these bonds make them labile and susceptible to exchange chemistry, as the electron density of the bond is donated only by the Lewis basic group of the ligand with little back-bonding from its metal partner[73]. In contrast to a covalent bond, electron density is not shared. The ligand can thus be quickly exchanged by using a stronger Lewis base than the existing ligand (this is used for layer-by-layer assembly of films and "ionic ligand" exchange) or by mass action[75] where the new ligand simply dramatically outnumbers the existing one. This is typically a longer process[76].

The group IV surface is significantly different. When starting from a hydrogen-terminated surface chemistry, it is certainly possible to bond ligands to the Si or Ge NC surface *via* hydrosilylation[14] or hydrogermylation[65], respectively. It is also possible to attach ligands to a chlorinated group IV surface using Grignard chemistry[69]. As a result these NCs form a stable colloid in non polar solvents just as metal-based NCs do. However, group IV NC surface bonds such as Si-C-R[58] and Si-O-R[77] are mostly covalent, which makes them kinetically inert and thus resistant to exchange[78].

In contrast to metal atoms, it is quite difficult to engage in non-covalent bonding schemes in group Si and Ge atoms. In general, Si is more difficult, as it is a tightly bound atom with no *d*-orbitals. *d*-orbitals are often involved in non-covalent bonds as in those described for metal atoms above. It is, however, possible for Si to engage in a fifth, or "hypervalent," bond in which electron density is donated from a Lewis base partner. This is only possible when it is bonded to an electronegative atom to withdraw electron density away from it. Halogens are typically used. The fifth bond is characterized as a three-center four electron bond. In this case, electron density from a donating Lewis base is shared by three atoms, the donor atom, the electron-defficient Si atom, and an adjacent atom[79]. These concepts were developed for molecular chemistry, but they extend to the NC surface as well[80]. Hypervalent interaction between Si-Cl groups with donor molecules is well-estabilished in synthetic organosilicon work[81].

The distinction between covalent and ionic typically becomes blurry going down the columns of the periodic table. Ge is thus more likely than Si to engage in non-covalent bonds and remains more stable whereas carbon is known not to do so at all[82]. When a hypervalent bond occurs, peripheral bonds are affected in accordance to "Gutmann's rules," which describes the redistribution of electron density after a Lewis acid-base bond occurs. The peripheral bonds are lengthened and shifted toward a more ionic-type bond, as seen in the spectrum in figure 2.2. As the strength of the donor increases or the number of hypervalent bonds increases, peripheral bonds elongate and become more unstable. This can lead to the formation of an inner sphere ionic complex. Unfortunately, these bonds thus become very reactive and susceptible to hydrolysis.

2.3 Conclusion

It is clear from these insights that the group IV NC surface is much different than its metal-based counterpart. High-quality optoelectronic films are cast from

stable colloids, but, with the exception of a few instances that are not understood[83,84], stable group IV colloids have only been achieved after aliphatic ligand attachment. Since this ligand cannot be exchanged for the reasons outlined above, films cast from these colloids are unavoidably resistive. Achieving a stable NC colloid without a ligand is a logical route to circumvent this issue. Efforts in this direction are the basis of chapters 4 and 5.

Chapter 3

Plasma Synthesis of Nanocrystals

> "*One man's 'magic' is another man's engineering. 'Supernatural' is a null word.*"
> -Robert A. Heinlein

3.1 Introduction

Plasma synthesis of NCs has emerged as a promising alternative to conventional solution-based routes[53]. In contrast to solution synthesis, it is a scalable, flow-through scheme capable of high production yields. It is able to produce high-quality, organic-free NCs without wasteful use of liquid chemicals. Undoubtedly, the most important two features of this method are the ability to crystalize group IV NCs and produce them with a fairly narrow size distribution (within ∼15% of the mean). Both of these attributes arise due to the unique chemical environment of a nonthermal plasma, which are summarized in the following:

1. The plasma is a highly non-equilibrium (nonthermal) environment. Though the gas temperature of the plasma remains relatively close to room temperature (∼300-600 K), the electrons are extremely hot (∼30,000-50,000 K) and lead to dissociation of gaseous precursors. Highly

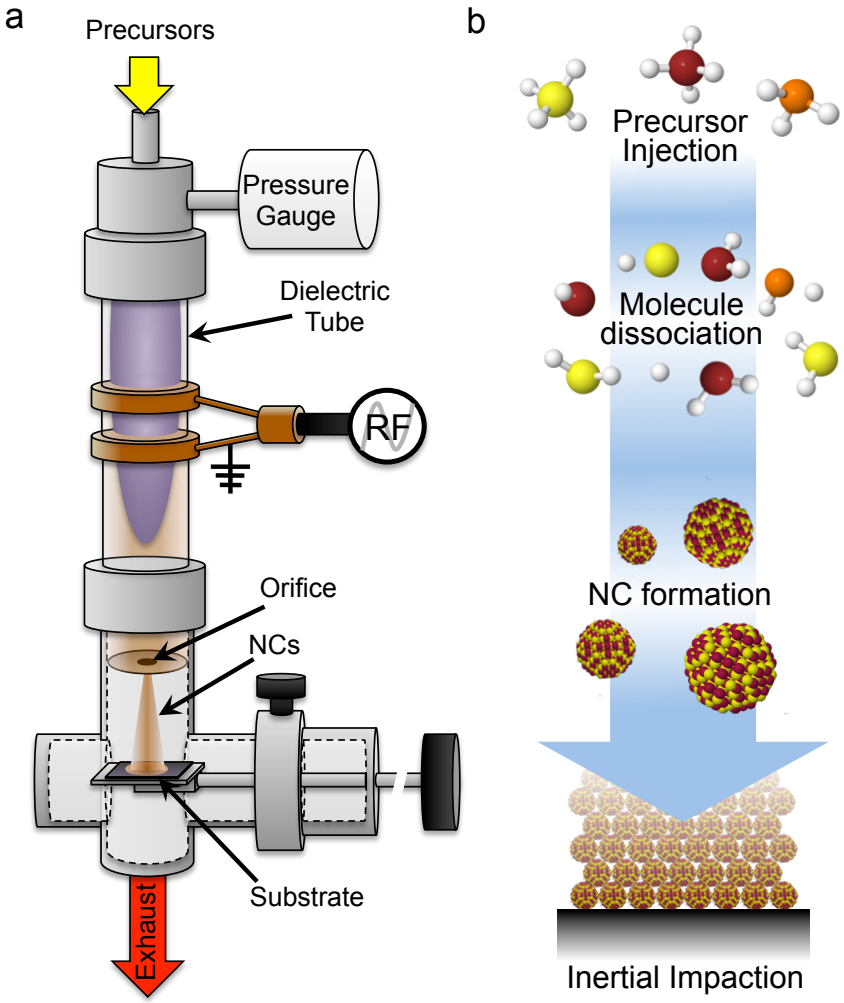

Figure 3.1: **The plasma reactor. a**, A cartoon schematic of the reactor. **b**, The process of gaseous precursor injection and decomposition, NC formation, and NC film impaction.

exothermic reactions at the NC surface, such as electron-ion recombination, lead to selective particle heating and crystal growth[85,86].

2. The electrons in the plasma have much higher mobility than the ions. Consequently, the Si NCs, as well as the reactor walls, obtain a unipolar negative charge[87]. Electrostatic repulsions allow for Si NCs to grow without agglomeration resulting in narrow size distributions[88,89]. This feature distinguishes nonthermal plasmas from other gas-phase routes which yield a much wider size distribution[47–49].

Figure 3.1a shows a cartoon schematic of the plasma reactor as well as a generic representation of NC formation in figure 3.1b. Before this work, group IV synthesis was limited to SiH_4[54], GeH_4[56], and $GeCl_4$[55] precursors. Here we investigate $SiCl_4$ in order to a achieve a Cl-terminated Si NC surface. Synthesis from $SiCl_4$ was reported from a previous member of the Kortshagen research group at the same time as this work.[90].

3.2 Nanocrystals from silicon tetrachloride

This work was inspired by Ge NCs synthesized from $GeCl_4$. It was serendipitously observed that Ge NCs synthesized from $GeCl_4$ could form a stable colloid in select solvents without the need for ligand attachment[83]. While not fully understood at the time, it is an exciting result. Rutherford backscattering in addition to chemical etching experiments shows a significant amount of Cl on the Ge NC surface, and it was hypothesized that a Cl-terminated Ge NC surface played a significant role in colloidal stability. Synthesis of Si NCs from $SiCl_4$ was explored with the hope to extend this observation of colloidal stability to Si NCs.

Plasma conditions were adapted from Ge NC synthesis[55] in which a flow of H_2 is included with $SiCl_4$ to serve as a reducing environment. Figure 3.2a shows Raman spectra from Si nanoparticle samples synthesized using this chemistry. At 150 W nominally applied power, a shoulder at 521 cm^{-1} begins to emerge. This

is the optical phonon vibration of crystalline Si[91]. This peak is highlighted in yellow in figure 3.2a. As power is increased, this peak becomes more prominent, and the lower energy peaks, due amorphous Si material, decrease correspondingly. Figure 3.2b shows an X-ray diffractions (XRD) spectrum from the Si NC sample synthesized using 175 W nominal power and impacted onto a glass substrate. The NCs exhibit peaks corresponding to diamond cubic Si. Scherrer broadening analysis by fitting the peak with a Gaussian and Lorentzian curve reveals Si NCs that are ∼8 nm in diameter.

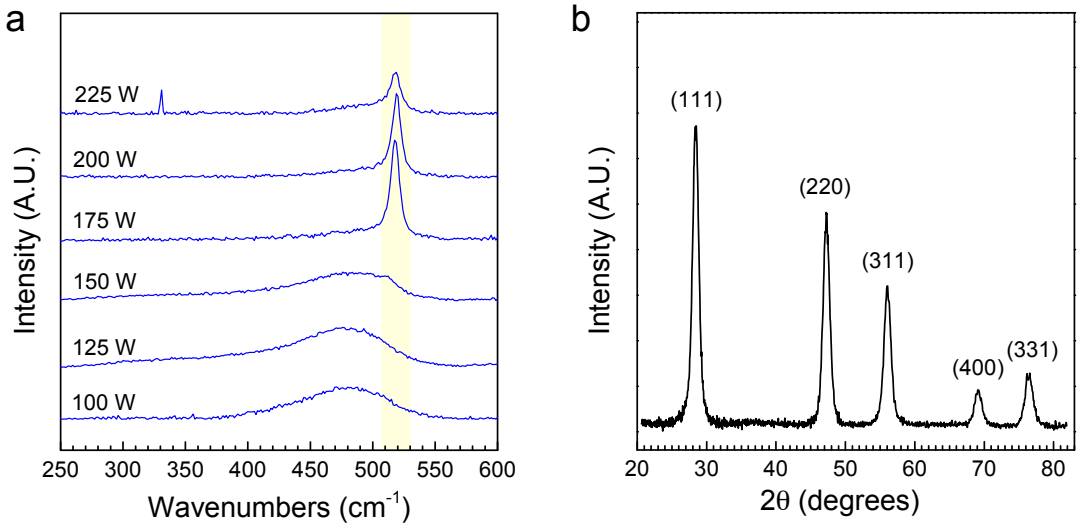

Figure 3.2: **Crystalline Si NCs from $SiCl_4$.** **a**, Raman spectra of Si NCs synthesized using a range of nominal input powers. **b**, An example of a XRD spectrum from a crystalline Si NC sample.

The ability to tune the size of the Si NCs using plasma residence time was achieved as one would expect from previous reports[53]. With a focus on surface chemistry, little time was dedicated to investigating this effect. However, optimal plasma conditions for residence time size control of the Si NCs was investigated by Gresback *et al.*[90].

3.3 Silicon nanocrystal photoluminescence

Here we demonstrate an interesting effect by using plasma power to control Si NC size and investigate the resulting photoluminescence (PL) properties of the Si NCs. Figure 3.3a shows a photograph of Si NCs impacted onto a glass substrate with successively increased power applied to the plasma. The first spot at the bottom of the photograph corresponds to 80 W, and every two subsequent spots represents a power increase to 90, 100, 120, 140, and 160 W. In figure 3.3b, visible PL is observed when the NC samples were illuminated with ultraviolet (UV) light.

Si NCs synthesized at 90 W do not show visible signs of PL. However, the remaining samples emit after exposure to ambient oxygen and water for >2 hours. Samples synthesized at higher power emit at a bluer energy than the sample before it. It appears the increased power etches the Si NCs to yield a smaller size. The observed PL is the expected trend for quantum confinement effects on the Si NC band gap. It is important to note the existence of PL validates that no oxygen is in the core of the crystal, only on the NC surface, as oxygen in the core would lead to high-energy emissive defect states or quenched PL[92].

The NC emission could be tuned from red (∼850 nm) to yellow (∼550 nm). However, NC mass yield decreased dramatically at higher powers. This can be seen in figures 3.3a and b, as the spot corresponding to the yellow-emitting Si NCs synthesized at 160 W is much smaller though deposition time remained the same. This is again attributed to etching effects, as Cl is well-known to etch Si[93], and is likely the reason for decreased yield. The yield is so small that the sample is invisible to the naked eye until UV light illuminates it (figure 3.3b). This is an encouraging result for downshifting films for photovoltaic and display applications.

For photovoltaic applications, a downshifting film should selectively absorb UV and high-energy visible light, where the solar cell is an inefficient absorber, and allow visible light to pass through. The high energy light absorbed by the NC film is then reemited at a wavelength that is efficiently absorbed by the solar cell.

The result is a higher power conversion efficiency, as more sunlight was utilized. In figures 3.3c and d, we demonstrate an optically transparent film that aborbs high energy light and downshifts it to red, a region of strong absorption in a typical solar cell. This film was deposited by simply rastering the substrate under the beam of NCs accelerated through the orifice of the reactor. Film thickness is thus controlled by the number of times the substrate is rastered.

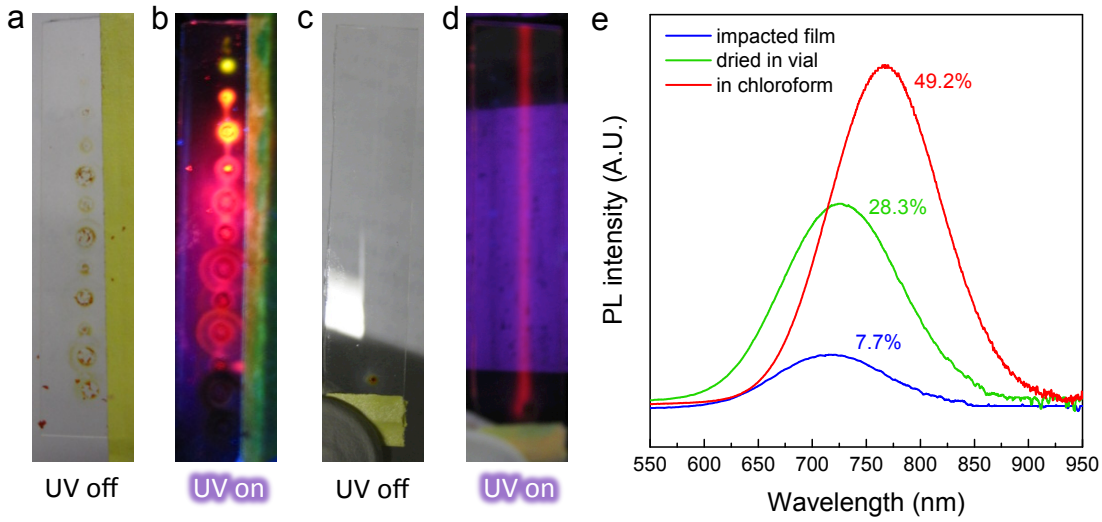

Figure 3.3: **Photoluminescence from Si NCs synthesized from $SiCl_4$. a**, Si NCs deposited onto a glass substrate using various plasma powers. **b**, The same Si NCs exhibiting visible PL under UV illumination. **c** and **d** show a simlar effect for an optically-transparent thin film of Si NCs impacted on to a glass substrate. **e,** Photoluminescence intensity as a function of wavelength for three samples: Si NCs that were suspended in chloroform and allowed to oxidize for ∼2 hours (red), the same Si NCs after two days of oxidation (green), and Si NCs deposited in a film and allowed to oxidize for two days (blue). Percentages next to PL spectra correspond to PL QY of the sample

The NCs need to be oxidized before PL is observed. This is likely due to a trap-passivation phenomenon that has been previously observed in fluorine-etched Si NCs[94]. The PL quantum yield (QY) was evaluated for oxidized NCs synthesized at 120 W. The first sample was synthesized and

immediately dispersed in chloroform. The PL spectrum of this sample is shown in red in figure 3.3e after allowing the NCs to oxidize for ∼2 hours. The PL QY of this sample is 49.2% with a full width at half maximum (fwhm) of 120 nm. A PL QY this high is typically only observed in Si NCs synthesized from silane and subsequently passivated using hydrosilylation to attach alkane ligands[14]. However, F-etched Si NCs show a similar result[95]. The halogen is hypothesized to assist in forming a "soft" oxide, which better passivates the NC[94].

After allowing the NCs to oxidize for a ∼48-hour period, a blueshift is observed, which is consistent with a smaller Si NC diameter due to oxide shell growth. The PL QY of the NCs has also decreased to 28.3%. The full width at half maximum remains at 120 nm. The spectrum can be seen in green in figure 3.3e. It is interesting to note that the PL QY is still 4× greater than that of a film synthesized at the same time but impacted onto a substrate and allowed to oxidize (blue spectrum, figure 3.3e). It is likely that NCs remaining relatively isolated from one another can grow a uniform shell and better passivate the NC. In contrast, oxygen and water need to penetrate into the thin films of Si NCs, which means NCs at the bottom of the film may not be as well passivated as NCs at the top of the film. This is a likely rationale for the PL QY of 7.7% observed in the impacted film.

3.4 Surface chemistry control

This work was designed to achieve a Cl-terminated Si NC surface chemistry. Intuitively, decomposition of $SiCl_4$ in the presence of H_2 should yield a surface that can be terminated with both chloride groups as well as hydride groups. Initial synthesis efforts yielded a surface that was considerably oxidized. This is clearly observed in figure 3.4a showing a Fourier transform infrared spectrum (FTIR) spectrum of an Si NC sample. Oxidation is manifested as the broad O-H peak centered at 3350 cm^{-1} and the O_2Si-Si-H and O_3-Si-H bonds around 2255 cm^{-1}. A prominent Si-O-Si stretching mode also emerges at 1090 cm^{-1}.[96]

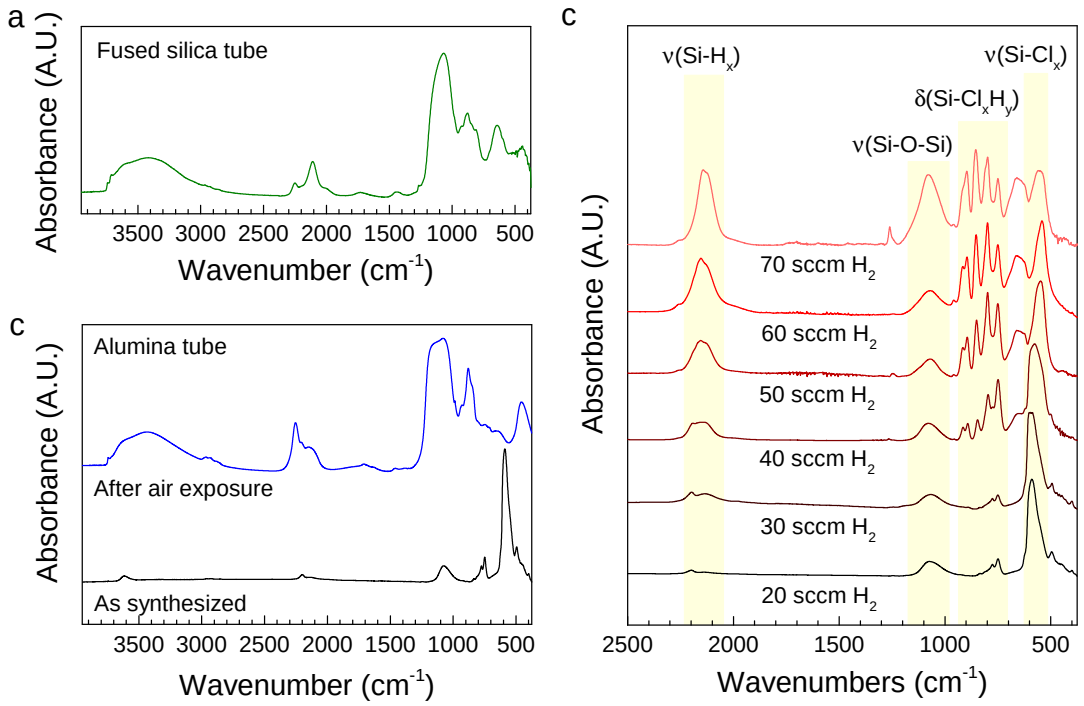

Figure 3.4: **Si NC surface chemistry control.** **a**, FTIR spectrum of Si NCs synthesized using a fused silica tube. **b**, FTIR spectra of Si NC synthesized from an alumina tube (black), and the same NCs after being exposed to ambient air (blue). **c**, FTIR spectra of Si NCs synthesized at constant total pressure but with varying H_2 flow. Spectra are normalized to the most intense peak and offset for clarity.

Care was taken to ensure no ambient air exposure to the sample. NCs were synthesized in the plasma reactor and transferred air-free to a N_2-purged glovebox for characterization, alternative sources were investigated. Cl plasmas are well-known to etch SiO_2[97], which could lead to *in situ* oxidation of Si NCs during synthesis. Alumina is often used as an etch-resistant barrier in semiconductor processing[93]. Indeed, switching to a high-purity alumina tube for synthesis dramatically decreased evidence of oxidation and indicates oxidation had occurred during synthesis. This is shown in the nearly-pristine IR

absorption spectra shown in black in figure 3.4b. The Si-Cl_x stretching modes between 520cm^{-1} and 580cm^{-1} have now gained prominence[98]. The blue spectrum is the same sample after air exposure. The NCs quickly oxidize and take on the spectral features of figure 3.4a. This is consistent with previous reports[99] in which a chlorine-enhanced Cabrera-Mott oxidation mechanism is invoked.

Hydrogen can be incorporated onto the NC surface by simply varying the ratio of $SiCl_4$ to H_2. The reaction pressure is kept constant by adjusting Ar flow. Figure 3.4c focuses on the lower energy region of the spectrum where modes due to Si-Cl and Si-H dominate the spectrum. There is a clear trend observed. Increased H_2 flow leads to more hydride groups and fewer chloride groups on the surface. A condition that removes all Cl from the surface was never obtained. Unfortunately, Si NC mass yield decreased with increasing H_2 flow. NC size also decreased with increasing H_2 flow. It is thus difficult to decouple surface chemistry from other important Si NC characteristics by simply changing one plasma parameter.

3.5 Conclusion

It is clear that the $SiCl_4/H_2$ plasma is a dynamic chemical environment with competing mechanisms of etching and particle nucleation and growth. This is certainly the case in comparison to the more heavily-used silane chemistry. In this work, Si NC synthesis was demonstrated and plasma-dependant etching effects were investigated using PL spectroscopy. Si NC surface chemistry was also systematically investigated. After achieving a Cl-terminated surface that was sufficiently free of oxide, many of potential avenues for investigation into synthetic chemistry were not undertaken in order to explore colloidal stability of these NCs. This leaves a significant opportunity for research (see below). The route taken in this work also proved fruitful. The ability to control the surface chemistry of the NCs is found to be critical for achieving stable colloids of Si NCs without covalent ligand attachment. The following chapter will discuss, in

detail, the role of chlorine at the NC surface for colloidal stability in addition to an unexpected surface doping effect.

3.6 Experimental methods

Plasma conditions. Si NCs shown in the raman and XRD spectra are synthesized by flowing 30 standard cubic centimeters (sccm) of argon, which serves as a dilution gas, 40 sccm of H_2, and 2 sccm $SiCl_4$. The reactor pressure was 2.5 torr, which is controlled by an orifice downstream of the plasma. A plasma is struck by applying power at a frequency of 13.56 MHz to a pair of ring electrodes wrapped around a 2.54 cm outer diameter (OD) and 2.23 cm inner diameter (ID) fused silica tube. The nominally applied power is increased until a crystalline sample is achieved. Si NCs for PL measurements were synthesized by flowing 0.5 sccm $SiCl_4$, 40 sccm H_2, and 30 sccm Ar. The pressure in the reactor was 2.5 Torr. The same silica tube is used. Applied power was varied from 80 W to 160W. Each spot in figure 3.3a and b represents two minutes of deposition. Si NCs for surface chemistry investigation were synthesized by flowing $SiCl_4$, 20 to 70 sccm H_2, and between 0 and 40 sccm Ar. The pressure is kept constant at 2.5 torr. An alumina tube with a 1.90 cm OD and 1.27 ID was used, and applied power was varied from 120 W to 250W where higher powers were needed in the more H_2-rich plasmas.

FTIR. FTIR experiments were done in diffuse reflectance infrared Fourier transform (DRIFT) mode using a Bruker Alpha FTIR spectrometer inside a N_2-atmosphere glovebox. Spectra were typically collected by averaging 24 scans at 2 cm^{-1} resolution. Samples were prepared by directly impacting Si NCs onto a gold-coated silicon wafer.

X-ray diffraction. XRD was performed on Si NCs impacted onto a glass substrate using a Bruker-AXS microdiffractometer with a 2.2 kW sealed Cu

X-ray source. The Si NC diameter was calculated from the Scherrer equation using Jade 8.0 software.

Raman spectroscopy. Si NCs impacted onto a glass substrate were illuminated with an Omnichrome argon ion laser with 514.5 nm excitation and 50 mW maximum output power. Spectra were collected with a Witec alpha300 R confocal Raman microscope, UHTS300 spectrometer, and DV401 CCD detector.

PL spectroscopy. PL measurements were carried out using an Ocean Optics, Inc. USB2000 spectrometer equipped with an integrating sphere. The excitation source was a 395-400 nm light-emitting diode. The quantum yields are calculated by dividing the integrated peak areas of LED absorption by the Si NC emission peak. The PL QY displayed in figure 3.3a is the mean of three measurements.

3.7 Future work

This work is certainly not complete. The large parameter space of power, pressure, and $SiCl_4$-to-H_2 ratio was not rigorously explored. It would be illuminating to determine etching-dominant and NC growth-dominant regimes. It could yield an interesting phase diagram that could include mass yield, surface chemistry, and NC size as a function of these three parameters. PL dependence on these properties could also be corroborated for a complete study. Some of this has been covered by other groups[90,100], but surface chemistry dependance has not been explored throughout the parameter space.

Investigation of PL from oxidized Si NCs could be an interesting endeavor. The properties will be important to explore for downshifting applications in photovoltaics and displays. For example, the effect of oxidiziing Si NC while

individually isolated would be an interesting study. It is likely that isolated NCs allowed to oxidize in solution and then cast into a film would have better properties than a film of NCs that is left to oxidize. This could be studied using the Si NC colloids outlined in the following section.

While attempting to achieve smaller NCs with a high degree of chlorination, it was also found that higher order chlorosilanes could be produced in the gas phase when $SiCl_4$ is decomposed with a deficient amount of H_2. The chlorosilane molecules were polymerized to such a degree that they condensed in $\sim$10 mTorr vacuum. Unfortunately this intriguing material was never explored, but it could be quite interesting as a material that could be cast into a film and annealed to produce low-cost amorphous or polycrystalline silicon.

Chapter 4

The Chloronated Silicon Nanocrystal Surface

"*We live to survive our paradoxes.*"
-Gordon Downie (The Tragically Hip)

4.1 Introduction

Quantum confinement effects make semiconductor nanocrystals (NCs) particularly interesting at diameters approaching or below the exciton Bohr radius. Processing these materials from colloidal solutions enables roll-to-roll, large-area deposition of NC thin films for optoelectronic devices such as solar cells[101], light-emitting diodes[102], and photodetectors[103]. Typical NCs have an exciton Bohr radius on the order of 10 nm or less. Colloidal stability becomes exceedingly difficult at this scale, as Brownian motion becomes dominant and leads to NC agglomeration[104]. A steric barrier to agglomeration from long-chain organic ligands at the NC surface is typically employed to overcome this difficulty[26]. Ligand-capped NCs are solvated in non-polar solvents and will self-assemble into highly-ordered thin films[105]. However, the organic ligands dramatically hinder charge carrier transport in the films[35,106]. For the

extensively-studied metal chalcogenide NCs, this problem is routinely solved during film assembly by chemical exchange of the original ligands for shorter organic[35] or inorganic[37] ligands.

Talapin and coworkers have pioneered an alternative strategy in which insulating organic ligands are exchanged in solution for conductive molecular metal chalcogenide (MMC) complexes[6,39] or metal-free inorganic ions[40]. Conductive films can thus be assembled directly from solution. This strategy represents a second viable mechanism of NC colloidal stability based on electrostatics where the negative charge of the ionic surface species imparts stability in polar solvents.

After deposition of a conductive NC film, control of the optoelectronic properties is paramount to device performance. In bulk semiconductors, this is achieved by doping–the controlled addition of atomic impurities into the crystal lattice. This has proven challenging at the scale of confined NCs. Statistical, thermodynamic, and kinetic arguments have been employed to rationalize the difficulty of incorporating dopant atoms into NCs[107], and practical implementation of doped NC films has remained elusive.

We confront the issues of thin film ligand removal as well as doping of NCs by applying the framework of generalized Lewis acid-base theory[108] to the silicon (Si) NC surface. Silicon normally bonds with four atoms to complete its outer shell octet. However, polarization of electron density away from the Si atom renders it Lewis acidic and capable of engaging in pentavalent and even hexavalent bonds[79,109]. Though this phenomenon is well known to occur in molecular analogs, for the first time we demonstrate its significant potential when applied to the surface of a NC. This is achieved by first terminating the Si NC surface with chlorine (Cl) to polarize electron density from Si surface atoms. The Lewis acidic Si-Cl surface groups facilitate hypervalent interactions with hard donor (Lewis base) molecules. In a series of experiments, we show this interaction is responsible for colloidal stability by ruling out previously-demonstrated steric[26] and electrostatic[6,39,40] mechanisms. In parallel,

the observation of free carrier absorption in the Si NCs upon contact with the donor molecules further validates the interaction as hypervalent in nature and illustrates a new method for reversible molecular doping of NCs.

4.2 Donor molecules and the silicon nanocrystal surface

Nonthermal plasma synthesis has proven to be highly successful in the production of group IV NCs when compared to colloidal methods due to the high crystallization energies needed[54]. It also allows for surface chemistry control. In this work, a Cl-terminated surface is achieved via decomposition of $SiCl_4$ vapor in the presence of H_2 in a nonthermal plasma reactor.

Addition of an appropriate hard donor solvent to a vial containing Cl-terminated Si NCs yields an optically transparent colloidal solution after slight agitation by simply shaking the vial until a maximum concentration is reached. The process of colloid formation can be seen in a video supplied as supplementary information to the publication[68]:

nature.com/ncomms/2013/130729/ncomms3197/extref/ncomms3197-s2.mov

Dynamic Light Scattering (DLS) on the Cl-terminated Si NCs solvated in 2-butanone, shown in Fig. 4.1a, confirms the Si NCs are un-agglomerated with a single-particle population at 10 nm in diameter. Figure 4.1b shows transmission electron microscopy (TEM) images of highly monodisperse 8 nm Si NCs cast from a benzonitrile solution. The crystal diameter is in agreement with Scherrer broadening of the x-ray diffraction spectrum and the 10 nm diameter observed in the DLS spectrum, which includes the solvation layers that surround each NC. Evidence of ordering and lack of agglomeration in the NC monolayer of figure 4.1b also illustrates NCs are stabilized in solution. As expected for a stable solution[105],

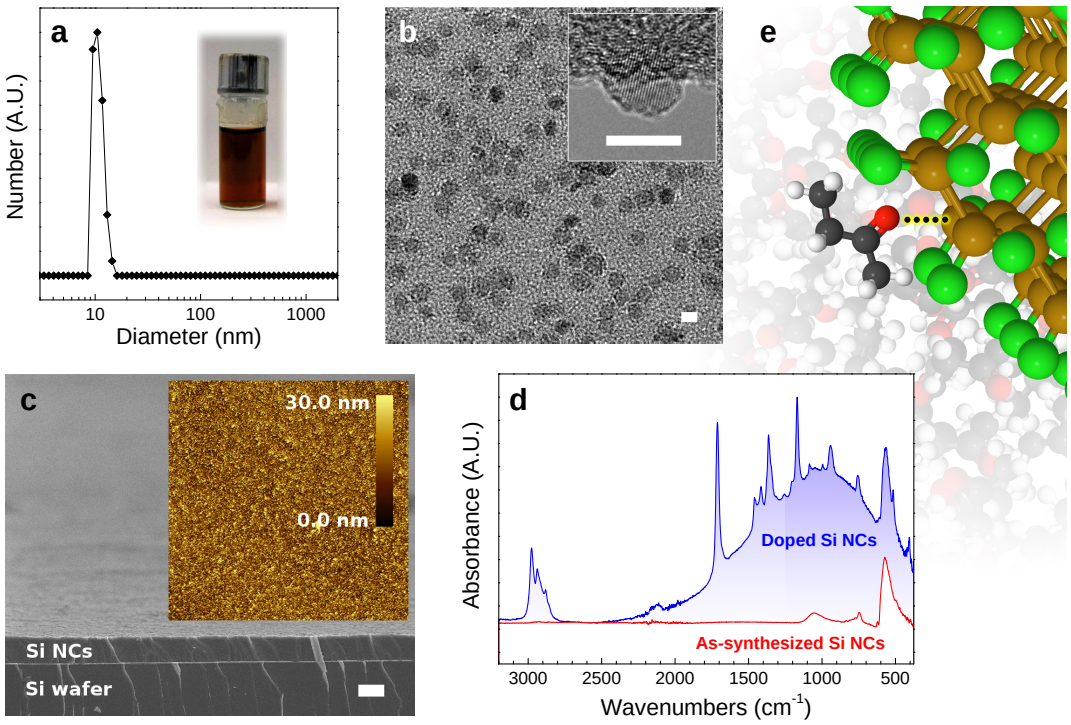

Figure 4.1: **Colloidal stability and doping of Si NCs.** Si NCs synthesized without ligands immediately form a concentrated solution when dispersed in hard donor solvents as 2-butanone (**a**, inset). **a**, DLS spectrum showing a single-particle population of Si NCs in 2-butanone with a diameter of 10 nm, which indicates a solvation shell of 2 nm when compared to TEM (**b**). Single particle solvation is also validated by the 2-dimensional ordering observed in TEM (**b**). Scale bars in **b** are 8 nm. SEM demonstrates device-quality films are attained by drop-casting from these stable colloids (**c**), and SPM (inset) shows films are continuous over large areas with a root mean square roughness of 8.4 nm. The scale bar in **c** is 2 μm, and the SPM area is 50 μm $\times$ 50 μm. **d**, ATR-FTIR spectra depicting as-synthesized Si NCs (red) and Si NCs in the presence of 2-butanone (blue). The broad absorption centered at 1000 cm^{-1} is attributed to free carrier absorption due to hypervalent interactions at the Si NC surface. **e**, A cartoon depiction of this hypervalent interaction between a 2-butanone molecule and a Si-Cl group of the Si NC surface.

the Si NCs self-assemble into device-quality films. Figure 4.1c shows a scanning electron microscopy (SEM) image of a film assembled by drop-casting a 5 mg/ml solution of Si NCs in 2-butanone onto a gold-coated Si wafer. Scanning probe microscopy (SPM) shows films are crack-free and continuous over large areas with a root mean square roughness of 8.4 nm (Fig. 4.1c, inset).

Solvents that provide colloidal stability also exhibit evidence of doping in the attenuated total reflectance Fourier transform infrared (ATR-FTIR) spectrum upon contact with the Si NCs. An example of this is shown in figure 4.1d. The Si-Cl_x stretching mode at 575 cm^{-1} is the dominant feature of the IR spectrum of the as-synthesized Si NCs (Fig. 4.1d, red). After adding 2-butanone to the Si NCs, additional sharp features are observed due to molecular vibrations of 2-butanone, and a broad free carrier absorption centered at 1000 cm^{-1} is also present (Fig. 4.1d, blue).

The observed colloidal stability, as well as free carrier absorption, is indeed dependent on Si NC surface chemistry. For control experiments, we synthesized Si NCs from silane to ensure the production of Si NCs with a fully H-terminated surface[58]. We found H-terminated Si NCs to be insoluble in most solvents, but dilute solutions may be obtained by prolonged sonication, which is consistent with previous work[84,110]. Moreover, no free carrier absorption is observed upon interaction with hard donor molecules.

Solvent choice is also important. A number of solvents were used in this study, and colloidal stability was achieved in a variety of donor solvents. A representative list, along with common solvent scales, is compiled in Table 4.1[111–113]. This concept will be expanded on in the discussion section.

Table 4.1: **Solvent characteristics for NC colloidal stability and doping.** Various solvent characteristics are investigated to rationalize Si NC colloidal stability observed.

Table 1 | Solvent characteristics for colloidal stability and doping of Si NCs.

Solvent	ε_r*	μ†	E_T (30)‡	π*§	pK_{BH}‖	DN¶	$-\Delta H_{BF_3}$#	Stability
Ketones/aldehydes								
Acetone ($n=0$)	21.36	2.88	42.2	0.71	1.18	17.03	76.03	Yes
2-Butanone ($n=1$)	18.85	2.78	41.3	0.67	1.22	17.43	76.07	Yes
2-Pentanone ($n=2$)	15.38	2.74	41.1	—	1.17	17.50	76.19	Yes
2-Hexanone ($n=3$)	14.56	2.69	40.1	—	1.18	—	74.60[21]	Yes
Cyclohexanone	16.02	3.06	39.8	0.76	1.39	17.79	76.36	Yes
Acetophenone	18.18	3.05	40.6	0.90	1.11	15.00	74.52	Yes
Benzaldehyde	17.85[22]	—	—	—	0.78	—	74.88	Yes
2,3-Butanedione	4.71[22]	0.00	—	—	—	—	—	No
Phosphine oxides								
TOPO/TOP**	—	—	—	—	—	—	—	Yes
Phosphines								
TOP**	—	—	—	—	—	—	—	No
Nitriles								
Acetonitrile ($n=0$)	35.94	3.95	45.6	0.75	0.91	14.60	60.39	Yes
Propionitrile ($n=1$)	28.86	4.04	43.6	0.71	0.93	16.10	60.96	Yes
Butyronitrile ($n=2$)	24.56	4.07	42.5	0.71	0.93	16.60	61.18	Yes
Valeronitrile ($n=3$)	20.03	4.12	42.4	—	—	—	60.75[21]	Yes
Hexanenitrile ($n=4$)	17.26	3.48	—	0.90	0.89	—	—	Yes
Benzonitrile	25.20	4.28	46.7	—	0.80	13.00	55.44	Yes
Ethers								
Diethyl ether	4.42	1.11	34.5	0.27	1.01	19.20	78.77	No
Tetrahydrofuran	7.47	1.69	37.4	0.58	1.28	20.50	90.40	No
Other oxygen donors								
1-Methyl-2-pyrrolidone	32.58	3.75	42.2	0.92	2.19	27.30	112.56	No
Dimethylformamide	37.06	3.79	43.2	0.88	2.10	26.60	110.49	No
Dimethylsulfoxide	46.71	3.96	45.1	1.00	2.54	29.80	105.34	No
Other nitrogen donors								
Pyridine	13.22	2.21	40.5	0.87	1.86	34.00	128.08	No
Triethylamine	2.45	0.72	32.1	0.14	2.13	31.70	135.87	No
Hydrocarbons								
Hexane	1.89	0.00	31.0	−0.08	—	0.00	—	No
Benzene	2.27	0.00	34.3	0.59	−0.49	0.10	—	No
Chloronated hydrocarbons								
1-Chloropropane	8.53	2.06	37.4	—	−0.30	—	—	No
1,2-Dichlorobenzene	10.36	2.53	38.0	0.80	—	3.00	—	No††

Values are compiled from Abboud and Notari[23] unless otherwise noted. The n value listed for ketones and nitriles corresponds to the molecular length in Fig. 3a.
*ε_r is relative permittivity (formerly dielectric constant).
†μ is the modulus of the molecular dipole moment (D).
‡E_T (30) is a common polarity scale (kcal mol^{-1}).
§π* is a common polarizibility scale (kcal mol^{-1}).
‖pK_{BH} is a basicity scale based on hydrogen bond formation of a donor molecule with an OH group (kJ mol^{-1}). Compiled from ref. Laurence and Gal[21].
¶DN is the Gutmann donor number, a basicity scale defined as the negative enthalpy change upon interaction of donor molecule with $SbCl_5$ (kcal mol^{-1}).
$-\Delta H_{BF3}$ is a basicity scale based on the negative enthalpy change upon interaction of a donor molecule with BF_3 (kJ mol^{-1}).
**1 ml of 1.9 μM trioctylphosphine oxide (TOPO) in trioctylphosphine (TOP) was added per milligram of Si NCs.
††Si NCs appear to stabilize but can be centrifuged or filtered out.

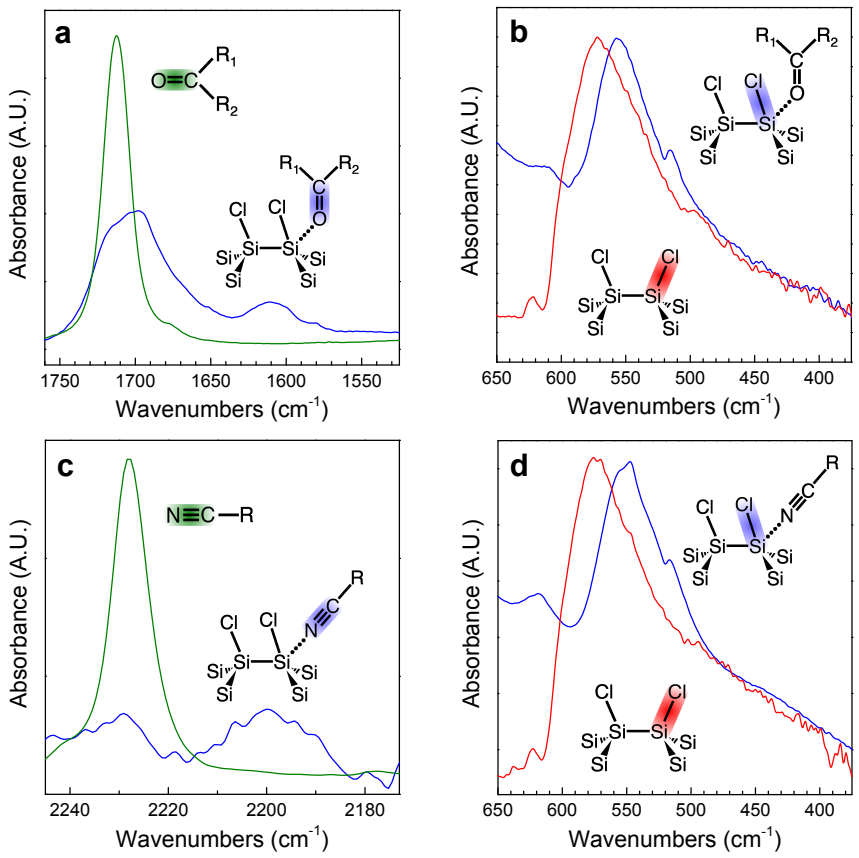

Figure 4.2: **ATR-FTIR characterization of hypervalent interactions.** Electron density redistribution due to hypervalent interaction leads to lengthening of the donor group bond as well as the peripheral bonds of the accepting acidic site. This is clearly observed in ATR-FTIR spectra of the Si NC-donor molecule system by red-shifting of the stretching modes of these bonds. **a**, The carbonyl stretching region of neat 2-butanone (green) and 2-butanone in the presence of Si NCs (blue). **b**, The Si-Cl_x stretching region of as-synthesized Si NCs (red), and the red-shifted stretch in the presence of 2-butanone (blue). The same trend is observed in the nitrile region of the spectrum (**c**) for nitrile solvents interacting with the Si-Cl_x groups of the Si NC surface (**d**). Bond color of inset diagrams indicate vibrations observed in the corresponding spectra.

4.3 Infrared spectroscopy of nanocrystal surface interactions

It is clear from observational studies that a Cl-terminated surface is needed to achieve colloidal stability as well as free carrier absorption. Hypervalent interaction between Si-Cl groups with donor molecules is well-estabilished in synthetic organosilicon work[81]. Here, we employ ATR-FTIR to demonstrate this interaction at the Si NC surface. A cartoon depiction of the interaction between a Si-Cl surface group of a Si NC with the donor carbonyl group of 2-butanone is provided in figure 1e.

IR vibrational modes are well known to be sensitive to changes in electron density and bond length. The carbonyl[114] and nitrile[115] stretching modes have been extensively studied in this regard due to their spectral isolation and sensitivity. Figure 4.2a shows the IR spectrum of the carbonyl stretching region of 2-butanone. The carbonyl stretch of neat 2-butanone is plotted in green with a characteristic frequency of 1712 cm^{-1}. The blue spectrum is taken after a solution of Si NCs is allowed to evaporate onto the ATR crystal. In the presence of Si NCs, the carbonyl peak has broadened and red-shifted by 25 cm^{-1}. Additionally, a lower-energy satellite peak emerges at 1610 cm^{-1}. Gutmann's empirical analysis of acid-base interactions[108] serves as an intuitive guide to understanding the spectral shifting by redistribution of electron density and subsequent change in bond lengths upon Lewis acid-base interaction. Upon interactions, the bond length of the Lewis base (carbonyl) is increased, which polarizes the electron density toward the Lewis acidic site (Si surface atom). The lengthened bond is clearly seen in figure 1a as a shift to a lower energy vibration in the ATR-FTIR spectrum. The satellite peak is likely due to more strongly bound 2-butanone molecules.

The response of the Lewis acidic site (Si surface atom) to this interaction is an increase in the coordination number and a lengthening of the peripheral Si-Cl_x bonds, which is observed in the IR spectrum as a red-shift from 575 cm^{-1} to 550

cm^{-1} in the Si-Cl_x stretching modes (Fig. 4.2b). No other spectral shifting is observed. Secondary bonds also predicted by Gutmann to be affected, such as the Si-Si or C-C vibrational modes, are difficult to resolve or show no shifting. This is not surprising, as effects due to hypervalency are less significant farther away from the acid-base interaction site.

The ATR-FTIR spectra in Figure 4.2c and d show a similar effect of the nitrile group of benzonitrile interacting with Si-Cl_x groups of the Si NC surface. The nitrile stretch in Figure 4.2c is red-shifted from 2225 cm^{-1} to 2200 cm^{-1}. The red-shift is of similar magnitude to that observed in the carbonyl group of 2-butanone. The Si-Cl_x stretch also shifts from 575 cm^{-1} to 550 cm^{-1} (Fig. 4.2d).

One must be careful in the application of Gutmann's rules to the surface of a NC, as structural reorganization of the molecules is typically needed to lower the energy of the newly-formed hybrid orbitals. The surface Si atoms of the NC are relatively fixed in comparison, but shifts in electron density are certainly possible. The more rigorous molecular orbital picture is consistent with Gutmann's empirical rules. Si is able to engage in electron-rich three-center four electron bonding, which results in a pair of hybrid orbitals that localizes the electron density at the peripheral atoms[79]. Constituent bonds are thus lengthened, which is observed as a red-shift in the ATR-FTIR spectrum. Taken together with Lewis acid-base theory, we conclude the ATR-FTIR data confirms hypervalent interactions at the Si NC surface. Most importantly, the observations shown for Si NCs in 2-butanone and benzonitrile are generalizable; similar spectral shifting is observed for the many ketones/aldehydes and nitriles investigated.

4.4 Mechanism of colloidal stability

Colloidal stability is an attractive feature of NC systems, as it enables cost-effective deposition of thin films for optoelectronics. Currently, success in device integration of NCs lies in the ability to chemically exchange insulating

ligands for shorter species during film deposition[35,37] or in solution for charged ionic species[6,39,40]. The key to both of these strategies is ligands that are relatively labile and thus freely exchanged. This is an important distinction to group IV NCs. While long-chain ligands also provide colloidal stability in group IV NCs[14,65], the surface species are covalently bound, and ligands are kinetically inert to exchange reactions. This feature has precluded significant progress on group IV NC device development when compared with metal chalcogenide NCs. Thus, understanding the mechanism of stability observed in this work will be important for development of colloidal NCs for optoelectronics.

In a series of experiments, we illustrate hypervalent interactions at the Si NC surface are responsible for colloidal stability rather than the two common mechanisms typically associated with this effect (steric and electrostatic interactions)[116]. We begin by investigating the effects of varying the molecular length of n-alkanones and n-alkanenitriles. Figures 4.3a and b show Si NC concentration as a function of molecular length for ketones and nitriles, respectively.

If the Si NC colloids are stabilized by steric interactions between the long-chain tails of strongly-bound ligands, then longer chain molecules are expected to have a larger steric barrier and provide better stability. However, the data show that Si NC concentration decreases with increasing ketone length (Fig. 4.3a). Nitriles exhibit a slightly different trend, with Si NC concentration increasing with chain length until heptane- and octanenitrile (n = 5 and 6, respectively), then decreasing again as chain length is increased further (Fig. 4.3b). If Si NC colloids are formed from steric interactions between the non-covalently bound solvent molecule, no decrease in stability should be observed upon increasing chain length. Furthermore, adding a typical non-polar solvent used in sterically-stabilized solutions, such as hexane, causes Si NCs to quickly flocculate and phase-separate from the stable solution, which suggest that non-polar solvents disrupt the stabilizing forces provided by the weakly-bound ketone or nitrile molecules.

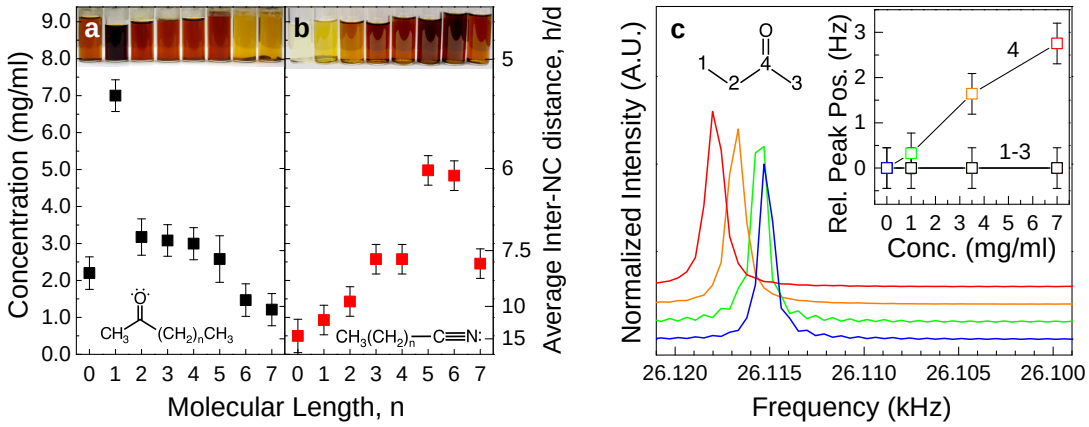

Figure 4.3: **Mechanism of colloidal stability determination.** Si NC concentration as a function of molecular length, n, for n-alkanones (**a**) and n-alkanenitriles (**b**) as determined by UV-Vis absorption. The right axis is the average inter-NC separation distance. If electrostatics are the dominant mechanism of colloidal stability, then shorter molecules should achieve higher concentrations. If steric effects were dominant, longer molecules are expected to provide more highly-concentrated Si NC solutions. Photographs of the solutions are included at the top of the graph. Error bars reflect uncertainty in mass measurements. **c**, The carbonyl region of the ^{13}C NMR spectra of Si NCs stabilized in 2-butanone at concentration of 0, 1, 3.5, and 7 mg/ml. The spectra are normalized and vertically offset for clarity. The downfield shift of the carbonyl peak is due to Si NC surface interactions and resulting interactions in the solvent shells surrounding the NC. Aliphatic carbon peaks (1-3) do shift relative to neat 2-butanone with increasing Si NC concentration (inset). Error bars correspond to the digital resolution of the spectrometer.

We explore the interaction of solvent molecules with the Si NCs using ^{13}C nuclear magnetic resonance (NMR). Since NMR is a time-averaged technique, solvent dynamics can be probed. Shifts are expected for short-lived interactions (shorter than the NMR signal decay time), whereas a strongly-bound molecule would give rise to a second peak. Figure 4.3c shows the carbonyl region of the ^{13}C NMR spectrum at increasing concentrations of Si NCs in 2-butanone. The data show a clear downfield shift of the carbonyl peak with increasing concentration from 0 to 7 mg/ml (Fig. 4.3c), which illustrates the fluxional nature of the solvent molecules with the Si NC surface. Peaks corresponding to the aliphatic carbons do not shift (Fig. 2c, inset). This effect is frequently observed in the solvation of ions as well as molecules when dissolved in carbonyl-containing solvents[117]. A downfield shift of the carbonyl carbon establishes direct interaction between the solute and the carbonyl oxygen as well as intermolecular ordering of dipole moments in the solvation shells surrounding the solute. Though the 2-butanone molecules interact with the Si NC surface, they are not strongly bound.

For electrostatic stabilization, which is typically described by Derjaguin, Landau, Verwey and Overbeek (DLVO) theory, a shorter ketone or nitrile, which have the highest relative permittivity (formerly dielectric constant), will more effectively screen charge. Indeed, high relative permittivity solvents such as water (ϵ=80.1) and formamide (ϵ=111.0) were needed to stabilize NCs after terminating the surface with negatively-charged inorganic ligands[40]. If Si NC solubility were dominated by electrostatics, then shorter molecules with a higher relative permittivity should yield more highly concentrated solutions. However, Si NC concentration is highest for ketones (2-butanone, n=1) and nitriles (heptanenitrile, n=5) with only modest relative permittivities (18.85 and 15.6, respectively[118]).

Additional evidence also supports electrostatics as insignificant. Firstly, the addition of electrolytes to stable solutions should contract any electrical double layer predicted by DLVO theory, which would allow the NCs to agglomerate and fall out of solution. No such effect is observed upon adding 1.0 mg of NaCl to a

1.0 mL solution of 0.5 mg/mL Si NCs in 2-butanone. Secondly, Si NCs solvated in ketones show no measurable ζ-potential, which is the standard technique to evaluate colloidal charging[119]. Whereas some nitriles had ζ-potentials as high as -25 mV (benzonitrile), this is still below the widely-regarded $\pm$30 mV needed for colloidal stability based on electrostatic interactions as well as the -60 mV observed in the negatively-charged MMC-terminated NCs[6]. Moreover, a Coulombic model that adapts DLVO to organic solvents would predict a surface potential of $\pm$81.4 mV for 8 nm particles in 2-butanone and $\pm$89.5 mV in pentanenitirile[120].

It appears macroscopic models do a poor job of explaining the observed colloidal stability. The average inter-NC separations (h/d) in our solutions (Figs. 4.3a and b) are beyond the regime of continuum theory, and non-DLVO forces, such as solvation, will dominate[121,122]. The Si NC dispersions have remained stable for over one year when kept air free. Solutions in 2-butanone reach an h/d value of nearly 5 NC diameters, and Brownian motion alone would lead to flocculation on the time scale of a few microseconds without a significant barrier to agglomeration. These data suggest the fluxional hypervalent interactions within these Si NC solutions are indeed the dominant mechanism of stability. Secondary molecule-molecule interactions also likely play a role, as a modest dipole moment (μ) is needed in addition to donor strength (Table 4.1). This explains why 2,3-butanedione does not provide stability, which has similar donor strength to 2-butanone but no dipole moment.

4.5 Surface doping of silicon nanocrystals

It is perhaps not surprising that hypervalent NC surface interactions could provide doping effects. From the ATR-FTIR studies, it is clear additional electron density is being donated from the Lewis base molecule to the Si surface atoms. Similar phenomena have been investigated, and it is often referred to as "surface-transfer"[123] or "molecular"[124] doping. Experimental studies on porous Si has demonstrated n- and p-type doping with donor (NH_3) and acceptor

(NO_2) molecules, respectively[125]. A similar effect was demonstrated with Si nanowires in which dopant concentration could be controlled by the partial pressure of the molecular dopant[126] at the Si surface. Computational studies also validate these experiments[124,127]. In each case, Si is reversibly doped by the adsorption of donor or acceptor molecules.

In this work, we demonstrate the doping effect by employing ATR-FTIR. Si NCs are first deposited onto an ATR crystal. The spectrum of the as-synthesized Si NCs can be seen in Figure 4.4a with the characteristic Si-Cl_x stretching vibration at 575 cm^{-1}. A dense colloid is formed upon addition of pentanenitrile (Fig. 4.4b) onto the Si NCs. A spectrum is taken every 20 seconds as the Si NC solution evaporates. The initial spectrum (Fig. 4.4c, 1) is nearly identical to neat pentanenitrile. The broad absorption then emerges with the Si-Cl_x stretching vibration of the Si NCs. The IR absorption intensity increases from (1) to (4) where it reaches a maximum after 640 seconds of evaporation time. The broad absorption then slowly decreases and red-shifts as solvent molecules evaporate from the Si NC surface, and a film is assembled at (5).

The broad absorption in Figure 4.4c is attributed to free carrier absorption, or, in the case of non-interacting NCs, localized surface plasmon resonance. Heavily phosphorus-doped Si NCs were recently shown to exhibit localized surface plasmon resonance in this mid-infrared region[128]. Applying similar analysis, the absorption feature centered at 1000 cm^{-1} corresponds to an approximate doping concentration of 10^{19} cm^{-3}. This high doping level is consistent with the high surface-area-to-volume ratio of the 8 nm NCs.

The surface doping effect appears reversible. The broad absorption peak red-shifts as surface molecules evaporate from spectrum 4 to 5 in Figure 4.4c. The Si NC solution was allowed to evaporate for roughly twelve hours. This spectrum is shown in Figure 4.4d (blue). Applying dynamic vacuum (roughly 10^{-2} torr) to the sample for 800 s decreases the intensity and red-shifts the free carrier absorption. At the same time, the absorption intensity of the C-H_x and C≡N vibrations associated with surface molecules decrease by a factor of three

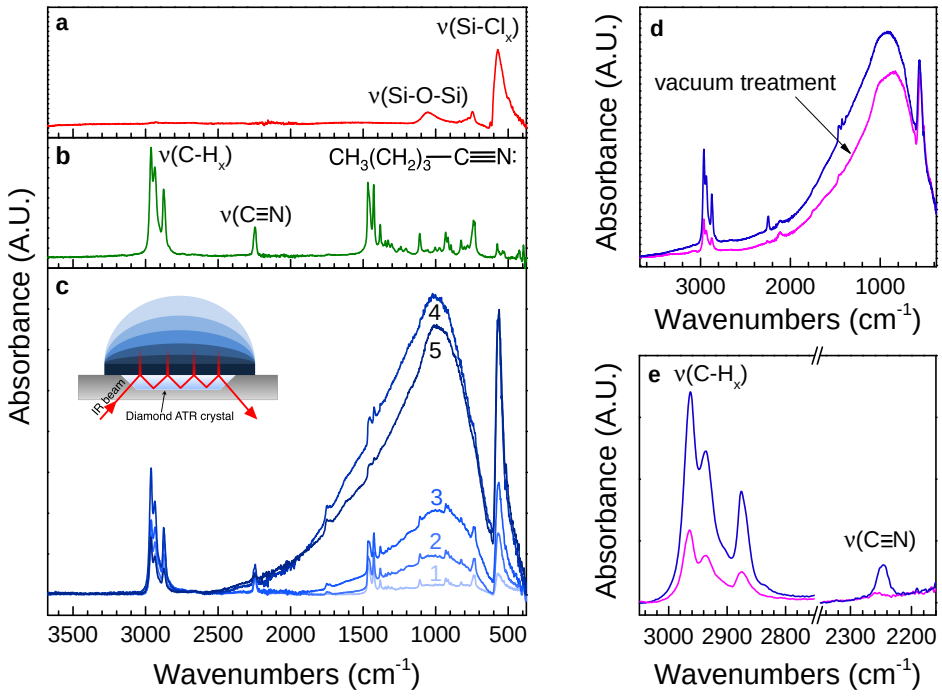

Figure 4.4: **Surface doping of Si NCs. a**, ATR-FTIR spectra of as-synthesized Si NCs and neat pentanenitrile (**b**) are provided as reference for **c** where pentanenitrile is added to Si NCs on an ATR crystal, and spectra are recorded every 20 seconds. Spectra are not normailized. The spectra are identical to neat pentanenitrile until a broad absorption due to free carriers is observed. The absorption arises from solvent molecules non-covalently bound to the NC surface that effectively dope the NC. As solvent evaporates, the broad IR absorption band increases in intensity from (1) to (4) then decreases and red-shifts as solvent evaporates from the Si NC surface, and a film is assembled at (5). Much of the remaining solvent can be removed by applying dynamic vacuum to the film (**d**). After 800 seconds, the absorption intensity of characteristic pentanenitrile vibrational modes, ν(C-H$_x$) and ν(C≡N), is decreased by a factor of ∼3 (**e**).

(Fig. 4.4e), which indicates the dopant effect is indeed due to hypervalent interactions at the Si NC surface.

The ability to remove surface molecules is also clear from thermogravimetric analysis shown in figure 4.5. In fact, attempts to corroborate the observed ATR-FTIR shifts with x-ray photoelectron spectroscopy was not possible because signal from the solvent was not present. This is presumably due to solvent evaporation in ultra-high vacuum (10^{-9} Torr), which apparently removes surface-bound molecules. These observations are consistent with the fluxionality of 2-butanone molecules observed by ^{13}C NMR.

4.6 Electrical characterization of thin films

Initial efforts were made to demonstrate the viability of Si NC films for electronic devices by fabricating a simple Al/Si NC/Al vertical structure. Device areas of 1 mm^2 and 4 mm^2 show consistent behavior. Figure 4.6 shows examples of the typical behavior observed. Without heat or vacuum treatment, the Si NC films were highly conductive at voltages below 1 V and exhibit dark conductivities as high as 10^{-5} S/cm (Fig. 4.6a, inset). We believe this is due to surface doping effects, which indicates incomplete removal of bound solvent molecules. Films also showed little response to temperature when varied from 298 K to 80 K, which also indicates extrinsic conduction.

After applying voltages up to 5 V (Fig. 4.6a) the films show non-ohmic behavior. The same behavior is observed for films that are annealed or treated with vacuum, which suggests these treatments disrupt molecular doping effects. Figure 4.6c shows a log-log plot of a film cast from benzonitrile and vacuum annealed at 200 °C for 12 hours at 10^{-2} Torr. The slope (m) of the log-log curve is 3.24 at voltages >0.2 V, which indicates space-charge-limited current. The films still exhibit ohmic ($m = 1$) transport at voltages <0.2 V corresponding to a dark conductivity of 10^{-8} S/cm. This is consistent with the intrinsic conduction observed in a recent report of undoped Si NC films deposited by aerosol

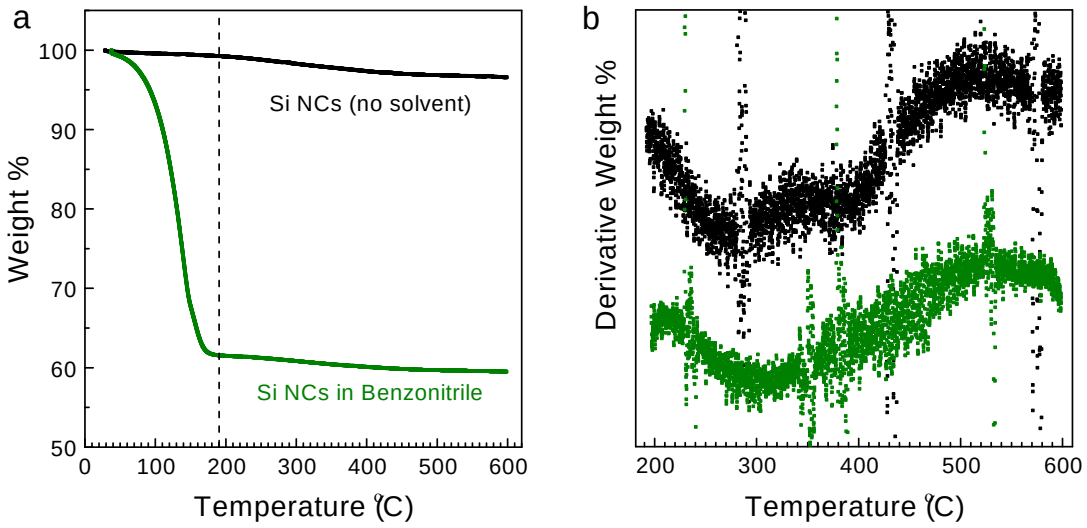

Figure 4.5: **Solvent removal.** To demonstrate removal of dispersing solvent after film formation, we employed thermogravimetric analysis (TGA). **a**, Normalized weight as a function of temperature for 12.98 mg Si NCs transferred directly to a TGA pan (black). Benzontrile was added to a second TGA pan, and Si NCs were added to form a dense colloid. The solvent was allowed to naturally evaporate under N_2 purge. After 12 hours the sample weight remained constant 36.81 mg to indicate the free dispersing solvent molecules had evaporated. This sample is the green spectrum in (**a**). The experiments were performed in a N_2 atmosphere. A ramp rate of 10 °C/min was used. The sample of Si NCs solvated in benzontrile lost roughly 40% of its weight as it approached the boiling point of benzonitrile at 190°C (dashed vertical line). **b**, The derivative spectrum shows the weight loss behavior of the Si NCs solvated in benzonitrile (green) after the solvent has evaporated (200°C) is nearly identical to the as-synthesized Si NCs (black).

impaction[63]. We are currently working to manipulate film casting conditions to improve consistency of these initial investigations.

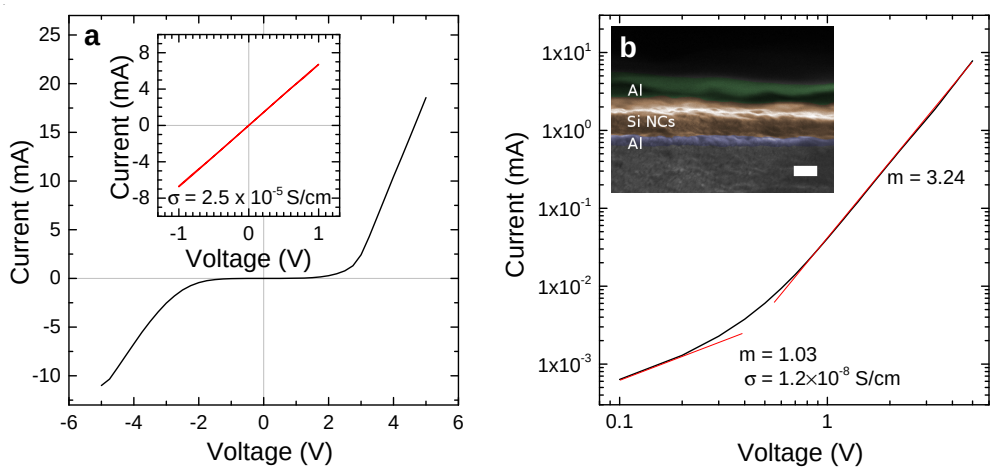

Figure 4.6: **Si NC thin film device characterization.** Films cast from benzonitirle and allowed to naturally evaporate show non-ohmic behavior at voltages >1 V. A typical curve is shown in **a**. **b**, Before applying higher voltage, Al/Si NC/Al devices show highly conductive ohmic transport exhibiting dark conductivities on the order of 10^{-5} S/cm. We believe this is due to surface doping effects. Films also showed little response to temperatures varied from 298 K to 80 K, which indicates extrinsic conduction. After applying voltages >1 V or annealing the film , the films are no longer ohmic. **c**, A log-log plot of the device characteristics of a film cast from benzonitrile and vacuum annealed at 200 °C for 12 hours at 10^{-2} torr. Fitting the log-log current-voltage curves shows films exhibit ohmic transport at <0.2 V corresponding to a dark conductivity of 10^{-8} S/cm. Space-charge-limited current (m=3.24) is observed at higher voltages. The inset is a colorized SEM images showing the device cross-section.

4.7 Discussion

To elucidate the observed interactions of donor molecules with the Si NC surface, we invoke a simple molecular orbital theory model (Fig. 4.7). The lowest unoccupied molecular orbital (LUMO) of the Si-H groups is too high afford a favorable interaction with donor molecules. Electron density is polarized

away from the Si surface atoms with Cl termination, which effectively lowers the LUMO of the Si NC surface[129]. The LUMO of Cl-terminated Si NCs is now at an accessible level to interact with the highest occupied molecular orbital (HOMO) of donor molecules, whereas the LUMO of H-terminated Si NCs remains inaccessible. This is consistent with our observations that hypervalent interactions, and subsequent colloidal stability and free carrier absorption, are only realized in Cl-terminated Si NCs.

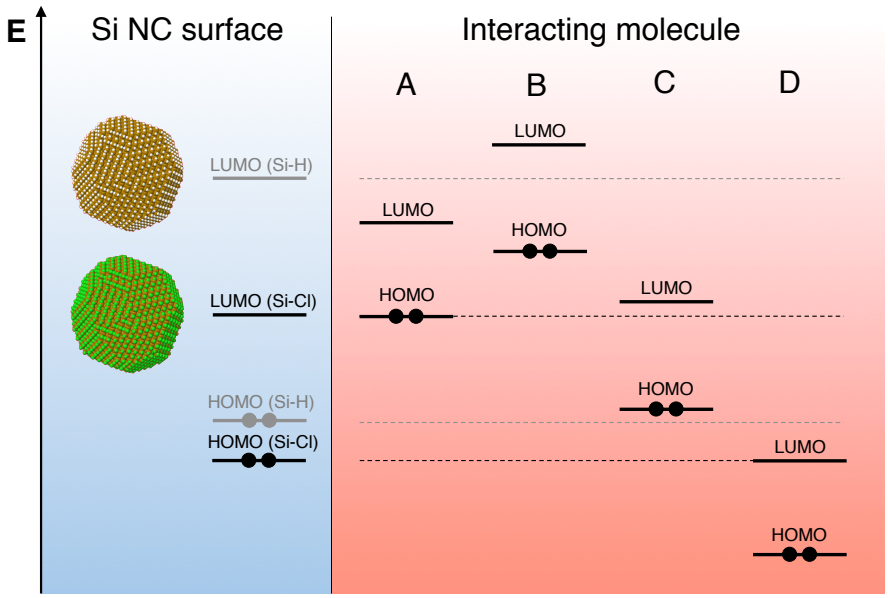

Figure 4.7: **Molecular orbital picture.** The Cl-termination of the Si NC surface effectively lowers the LUMO energy in comparison to the H-terminated Si NC surface (i.e. the Si-Cl group is more Lewis acidic). Molecule "A" represents a molecule with favorable energetic alignment for hypervalent interactions. In this study, we find ketones, aldehydes, and nitriles to fit this criteria. "B" molecules are strong Lewis base donors such as DMF and pyridine. These molecules also donate electron density but to an extent where the Si-Cl surface is not preserved. "C" molecules are chemically inert molecules such as hydrocarbon and chlorinated hydrocarbon solvents, and "D" molecules represent protic solvents, such as alcohols, that contain acidic hydrogens, which hydrolyze the Si-Cl group.

Interacting molecule "A" in Figure 4.7 represents molecules such as ketones, aldehydes, and nitriles that have a HOMO near the same energy as the Si-Cl

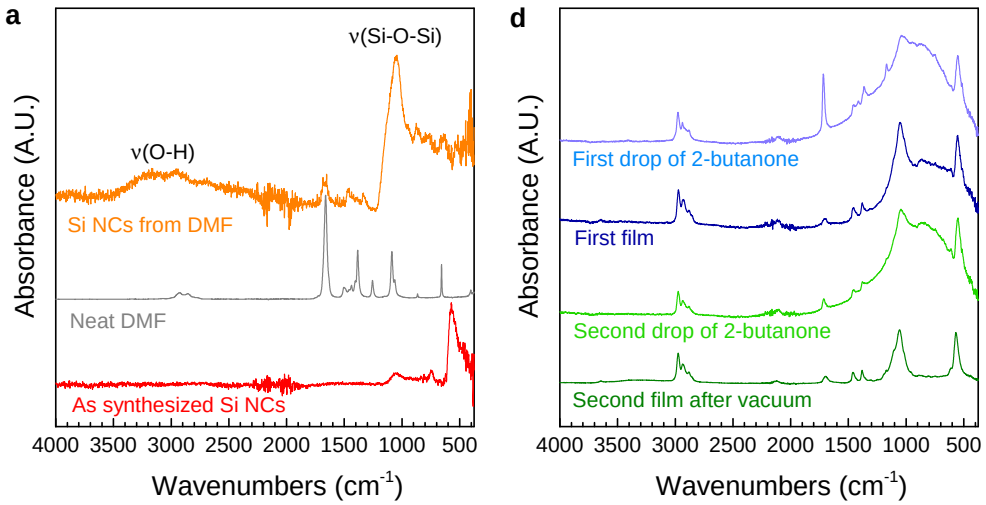

Figure 4.8: **Instability of the surface Si-Cl bond.** **a**, ATR-FTIR spectra of as-synthesized Si NCs (red) and neat dimethylformamide (gray). After the addition of dimethylformamide to the Si NC sample, the resulting film (orange) is oxidized by trace amounts of water in the N_2-purged glovebox. This is apparent from the Si-O-Si vibrational mode that appears at 1090 cm^{-1} and the broad O-H absorption centered at 3200 cm^{-1}. **b**, Si NCs are dispersed in 2-butanone (light blue) and the solvent is allowed to evaporate to form a Si NC film on the ATR crystal (dark blue). There is a broad absorption due to free carriers. The Si-O-Si peak is indicative of hydrolysis from trace water in the N_2 glovebox. A second drop is added to the same film (light green) and allowed to evaporate. The free carrier absorption peak returns. The film is then put under dynamic vacuum (10^{-2} Torr) to remove solvent and demonstrate reversibility of doping effect. The free carrier absorption peak is no longer visible (dark green). Spectra are offset for clarity.

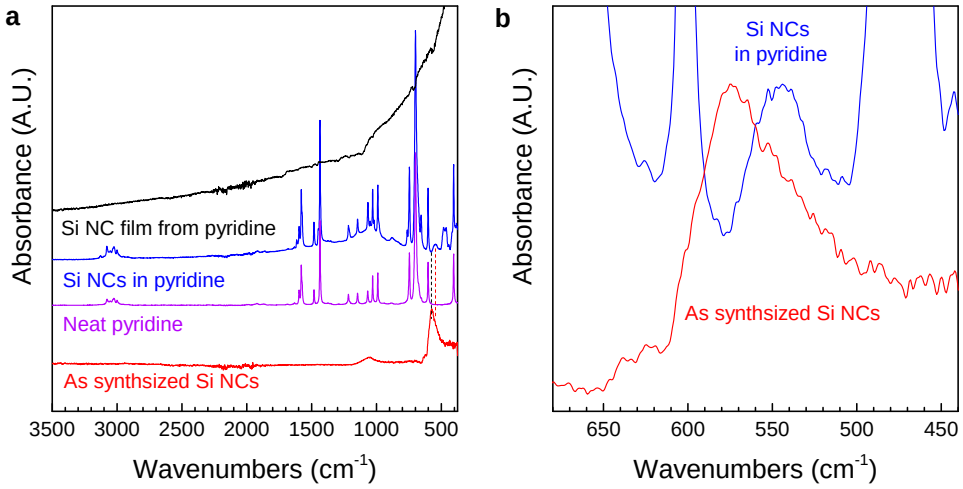

Figure 4.9: **Si NC interaction with pyridine.** **a**, Attenuatated total reflection-Fourier transform infrared (ATR-FTIR) spectra of as-synthesized Si NCs (red). Neat pyridine (magenta) is added to the Si NCs on the ATR crystal (blue). The resulting film (black) shows few molecular vibration peaks but has characteristic ν^3 (ν=frequency) dependence of free carrier absorption. **b**, Si-Cl_x region of the spectrum where a 25 cm^{-1} red-shift in the solvated NCs (red) can be observed in comparison to the as-synthesized Si NCs (blue). Spectra are offset for clarity.

LUMO and are thus able to favorably interact with the Si-Cl surface groups. Electron density is donated from the donor group of the molecule to the Si surface in the form of a hypervalent interaction. This leads to the characteristic shifting in the ATR-FTIR peaks previously discussed.

Interacting molecule "B" of Figure 4.7 is a strong Lewis base. This includes common oxygen donors such as dimethylformamide and DMSO as well as nitrogen donors such as pyridine and triethylamine. Charge transfer should occur with these molecules as well, but, in general, acid-base interactions exist on a continuum between hypervalent states and ionized states[79]. As the strength of the donor increases and the number of hypervalent bonds increases, peripheral bonds (Si-Cl) become more polarized and unstable, which leads to the formation of an inner sphere ionic complex. This leads to enhanced susceptibility to hydrolysis[130]. Whereas figure 4.9a and b demonstrates the more sterically-hindered donor nitrogen of pyridine shows evidence of hypervalent interaction, hydrolysis with trace amounts of water in a N_2-purged glovebox is observed in the ATR-FTIR spectrum upon interaction with strong donors such as dimethylformamide. This can be observed in figure 4.8a.

Finally, molecule "C" of Figure 4.7 represents non-polar, chemically-inert solvents such as hexane and benzene, and molecule "D" represents solvents that have yet to be discussed, which are protic solvents that possess an acidic hydrogen. These molecules hydrolyze the Si-Cl group.

It is clear that donor strength is an important parameter for hypervalent interaction with the Si NC surface from this analysis. Table 1 provides a variety of solvent scales that reflect physical properties (relative permitivity, dipole moment, polarizability, etc.) as well as basicity (donor strength), of investigated solvents. pK_{BH}, Gutmann donor number (DN), and -ΔH_{BF_3} are common basicity scales that reflect the relative strength of interaction between a Lewis base and a standard Lewis acid. Though the scale has seen criticism[113], antimony pentachloride is a sterically-hindered molecule that is a reasonable analog to the Si-Cl surface. It appears donor numbers between 13 kcal/mol and

17 kcal/mol, which corresponds to ketones/aldehydes and nitriles, yield favorable interaction with the Si NC surface. Higher donor numbers result in removal of Cl^- from the Si surface, and lower donor numbers do not noticeably interact. These trends are comparable for the remaining basicity scales. In fact, even small differences in *DN* between typical ketones and nitriles is noticeable as seen for reversible doping with 2-butanone in figure 4.8b.

In conjunction with experimental evidence, this model has important implications for many NC systems. By modulating the Lewis acidity of the NC surface, we have demonstrated hypervalent interactions as an avenue for colloidal stability and charge transfer doping. Hypervalency is not limited to Si. In fact, heavier group 14 elements (Ge, Sn, and Pb) should accommodate hypervalent interactions better than Si. We believe this is the mechanism previously observed in the colloidal stability[83] of Cl-terminated Ge NCs. Boron and all main group elements below the third period of the periodic table are well known to engage in hypervalent interactions as well. This includes widely-studied IV-VI compounds (PbS, PbSe) as well as emerging III-V NC materials.

4.8 Conclusion

The results presented here have the potential to impact two fundamental challenges in achieving practical application of colloidal NCs for optoelectronic devices. Hypervalent surface interactions observed at the Si NC surface has led to a novel mechanism of colloidal stability as well as a surface doping effect. This is achieved by terminating the Si NC surface with Cl, which leads to an acidic Si surface atom that can favorably interact with a particular class of donor solvents. We are able to understand and validate these findings with the application of a simple molecular orbital model, which we believe can be extended to encompass a variety of NC material systems.

4.9 Experimental Methods

Si NC synthesis. Cl-terminated Si NCs were synthesized by flowing 30 sccm of argon, 20 sccm of H_2, and 4 sccm $SiCl_4$ into an evacuated plasma reactor[54] and applying a nominal RF power of 200 W at 13.56 Hz to a pair of ring electrodes mounted on an alumina tube (1.90 cm OD, 1.27 ID). The pressure in the reactor was 733 Pa. See supplementary information for a more detailed description.

Colloid formation: The chlorinated surface is quite reactive to ambient conditions, and all processing is done air-free. Si NCs are collected by impacting them onto a substrate downstream of the plasma. The Si NCs are transferred from the reactor in a vacuum-component assembly pressurized with argon and further processed on a Schlenk line or in an inert-atmosphere glovebox. For UV-Vis absorption, Si NCs were transferred into a an ampule and capped with a septum in the glovebox. The capped ampule is removed from the glovebox and a solution is formed by transferring solvent to the ampule via cannula. The nitrogen atmosphere is removed, and the ampule is flame-sealed.

Solvents. The following solvents were purchased from Sigma Aldrich (purity and grade are included if available): acetone (≥99.9%, HPLC), 2-butanone (≥99.7%, HPLC), 2-pentanone (99.5%, HPLC), acetonitrile (≥99.9%, HPLC), propionitrile (99%), butyronitrile (≥99%), valeronitrile (99.5%), hexanenitrile (98%), heptyl cyanide (97%), nonanenitrile (98%), benzonitrile (99.9%, HPLC), 1-methyl-2-pyrrolidone (≥99%, HPLC), 2,3 butanedione (97%), methanol (HPLC), 1-butanol (≥99.7%, HPLC), 1-chloropropane (98%), 1-chlorobutane (≥99.8%, HPLC), 2-chlorobutane (≥99%), 1-chloropentane (99%), 2-chloropentane (95%), 1-chlorohexane (99%), 1-chloroheptane (99%), 2-chloroheptane, acetophenone (≥99.0%, GC), trioctylphosphine (97%), tributylphosphine (97%), N,N-dimethylethylamine (99%), N,N-dimethylbutylamine (97%), hexane (≥97.0%, HPLC). The following

solvents were purchased from Alfa Aesar: 2-hexanone (98%), 2-heptanone (99%), 2-octanone (98%), 2-Nonanone (98+%), 2-decanone (97%), octanenitrile (97%). Solvents were stored on a Shlenk line over 3Å molecular sieves for at least 24 hours after three freeze-pump-thaw cycles were performed to remove residual water and oxygen.

Film formation. Thin films of Si NCs were assembled by drop-casting onto a Au-coated Si wafer, placing a small funnel over the film to slow evaporation. The SPM topology image was obtained on a Digital Instruments Nanoscope operating in tapping mode with a scan rate of 0.4994 Hz and 512 lines per image.

DLS and ζ-potential. DLS spectra and electrophoretic mobility was evaluated on a Brookhaven ZetaPALS instrument using phase-angle light scattering with varied conditions between 50 V and 200 V at 2 Hz. ζ-potential values were evaluated from the electrophoretic mobility by applying Henrys equation at the Smoluchowski limit[119]. Relative permittivities were obtained from the Landolt-Börnstein Database[112].

Calculations. The average inter-NC distance, h, is derived within the close-packing model of uniform spheres: $h/d = (\pi/(3\sqrt{2}\phi))^{1/3} - 1$ where we normalize by the NC diameter, d, and ϕ is the volume fraction of Si NCs to solvent. We assume bulk density of Si. Calculation of the half-life of the NC solution follows from the Smoluchowski theory of diffusion-limited (perikinetic) aggregation. The derivation can be found in many textbooks[116] and assumes uniform Brownian spheres under no external fields. We have: $t_{1/2} = \pi\mu d^3/(8k_BT\phi)$ where μ is the viscosity of the medium, k_B is the Boltzmann constant, and T is temperature. The half-life of the solution drops steeply with particle size, which illustrates the difficulty of stabilizing particles with diameters as small as the nanocrystals investigated in the main text.

Colloid Concentration. UV-Vis absorption of centrifuged Si NC solutions was performed on a Cary 5E UV-Vis spectrophotometer. Centrifugation was done at 4000 rpm for up to 30 minutes. After centrifugation, optically transparent solutions indicate insignificant scattering, and the Beer-Lambert law ($A = \epsilon lc$) is employed to determine mass concentration from absorption by integrating the absorption spectra (Supplementary Figure S7) between 550nm to 800nm. The absorbance, A, is linearly dependent on concentration, c. The path length through the solution, l, and the extinction coefficient, ϵ, are constants. A was determined by integrating under the absorbance curve. The absorbance of 5.6 mg of Si NCs in 1.25 ml of 2-butanone, A_b, did not change after centrifugation, so the concentration, c_b, was known. It was used to determine the unknown concentration, c_o, of other solutions relative to 2-butanone. After subtracting the background solvent, the concentration of other solutions is obtained from: $A_o/A_b = c_o/c_b$.

^{13}C NMR. Samples were prepared by transferring Si NC solution to an evacuated quartz NMR tube and flame-sealing the tube. ^{13}C NMR spectra were obtained on a Bruker Avance III 500 MHz spectrometer equipped with a BBFO Smart Probe by locking onto a D_2O capillary at ambient temperature. 1024 scans were obtained at 125 MHz with a 29761.9 Hz sweep width, 30 degree pulsewidth, 1.1 second acquisition time, and 2.0 second relaxation delay.

ATR-FTIR. ATR-FTIR experiments were done on a diamond ATR crystal using a Bruker Alpha FTIR spectrometer inside a N_2-atmosphere glovebox. Spectra were typically collected by averaging 24 scans at 2 cm^{-1} resolution.

Si NC thin film device fabrication. Films of Si NCs were spin-cast at 1500 rpm for 1 minute on a glass substrate with 40 nm pre-deposited aluminum electrode. Si NCs were cast from either 2-butanone or benzonitrile and allowed

to dry at atmospheric pressure and under 10^{-7} Torr vacuum for up to 12 hours. Typical films thickness measured in SEM was between 100 nm and 150 nm from. The 1 mm^2 and 4 mm^2 vertical devices were completed by evaporating a 100 nm top aluminum contact. Films are annealed and vacuum-treated under a halogen lamp using an in-house fabricated annealing chamber with 10^{-2} Torr vacuum.

4.10 Future work

The chlorinated Si NC surface is interesting for many reasons that go beyond colloidal stability and doping. In fact, in the next section I demonstrate an alternative Lewis acidic Si NC surface chemistry that does not rely on "hypervalent" interactions. The colloids are thus much more versatile and chemically robust.

Still, the reactivity of the Si-Cl surface bond can be leveraged. Si-C-R, Si-N-R, and Si-S-R functionalities are all readily attainable using simple solution phase surface chemistry techniques. An illustrative example with a similar Ge-Cl surface is shown in section 6 of this thesis, which yielded the narrowest photoluminescence emission from Ge NCs to date. A similar study on the optical properties of Si or group IV allows NCs as a function of surface functionality is a "shovel-ready" project and should be pursued. These chemistries can also be applied with short functional groups to thin films of NCs pre-deposited in the gas phase in order to passivate trap states that have riddled the electrical properties of similar films.

An interesting endeavor is to move toward more polarized ligand groups at the surface. The best candidate is the Si-N-R linkage. In this case, the polarized Si-N bond may indeed be exchanged for a stronger Lewis base. This has recently been shown for Germanium by exchanging an amine for a thiol group[131], though it would be a more difficult task for Si (See chapter 2). An "exchangeable" ligand is the prerequisite for heterojunction shell growth, which has never been shown for group IV NCs with the exception of a native oxide.

The surface doping effect was an interesting observation in this work, but its stability and control need to be improved for it to be of practical use. An easy first attempt at achieving this is to simply dilute the "dopant molecule" (ketones or nitriles) in a non-interacting but miscible solvent (toluene) to varying degrees to observe a shift in the plasmon resonance. For practical purposes, however, the instability of the surface groups make the Si-Cl surface chemistry better as a starting chemistry on the way to a surface chemistry appropriate for device integration. This could be achieved, perhaps, with a layer-by-layer thin film assembly by exchanging the Si-Cl surface group for a methyl group using the Grignard chemistry described in the following sections.

Chapter 5

The Boronated Silicon Nanocrystal Surface

> "*There must be no barriers to freedom of inquiry ... There is no place for dogma in science. The scientist is free, and must be free to ask any question, to doubt any assertion, to seek for any evidence, to correct any errors.*"
> - J. Robert Oppenheimer

5.1 Introduction

Size-tunable optical properties and the ability to process thin films using scalable, cost-efficient printing techniques have long made colloidal nanocrystals (NCs) an attractive candidate for next-generation optoelectronics. Much of the recent progress in this direction hinges on the ability to manipulate the NC surface. Conventional solution synthesis yields NCs with ligands bound to metal surface atoms through a labile acid-base complex. The electrically-insulating native ligands are thus routinely exchanged to produce conductive NC arrays for devices such as solar cells[132], light-emitting devices[60], transistors[133], and photodetectors[134]. Just as surface manipulation has launched metal-based NCs

to the forefront of optoelectronic technology, it is the inability to do so with the covalent surface of group IV NCs that has greatly hindered progress. In this work, we demonstrate a Lewis acidic boron surface chemistry of gas-phase synthesized Si NCs that provides the same solution-phase versatility as their metal-based counterparts. This represents an immense step toward an abundant, non-toxic alternative to Pb and Cd-based NCs. These Si NCs are also uniquely suited for investigating the mechanism of colloidal stability that has been observed after metal-based NCs are stripped of ligands[135,136] or ligand-exchanged for ionic ligand[6,39–42]. We find the electrostatic mechanism previously invoked to be incomplete. An alternative model is proposed from which we demonstrate stable Si NC colloids in media that runs the gamut from hexane to water.

5.2 The Lewis acidic boron surface

More than three decades of research has launched colloidal NCs from the laboratory to a viable optoelectronic technology platform. As the industry grows, so does the need for non-toxic alternatives to Cd and Pb-based NCs. In opposition to typical solution-based techniques[71], nonthermal plasmas have emerged as the most prolific synthetic method for abundant and non-toxic group IV NCs[53]. However, the resulting nanopowder remains difficult to process without a secondary step to bind an alkane ligand to the surface to render them dispersible in nonpolar solvents[58]. The strength of the Si-C bond makes ligand exchange strategies[6,35] championed by metal-based NCs ineffective. Encouraging results have emerged recently that circumvent the need of a ligand. Plasma-synthesized Si[68] and Ge[83] NCs terminated with chlorine have shown colloidal stability in relatively polar solvents. The electron-withdrawing nature of chlorine renders Si or Ge NC surface atoms Lewis acidic and able to engage in "hypervalent" three-center two-electron bonds with Lewis basic solvent molecules. This hypervalent interaction was found to be critical to colloids stability.

In contrast to the Cl-terminated NC surface, here we employ a more direct strategy to produce a Lewis acidic surface. Monodisperse (within ∼15%) 8 nm Si NCs with a boronated surface are produced by incorporating a boron source (B_2H_6) with SiH_4 during plasma synthesis. TEM shows highly crystalline diamond cubic Si NCs (figure 5.1a and b). Figure 5.2a shows a XPS spectrum of the B(1s) peak of the as-synthesized Si NCs. The spectrum is deconvolved into four peaks wherein the sharpest blue peak at ∼188 eV corresponds to tetravalent boron (B(IV)) that is incorporated into the NC. The two smaller high binding energy peaks are also boron in the B(IV) state, but they are due to boron bonded to an electronegative atom in addition to Si[137]. This is likely due to oxidation of surface boron upon exposure to ambient oxygen and water during sample transfer. This is validated by the Fourier transform infrared (FTIR) spectra in Figure 5.2b, as the peak corresponding to ν(Si-B-O) increases in relative intensity after brief air exposure.

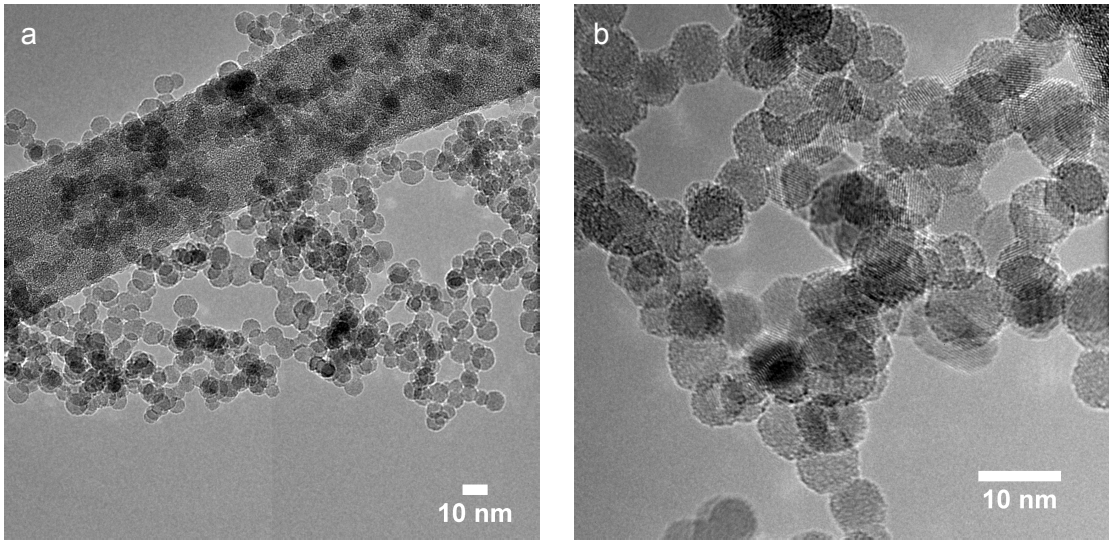

Figure 5.1: **TEM of boronated Si NCs.** Low (**a**) and high (**b**) resolution TEM images of boronated Si NCs.

The broad peak centered at ∼185 eV (red) is unmistakably the trivalent state

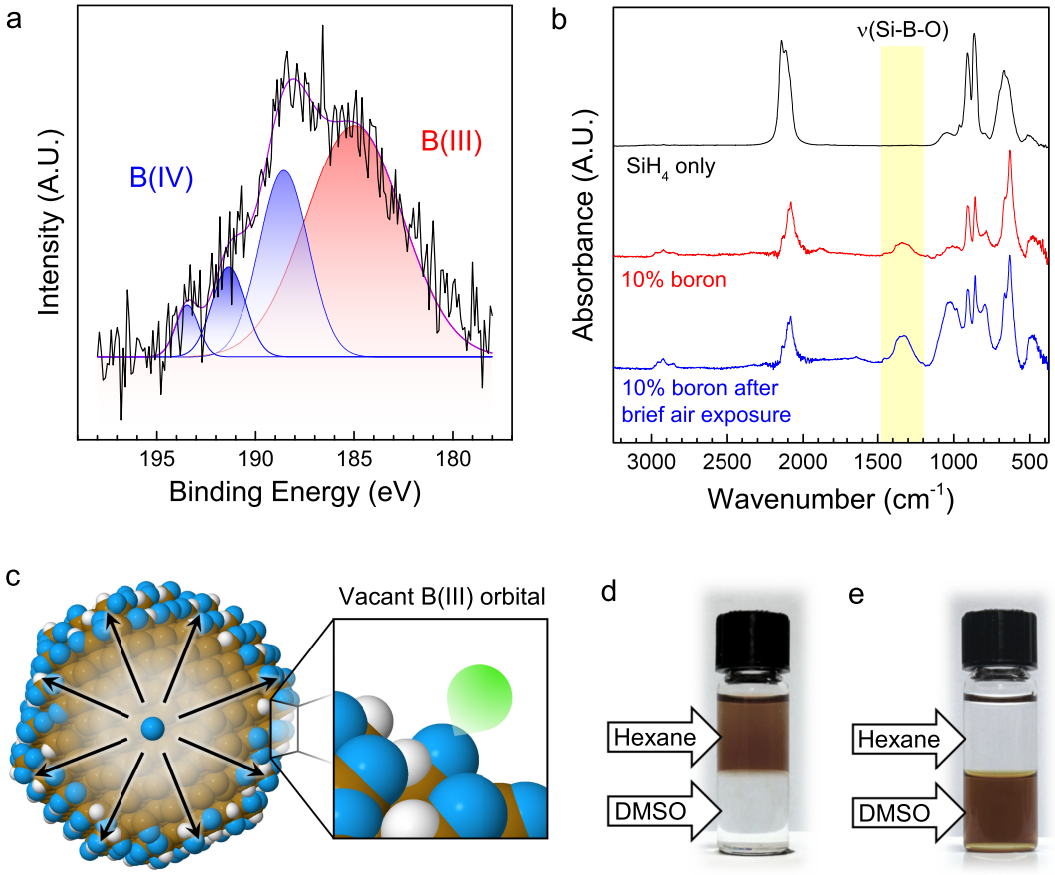

Figure 5.2: **Lewis acidic Si NC surface.** **a**, XPS B1s spectrum of Si NCs as they are produced from the plasma reaction. Surface B(III) accounts for ~60% of the boron in the sample. **b**, FTIR spectra of Si NCs synthesized from SiH_4 only (black), from SiH_4 and 10 atomic percent boron (red), and Si NC sample produced from 10 atomic percent boron after a brief exposure to air. **c**, Cartoon representation of B segregation to the Si NC surface to form Lewis acidic B(III) groups. **d, e,** Photographs of biphasic solutions of hexane and DMSO. In **d**, oleylamine-capped Si NCs are stable in hexane, and in (**e**) Si NCs are stable in DMSO without a ligand.

of boron (B(III))[137]. Peak integration of the XPS spectrum reveals ~60% of the boron is in the B(III) state, which must exist on the Si NC surface. First principles calculations show B atoms to energetically favor surface segregation to the Si NC surface in a trivalent coordination as opposed to substitutional incorporation[138]. In this state, boron has only three valence electrons, while there are four valence orbitals, 2s, $2p_x$, $2p_y$, and $2p_z$. The extra vacant valence orbital make boron a Lewis acid in the classical sense.

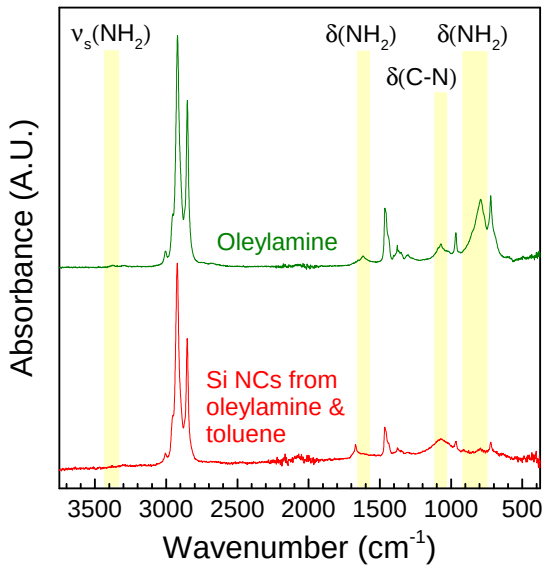

Figure 5.3: **Si NCs with an oleylamine ligand.** FTIR spectra of neat oleylamine (green) and Si NCs dispersed in toluene with an oleylamine ligand (red).

The Lewis acidic Si NC surface is now analogous to that of a metal-based NC. As such, we are able to demonstrate oleylamine ligand coordination to the boron surface sites. After binding ligands to the surface, they can be dispersed in the nonpolar solvents typically used in these systems such as hexane or toluene. Figure 5.2d shows a photograph of a biphasic solution of oleylamine-capped Si NCs dispersed in hexane over dimethylsulfoxide (DMSO). FTIR spectra of SiNCs before and after ligand attachment is also shown in figure 5.3. The oleylamine-capped Si NCs are dramatically different from what

has been previously demonstrated with covalent Si-C-R[58] or Si-O-R[77] ligands.

The remainder of our discussion will focus on the result captured by the photograph in figure 5.2e. Si NC nanopowder obtained from a SiH_4/B_2H_6 reaction containing $\geq$4 atomic percent fractional boron flow will disperse into a stable optically-transparent colloid by simply adding solvent and gently agitating. No long aliphatic ligand is needed. Figure 5.2e shows a biphasic solution of Si NCs stable in DMSO. We have previously established the importance of a Lewis acidic surface[68] for the colloidal stability of plasma-synthesized Si NCs. Surface boron atoms have also previously been recognized as important by Sugimoto *et al.*[139], but its role in colloidal stability was misunderstood as "inorganic atomic ligands." The boron at the Si NC surface plays the same role as a metal atom at the surface of a metal chalcogenide NC. It is an acidic binding site for a Lewis basic heteroatom of a ligand (or solvent molecule); boron itself is not a ligand.

5.3 DLVO Theory

Before further analysis of the Si NC colloids, we briefly introduce the cornerstone of colloidal science–Derjaguin, Landau, Verwey, and Overbeek (DLVO) theory. It can be found in many textbooks[122,140,141]. DLVO is a mean field theory that considers the Gibbs free energy of interaction between two approaching particles in a continuous electrolytic medium of point-charges by evaluating the sum of Van der Waals attraction, ΔG_{VdW}, and repulsion due to the "electrical double layer," ΔG_{EDL}. For ΔG_{VdW}, we employ the classic Hamaker result for two identical spheres[142]:

$$\Delta G_{VdW} = -\frac{A_{212}}{12}\left(d^2\left(\frac{1}{(d+h)^2}+\frac{1}{2dh+h^2}\right)+2ln\left(\frac{d(4a+h)}{(2a+h)^2})\right)\right) \qquad (5.1)$$

where h is the interparticle distance, A_{212} is the Hamaker constant, a NC material and medium dependent constant that determines the magnitude of

attraction. A_{212} can be calculated for bulk materials from dielectric data using Lifshitz theory[143]. However, one must be careful to apply Lifshitz theory to the size-dependant dielectric properties of quantum-confined NCs.

The ΔG_{EDL} component is determined by solving the nonlinear Poisson-Boltzmann equation for the electrical double layers surrounding two approaching particles[140]. It must be solved numerically for an exact solution[144]. For this discussion, we employ the Derjaguin approximation with a constant surface potential boundary condition, which is known to *overestimate* the electrical double layer repulsions for the highly curved surfaces of nanoparticles[145,146]. This point will be important for later discussion. We have:

$$\Delta G_{EDL} = \frac{32\pi d k_B T n_i}{\kappa^2} \tanh\left(\frac{e\Psi_0 z}{4k_B T}\right)^2 e^{-h\kappa} \tag{5.2}$$

where k_B is the Boltzmann constant, T is temperature, and Ψ_0 is the potential at the particle surface. $\kappa^{-1} = \sqrt{\epsilon\epsilon_0 k_B T/(2e^2 z^2 n_i)}$ is the Debye length, the characteristic decay length of electrostatic screening from a charged surface where ϵ is the relative permittivity of the dispersing medium, ϵ_0 is the permittivity of free space, e is the elementary charge, z is the electrolyte valence, and $n_i = 10^3 e^2 N_A z^2 C_i$ where N_A is Avogadro's number, and C_i is the electrolyte molarity. An immediate observations one can make is that the Debye length, κ^{-1}, and thus the double layer, decreases with increasing electrolyte concentration. Secondly, both free energies, ΔG_{EDL} and ΔG_{VdW}, decrease with decreasing diameter of the particle.

5.4 Characterization of silicon nanocrystal colloids

Boronated Si NCs will form extremely dense colloids (>50 mg/ml) when dispersed into strong Lewis basic solvents such DMSO, N-methylpyrrolidone (NMP), or dimethylacetamide (DMA). ζ-potential measurements show the Si NCs acquire

a charge that depends on which solvent is used. The charge is always negative, which is expected due to charge transfer from the Lewis basic solvent[147]. However, we find ζ-potential is not a good indicator of stability (e.g. a larger zeta potential does not necessarily provide better stability.) We systematically investigate Si NC stability by intentionally adding a monovalent electrolyte to the Si NC dispersion.

Figure 5.4a shows the ζ-potential of a Si NCs dispersed in a sodium iodide (NaI) electrolyte in DMSO of varying concentration. The average ζ-potential decreases toward zero with increasing electrolyte concentration, but the large variation in measurements make it difficult to claim a definitive trend. Dynamic light scattering (DLS) is performed on the same dispersions to monitor any agglomeration effects due to the added electrolyte. The error bars show the smallest peak position and largest peak position over the course of ten measurements. As expected the peak position never goes below the NC size determined by TEM, but the larger solvodynamic diameter either reflects many layers of solvent moving with the NC or small, soft agglomerates of NCs. This remains unchanged until a critical coagulation concentration (CCC) is reached. In NaI electrolytes, Si NCs colloids remain optically transparent up to 0.25 M where the dispersion becomes cloudy. At 0.5 M, the NCs agglomerate and settle to the bottom of the vial.

Figures 5.4c and d show the results for the same study using the larger cation electrolyte, cesium iodide (CsI). Similar behavior is observed, but the NCs remain optically transparent up to 0.25 M. For both electrolytes, the NCs are stable at extremely high electrolyte concentrations. 0.1 M and 0.25 M electrolytes corresponds to Debye lengths of κ^{-1}=0.74 nm and κ^{-1}=0.47 nm, respectively. The double layer has collaped to lengths approaching a single DMSO molecule (δ_{DMSO}=0.38 nm). Under these conditions, it is safe to approximate $\zeta = \Psi_0$. Regardless of the A_{212} chosen for the system, conventional DLVO does not predict a stable colloid under these extreme conditions.

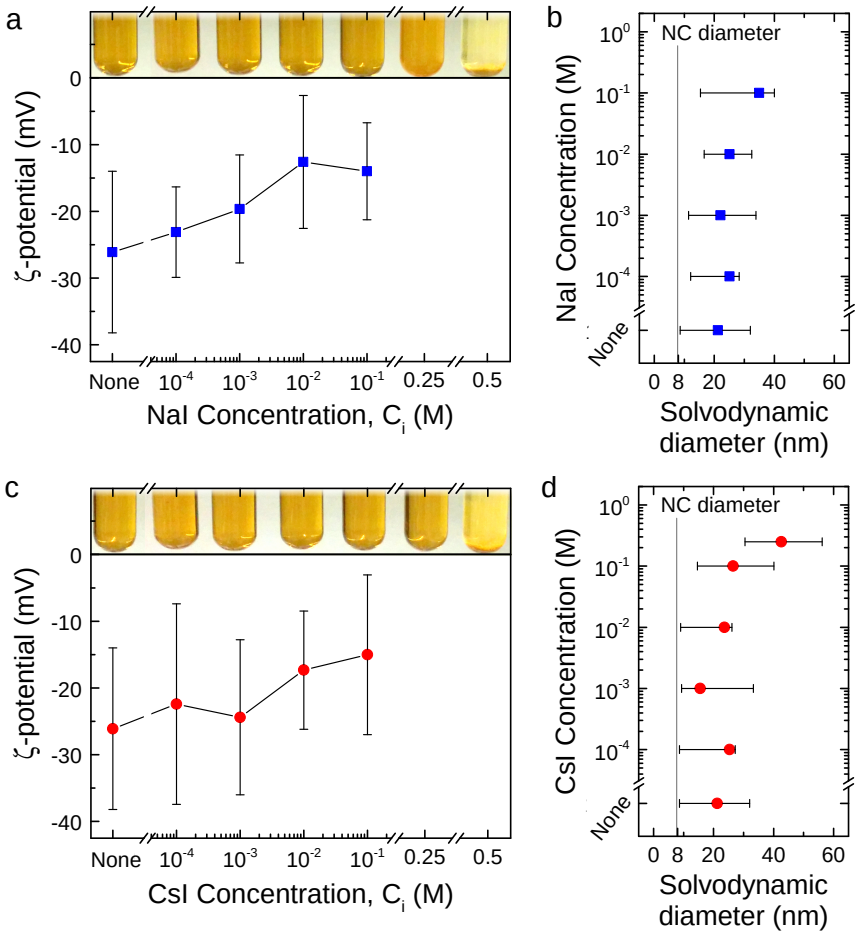

Figure 5.4: **Electrolyte effects on colloidal stability.** **a**, ζ-potential as a function of electrolyte (KI) concentration, and DLS spectra (**b**) at the corresponding electrolyte concentrations. **c** and **d** show the same experiment for a CsI electrolyte.

5.5 The challenge of electrostatic stability

We now step back from our Si NC system and take a general survey of the observations in the NC community developing ligand-stripped NCs[135,136] or NCs with inorganic ligands[6,39–42]. After measuring a ζ-potential, the prevailing opinion in the colloidal NC literature is to conclude colloidal stability is due to electrical double layer repulsions[6,39–42,136] as described by DLVO theory. The heuristic value of $\zeta \approx \pm 30$ mV has been repeatedly cited as justification[39,42]. Certainly electrostatics contribute to stability, but a simple analysis shows it is unlikely that this repulsive force is acting alone.

We begin with a model of colloidal particle agglomeration due to Brownian motion. This effect is summarized by the half-life, $t^s_{1/2} = t^f_{1/2} W$, which describes the amount of time for all singly-isolated particles in a volume fraction, ϕ, of diameter, d, to collide with another particle to form a dimer where $t^f_{1/2} = \pi \mu d^3/(8 k_B T \phi)$. This is the well-known von Smoluchowski result[148] where μ is the viscosity of the medium. W is the stability ratio, which is defined as the number of collisions between particles divided by the number of collisions that result in coagulation.[148]. According to DLVO, particles that collide fall into a deep primary minimum and are assumed to be bound to one another with no probability of returning to the isolated state[140]. If only DLVO forces are considered, a convenient but not limiting approximation for the stability ratio is[149]: $W \approx (\kappa d)^{-1} exp(\Delta \mathrm{G_b}/(k_B T))$. The colloid half-life is now a convenient function of the kinetic barrier height to agglomeration, $\Delta \mathrm{G_b}$.

In figure 5.5a, colloid half life, $t^s_{1/2}$, is plotted as a function of particle diameter for a 10 mg ml^{-1} gold colloid in a 0.01 M water electrolyte (z=1). Diameters of interest for NCs (d$\leq$10 nm) are highlighted in yellow. The strong dependence on diameter ($t^s_{1/2} \propto d^2$) make stabilizing NCs exceedingly difficult without a significant barrier to agglomeration ($\Delta \mathrm{G_b} > 20 k_B T$). For instance, for barrier height of $\Delta \mathrm{G_b} = 20 k_B T$, a colloid of 1 μm gold particles is predicted to remain stable for nearly 8 years whereas a 10 nm gold particle will remain stable

for ∼7 hours. On the other hand, $G_b = 50k_BT$ would provide a stable colloid of 10 nm Au particles for hundreds of years. A kinetic barrier height $\geq 20k_BT$ greater is routinely achieved in colloidal systems using particles that are 1 μm in diameter or greater[140]. However, this is more challenging at the nanoscale.

We now consider DLVO theory to determine a reasonable barrier height that can be obtained in a nanoscale colloid. Plotting the sum of the free energies in equations 5.1 and 5.2, $\Delta G_{net} = \Delta G_{VdW} + \Delta G_{EDL}$, as a function of distance yields the classic DLVO plot.

For our analysis, we take conservative estimates for typical conditions reported during a phase transfer of 8 nm NCs into a polar electrolyte (ionic ligands or stripping agent). Electrolyte concentrations as high as 0.1 M[39,41] have been reported for phase transfer, and ζ-potential measurements span 20[42] to 80 mV[39] in the resulting colloid. In figure 5.5b, we assume water containing a 1:1 (z=1) 0.01 M electrolyte and a suface potential of ±40 mV. A_{212} is varied over four orders of magnitude. The yellow shaded region encompasses experimental[122] and calculated[150] values of A_{212} across water for the bulk form of many common NC materials including metals (Ag, Au, and Cu), SiC, sulfides (CdS, PbS, and ZnS), and oxides (Al_2O_3, ZrO_2). Even extremely small A_{212} (A_{212}=0.1×10^{-20} J) only show a negligible barrier to NC agglomeration.

In figure 5.5c, the surface potential, Ψ_0 is varied for the A_{212}=10×10^{-20} J system, which is a value between bulk PbS ($A_{212} \approx 5\times10^{-20}$ J) and bulk gold ($A_{212} \approx 40\times40^{-20}$ J) across water. It is not until $\Psi_0 \geq$125 mV that a barrier of $20k_BT$ can be reached. Even by overestimating the electrical double layer repulsion with the Derjaguin approximation, we find extreme conditions are are needed to establish a barrier sufficient for colloidal stability for any meaningful amount of time. This demonstration is precisely why aliphatic ligands have been regularly employed for the colloidal stability of nanoscale systems. Still, the Si NCs here, and an array of NC systems, have demonstrated stability without aliphatic ligands.

A calculation by Talapin *et al.*[41] provides insight. An estimate of nine to

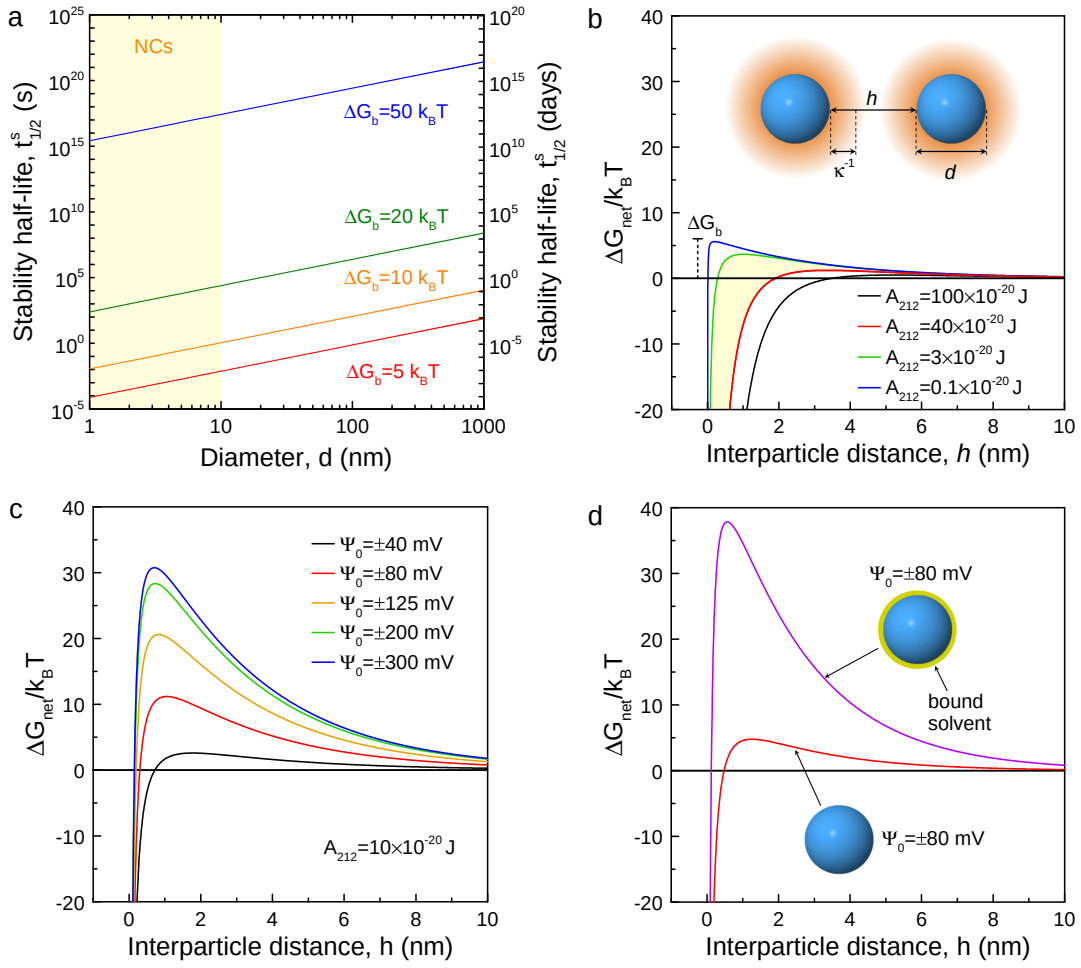

Figure 5.5: **Colloidal force analysis.** **a**, Colloid stability half-life, $t^s_{1/2}$, as a function of diameter, d. **b** and **c** show the net interaction energy in k_BT units as a function of interparticle spacing, h, considering the sum of Van der Waals attraction (equation 5.1) and electrical double layer repulsions (equation 5.2) in water for material systems with different Hamaker constants (**b**) and for a $A_{212}=10\times10^{-20}$ J system with increasing particle surface potential, Ψ_0 (**c**). **d**, Net interaction energy as a function of interparticle distance comparing NCs with and without a bound layer of solvent for a $A_{212}=10\times10^{-20}$ system in DMSO of NCs with a surface potential of $\Psi_0 = \pm80$ mV. All calculations are for 8 nm diameter NCs in a 0.01 M 1:1 (z=1) electrolyte.

eleven elemental charges are calculated to be at the surface of a 4.2 nm NC with S^{-2} ligands. This corresponds to just four or five S^{-2} ligands. If we estimate the diameter of a sulfide ion to be the length of a disulfide bond (0.205 nm), then ∼98% of the NC surface is unaccounted for. Talapin's calculation is derived from the potential at the slipping plane (ζ-potential), which is 1 to 2 solvent diameters away from the surface at 0.01 M, which would only lead to an underestimate in Ψ_0 of ∼17%[151]. This represents only one more sulfide ion at the NC surface. In light of this, we look toward what is most prevalent at the NC surface–the solvent.

In figure 5.5d, we consider 8 nm colloidal gold in DMSO with a surface potential $\Psi_0 = \pm 80$ mV. It should first be noted the red curve shows a $5k_BT$ smaller barrier height in DMSO than the water example in Figure 5.5c. More importantly, the purple curve simulates the effect of a single layer of solvent bound to the NC by shifting the Helmholtz plane by the diameter of one DMSO molecule. This is achieved by replacing h with $h + 2\delta_{\mathrm{DMSO}}$ in the exponential term of equation 5.2[122]. The effect is dramatic. The barrier height is increased by a factor of ∼8. This is an effect of magnified importance at the nanoscale where the Van der Waals attractions are smaller but still extremely strong at short distances. This analysis clearly demonstrates that considering only the electrical double layer to determine NC colloidal stability is an incomplete picture.

5.6 Mechanism of colloidal stability

We have already illustrated why it is difficult to stabilize a NC colloid using electrostatics alone and hypothesize interaction with solvent at the NC surface to play a role. Reports of solvent-dependant stability in metal-based NCs should already raise questions. For the DLVO model outlined above, the solvent is represented as a continuous medium characterized by a single parameter, ϵ. Indeed, ϵ is often cited as the determining factor for a suitable solvent for redispersion after ionic ligand treatment[39,40]. It is no surprise Formamide ($\epsilon = 109$) is often used[6,39–41,152]. However, in these same instances, acetonitrile ($\epsilon =$

35.94)[39,40] is often applied as an "anti-solvent" to flocculate NCs, whereas n-methyl-pyrrolidone ($\epsilon = 32.6$)[42], Dimethylformamide ($\epsilon = 37.06$)[39,42,136], and ethanolamine ($\epsilon = 37.06$)[6] are considered dispersing solvents. In fact, acetonitrile has been used as a dispersing solvent as well[136].

In contrast to solution-synthesized NCs, gas-phase synthesis from hydride precursors yield NCs that are uniquely free of organics. We now have the opportunity to analyze the mechanism of colloidal stability in an environment untainted by solution-phase synthesis, ligand exchange, or other solution-phase chemistries.

Figure 5.6 is a ternary diagram that weighs the relative importance of two solvent characteristics in addition to the relative permittivity–the Lewis basicity and the Lewis acidity. Si NCs are dispersed in eighteen neat solvents (table 5.1). The maximum concentration achieved in each single-solvent system is indicated by bubble color. Relative van der Waals volume of the solvent is indicated by bubble diameter. From this plot, it clear that relative permittivity is not the only determining factor to achieve colloidal stability. For instance, nitromethane ($\epsilon = 36.2$) and water ($\epsilon = 80.1$) provide no stability, and the solvent with the highest relative permittivity, formamide ($\epsilon = 109$), provides limited stability ($\sim$1 mg ml^{-1}).

It was observed previously[68], that Lewis basicity is a strong indicator of colloidal stability for Si NCs with a Lewis acidic surface. For the boronated Si NCs, stongly Lewis basic solvents such as DMSO, DMA, and NMP actually provide limitless stability; NCs can be added to these solvents to form a dense, viscous liquid[155]. However, triethylamine, tetrahydrofuran, and pyridine do no stabilize the NCs, as they have a depreciable relative permitivity. Ethanol, methanol, formamide, and water are also strong Lewis bases. The distinguishing factor with these solvents is they are protic, so they possess a strongly Lewis acidic hydrogen group. Molecules of these solvents are well known to interact with one another *via* self-associating hydrogen bonds.

The observations from figure 5.6 are easily reconciled in a qualitative molecular

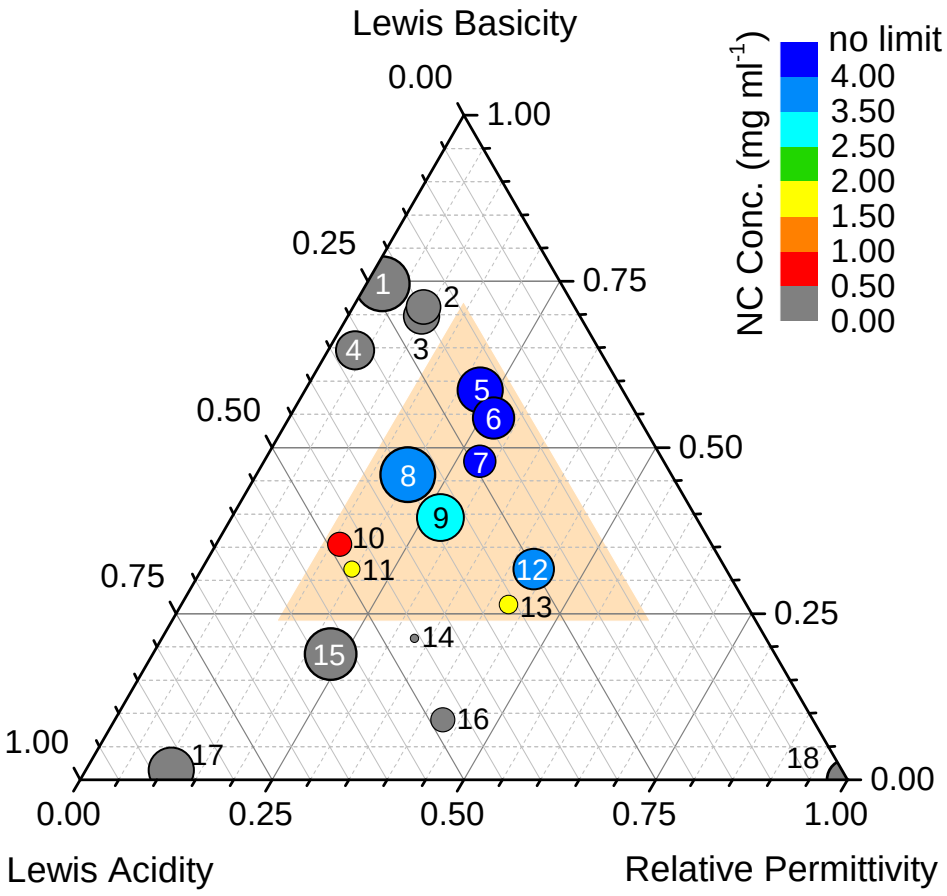

Figure 5.6: **Relevant parameters for colloidal stability.** A ternary diagram that demonstrates the relative impact of three solvent parameters on colloidal stability: Lewis basicity, Lewis acidity, and relative permitivity. Color of the bubble indicates maximum concentration that can be achieved in each solvent determined from UV-Vis absorption, and the bubble size corresponds to the relative van der Waals volume of the solvent. Numbers indicate solvent from table 5.1.

Table 5.1: **Normalized solvent parameters.** Compilation of data used in the ternary diagram of figure 5.6.

Label	**Solvent**	$\boldsymbol{\epsilon}$[a]	**Lewis basicity**[b]	**Lewis acidity**[c]
1	triethylamine (TEA)	0.022	0.817	0.255
2	tetrahydrofuran (THF)	0.069	0.528	0.146
3	pyridine	0.121	0.876	0.259
4	1,4-dioxane	0.021	0.381	0.188
5	N-methylpyrrolidone (NMP)	0.300	0.768	0.243
6	dimethylacetamide (DMA)	0.351	0.716	0.248
7	dimethyl sulfoxide (DMSO)	0.414	0.704	0.352
8	acetophenone	0.167	0.387	0.289[d]
9	benzonitrile	0.231	0.335	0.283
10	ethanol	0.225	0.495	0.677
11	methanol	0.303	0.490	0.754
12	propylene carbonate (PC)	0.577	0.423	0.334
13	formamide	1.000	0.619	0.726
14	water	0.720	0.464	1.000
15	1,2-dicholorobenzene (DCB)	0.095	0.077	0.237[d]
16	nitromethane	0.332	0.070	0.374
17	toluene	0.021	0.003	0.160[d]
18	hexane	0.017	0.000	0.000

[a] ϵ_r is relative permittivity (formerly dielectric constant) normalized to formamide (ϵ=109).

[b] Lewis basicity is determined from $SbCl_5$ affinity scale ($-\Delta H_{SbCl_5}$), which is commonly known as the donor number (DN)[108]. The values are normalized by hexamethyl phosphorotriamide ($-\Delta H_{SbCl_5}$=162.4 kJ/mol).

[c] Lewis acidity is determined from complimentary acceptor number (AN)[153], which is a unit-less scale derived from the phosphorus nuclear magnetic resonance shift of triethylphosphine oxide. The values are normalized by the AN of water (AN=54.8).

[d] Unknown AN values were calculated using a least-squares regression from known parameters found in Kamlet *et al.*[154]

orbital diagram[156] shown in figure 5.7. Here we represent the Lewis acidity as the relative height of the lowest unoccupied molecular orbital (LUMO). Conversely, the height of the highest occupied molecular orbital (HOMO) level represents the relative Lewis basicity of the solvent molecule. The Gibb's free energy of interaction between the NC surface groups and the Lewis basic group of an aprotic solvent molecule (e.g. DMSO, DMA, NMP), $\Delta G_{NC\text{-}A}$, is compared to interaction with a protic molecule (e.g. water, formamide), $\Delta G_{NC\text{-}P}$.

The final molecular orbital alignment is that of the acidic hydrogen of a protic molecule. The free energy of intermolecular interaction (hydrogen bond), $\Delta G_{P\text{-}P}$, is in competition with interactions at the NC surface. When water is added to the boronated Si NCs, they stick to the glassware and remain in an agglomerated state. In this case, it is more energetically favorable for water to hydrogen bond with itself than with the NC surface ($\Delta G_{NC\text{-}P} < \Delta G_{P\text{-}P}$). However, when aprotic solvents such as DMSO, DMA, or NMP are added, which do not possess acidic hydrogens, the NCs immediately disperse in solutions. Water is the extreme case. Other protic solvents that do not inter-hydrogen bond as strongly also provide some stability. However, the competition of these two bonds decreases the maximum concentration of NCs that are stabilized. It is worth noting that NCs with their ligands stripped or with ionic ligands have been shown to be dispersible in water[6,39,40]. It is likely NCs dispersible in water either have a more Lewis acidic surface or have a larger contribution from electrostatics than the Si NC investigated here.

It would seem Lewis acid-base interactions within the solvent and at the NC surface are a powerful indicator of colloidal stability. These interactions are not taken into account in conventional DLVO model, but they have been shown to be "extensions" to the DLVO model[151]. The collective effect of these molecular-scale interactions yields a macroscopic force that is manifested as a strong short-range repulsion or attraction[122,151]. It is referred to as solvation (hydration in the case of water). It is well known to exist experimentally[122] and shown empirically to be an exponential function of distance from the surface: $\Delta G_s = \Delta G_{AB} e^{d_0 - d/\lambda}$ where λ

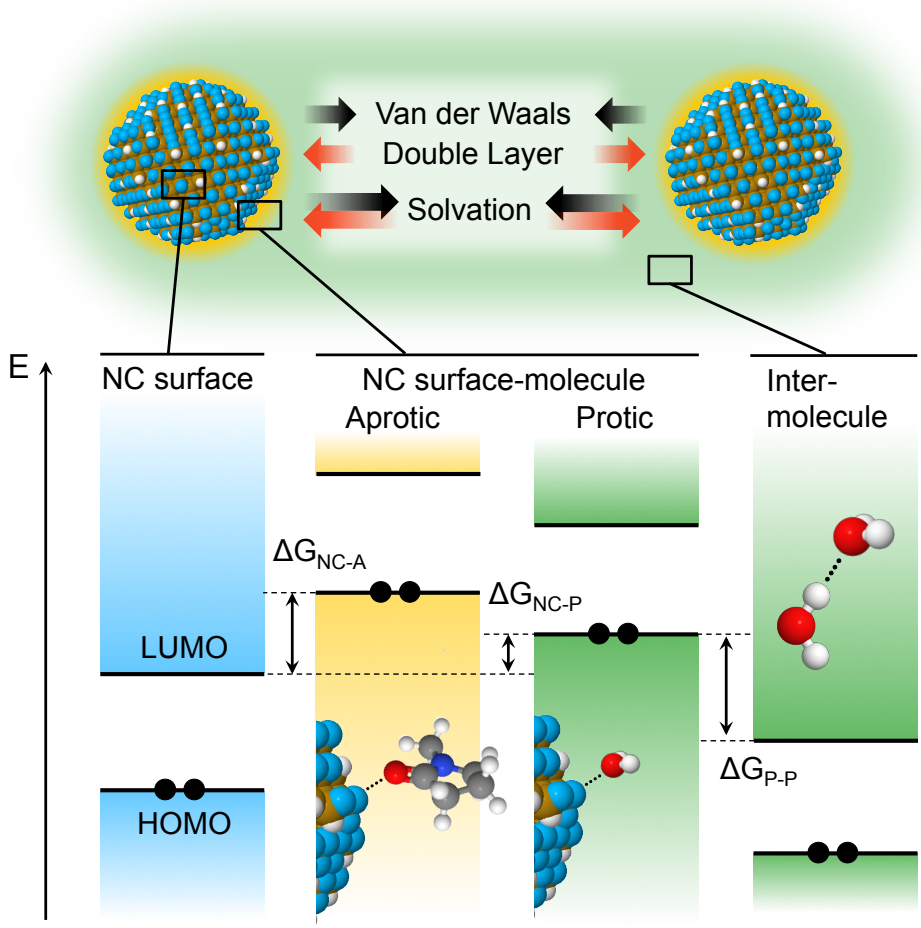

Figure 5.7: **Impact of molecular interactions on colloidal stability.** Schematic illustrating inter-particle forces and molecular interactions that must be considered to form a stable NC colloid. Molecular interactions, which give rise to solvation, are presented in the form of a qualitative molecular orbital diagram.

is the "solvent correlation length", an empirical parameter which has been shown to be between 0.6 nm and 1.1 nm[157,158] for repulsion in water, d_0 is the minimum separation due to Born repulsion (=0.158 nm), and ΔG_{AB} is the free energy of acid-base interaction per unit area (mJ m^{-2}).

This theory is nicely consistent with the conclusions drawn from the ternary diagram (figure 5.6) and the molecular orbital model (figure 5.7). The free energy of acid-base interaction, ΔG_{AB} can be positive or negative, which corresponds to an attractive (often referred to as hydrophobic) or repulsive (hydrophilic) force, respectively. This is the competition between $\Delta G_{NC\text{-}P}$ and $\Delta G_{P\text{-}P}$ just discussed. A $\Delta G_{P\text{-}P} > \Delta G_{NC\text{-}P}$ (positive ΔG_{AB}) leads to an attractive potential, whereas $\Delta G_{P\text{-}P}$ is negligible in an aprotic system and a repulsion is realized.

In comparison to electrical double layer forces, intermolular interactions play an increasingly dominant role in nanoscale colloids. This is perhaps not surprising. The strengths of most hydrogen bonds lie between 5 to $10k_BT$ per bond at 298 K[122], which is comparable to the barrier heights we have considered for DLVO theory. Indeed, Non-DLVO effects such as charge-inversion have been previously observed in NC systems[41]. Charge inversion phenomena is typically attributed to solvation forces[159,160]. From this work, it is clear that careful consideration of the solvent is necessary to control the colloidal forces needed for the stability NCs without ligands. The first layer of solvent at the NC surface is of utmost importance. While still debated[161], it is hypothesized that the entropic penalty for removing the first layer of solvent is the source of solvation forces[162]. This hypothesis is validated in the following section.

5.7 Colloidal stability in an array of media

We demonstrated the dramatic effect a single layer of bound solvent can have on colloidal stability. We now investigate this further by demonstrating the effect of bound solvent spectroscopically. In figure 5.8a Si NCs stabilized in NMP are dropped onto an attenuated total reflectance (ATR) crystal, and the FTIR signal

of the C=O stretching mode is monitored as a function of time. As the NMP evaporates, the C=O mode redshifts from its freely vibrating energy at 1690 cm^{-1} to ~1650 cm^{-1}, which is an indication of electron density transfer from the Lewis basic C=O group to a Lewis acidic B(III) group of the Si NC surface to form a weak acid-base complex[156].

After binding a Lewis acidic molecule to the surface, the Si NCs can now be stabilized in any miscible solvent. Certainly cosolvents within the orange triangle of figure 5.6 will provide stability. The important observation is that cosolvents that do not provide any stability on their own can now be used. Figure 5.8b shows illustrative examples of 50% volume mixtures. When a solvent that provides colloidal stability is first added, the Si NCs can now be diluted with solvents such as water, nitromethane, pyridine, and toluene. This covers relative permittivities from ϵ=80.3 (water) down to ϵ=2.3 (toluene). Si NCs first stabilized in DMSO are stable in 95% toluene. It would seem the characteristics of the cosolvent are of negligible importance to the solvent interacting with the NC surface. Interestingly, this observation was actually briefly reported previously by Dong *et al.* who noticed NCs would stabilize in water only if dimethylformamide is added as well[136]. This lends credence to the universal applicability of the conclusions drawn in this work.

The FTIR spectra of figure 5.8c illustrate a particularly attractive cosolvent system of NMP and water. Water-stable NCs are desirable for biocompatibility and cost reasons. We can demonstrate Si NC stability in solutions of 94% water by first forming a highly concentrated solution in NMP, then diluting with water. Even at high volume fractions of water, signal from NMP molecules can be prominently observed in the FTIR spectrum. Interestingly, even at 10% water by volume, the surface of the Si NCs remain unoxidized. It appears the boronated NC surface in addition to the NMP molecules bound to the surface through an acid-base complex actually protect the Si NCs from oxidation. This is observed by a lack of Si-O-Si vibration at 1090 cm^{-1}. Si NCs are typically extremely reactive in ambient air atmosphere[96], but these solutions were stored

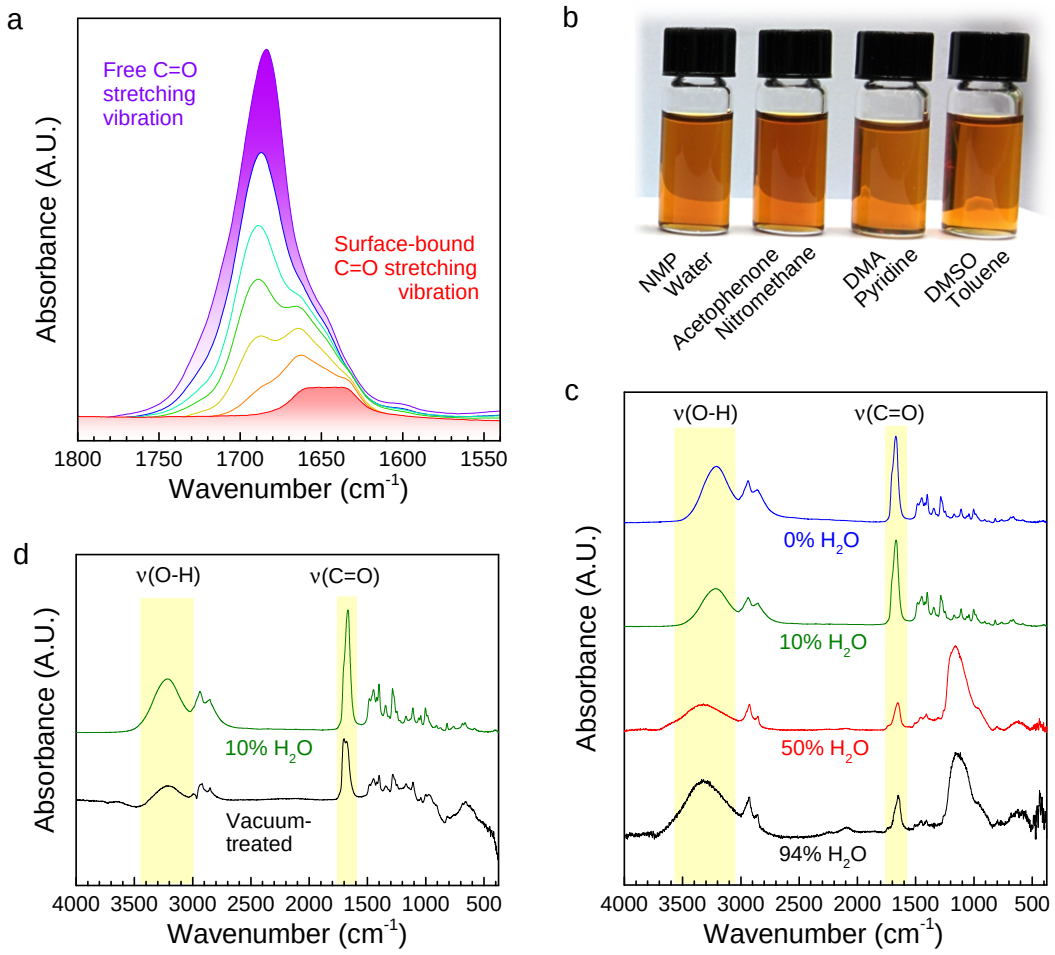

Figure 5.8: **Cosolvent effects on colloidal stability.** **a**, FTIR spectra of the C=O stretching vibration of NMP taken as a function of time as NMP evaporates from Si NC colloid. **b**, A photograph of 50% volume mixtures of a variety of cosolvent systems. **c**, FTIR spectra for films of Si NCs cast from NMP/water mixture of varying volume fractions. Spectra are normalized and offset for clarity. **d**, FTIR spectra of Si NC film cast from a solution of NMP and 10% water by volume before (green) and after (black) vacuum-treating the sample. Spectra are offset.

in ambient condition for weeks before FTIR was measured. Moreover, figure 5.8d shows that simply pulling modest vacuum ($\sim 10^{-3}$ torr) will remove adsorbed water from the surface of the NC. This will be an important attribute for further development of optoelectronics device-quality thin films cast from these colloids.

5.8 Conclusion

We began this work by introducing a versatile Lewis acidic B(III) surface chemistry. Colloidal stability with a typical ligand-binding scheme for stability in non polar solvents was shown. We then used the Si NCs as a model system to explore the mechanism of stability in polar solvents. We find the Lewis acidity of the NC surface, and its interaction with Lewis basic groups of solvent, to be of paramount importance. Insights into the role of the solvent on colloidal stability clarify some of the disparate observations reported for electrostatic colloidal stability of ligand-stripped NCs or NCs with ionic ligands bound to their surface. For colloidal stability to occur, bound ionic ligand or not, careful consideration of the solvent properties beyond the relative permittivity must be made. Molecular interactions must be considered for achieving a stable colloid. We concisely show this with molecular orbital model and demonstrate the ability to achieve stability in solvents that vary from toluene to water. Given the great breadth of NC materials explored using ligand stripping or ionic ligands, it is difficult to claim generality to our observations. Still, we have demonstrated that achieving colloidal stability in NC systems using an electrical double layer alone is exceedingly difficult. This insight is important in the design and further development of colloidal NCs for optoelectronics.

5.9 Experimental methods

Si NC synthesis. Si NCs are synthesized in a continuous-flow nonthermal plasma reactor from gas mixture of argon, silane, and diborane. The gas flows

through a borosilicate glass tube with a pair of copper ring electrodes secured to it. Typical flow rates are 30–50 standard cubic centimetres per minute (sccm) of argon, 0.4–0.6 sccm of silane, 0–2 sccm of diborane diluted in hydrogen (10%). 13.56 MHz radiofrequency power at 110 to 130 W is supplied to the ring electrodes to strike a plasma and yield crystalline Si NCs. A rectangular nozzle controls the gas pressure in the plasma region by restricting the flow. Adjusting the width of the nozzle opening allows for the pressure to change independently of the gas flow. This method is used to produce nanocrystals at reactor pressures ranging from 90 to 150 Pa. As a result, the nanoparticle size can be precisely controlled between 5 and 15 nm. 8 nm Si NCs are used throughout this study.

Si NC collection and colloid formation. Powder samples of silicon nanocrystals are collected directly from the gas-phase by impacting them onto a substrate mounted onto a manual feed-through located inside the reactor. A rectangular nozzle is placed in between the deposition and plasma region to accelerate the particles and impact them directly onto the substrate. The substrate is then retracted into a portable loadlock and transferred air-free to a N_2-purged glovebox for further processing. Si NCs are weighed and dispersed in various solvents.

XPS. XPS spectra are acquired on a Surface Science Laboratories, Inc. SSX-100 XPS with a monochromatic Al K_α X-ray source. A X-ray power of 200 W with a 1×1 mm^2 spot size was used. Si NC samples are prepared by directly impacting a <50 nm thin film of Si NCs onto a Au-coated Si wafer. B1s peaks were obtained taken by integrating scans for $\sim$6 hours. Peaks are assigned by using the C1s peak as a reference at 285 eV.

Chemicals. The following solvents were purchased from Sigma Aldrich (purity and grade are included if available): triethylamine (99%, ACS), tetrahydrofuran ($\geq$99.9%, anhydrous), pyridine ($\geq$99.8%, puriss), 1,4-dioxane (99.8%,

anhydrous), dimethylacetamide (99.9%, puriss), dimethyl sulfoxide (≥99.9%, ACS), benzonitrile (99%, Reagent Plus), ethanol (99%, anhydrous), methanol (99%, anhydrous), propylene carbonate (PC) (99.9%, HPLC), formamide (≥99.5%, ACS), water (deionized), 1,2-dicholorobenzene, (99%, anhydrous), nitromethane (≥98.5%, puriss), toluene (99.9%, HPLC), hexane (≥95%, spetrophotometric). The following solvents were purchased from Acros Organics: N-methyl-2-pyrrolidone (99%), acetophenone (98%, extra pure) Sodium Iodide (ACS) was purchased from J.T. Baker and dehydrated by pulling vacuum on a schlenkline and heating to 150°C. Cesium Iodide (99.998%, ultra-dry) was purchased form Alfa Aesar and used as received. 1.5 M stock solutions of DMSO electrolyte were prepared in a N_2-purged glovebox by stirring the salt with a magnetic stir bar until the solution turned clear.

ζ-potential. Electrophoretic mobility was evaluated on a Brookhaven ZetaPALS instrument using phase-angle light scattering with varied conditions between 1 V and 10 V at frequencies between 2 and 20 Hz depending on the stability response of the colloids. 10 runs of 10 cycles were averaged to obtain a mean and standard error. 0.1 mg ml−1 Si NC colloids were used. At electrolyte concentrations of 0.1 0.25 M, electrode corrosion became an issue. ζ-potential values were evaluated from the electrophoretic mobility by applying Henrys equation. Relative permittivities were obtained from the Landolt-Börnstein Database[112].

DLS. The DLS spectra were acquired 90° with a Brookhaven ZetaPALS instrument. Measurements tended to drift between ∼9 nm and ∼20 nm peak solvodynamic diameter for the Si NC samples investigated here. This behavior was checked against a NIST standard 92 nm ± 3.7 nm polymer microspheres in water as well as for Si NCs with a dodecane ligand stabilized in toluene. No drift was observed in either case, so the irregularity was concluded to be a component of the system.

Colloid Concentration. UV-Vis absorption of centrifuged Si NC solutions was performed on a Cary 5E UV-Vis spectrophotometer. Centrifugation was done at 4000 rpm for up to 30 minutes. After centrifugation, optically transparent solutions indicate insignificant scattering, and the Beer-Lambert law ($A = \epsilon lc$) is employed to determine mass concentration from absorption by integrating the absorption spectra (Supplementary Figure S7) between 550nm to 800nm. The absorbance, A, is linearly dependent on concentration, c. The path length through the solution, l, and the extinction coefficient, ϵ, are constants. A was determined by integrating under the absorbance curve. The absorbance of 5 mg of Si NCs in 3 ml of DMSO, A_b, did not change after centrifugation, so the concentration, c_b, was known. It was used to determine the unknown concentration, c_o, of other solutions relative to Si NCs in DMSO. After subtracting the background solvent, the concentration of other solutions is obtained from: $A_o/A_b = c_o/c_b$.

FTIR. FTIR experiments were done on a diamond ATR crystal or using the diffuse reflectance attachment on a Bruker Alpha FTIR spectrometer inside a N_2-atmosphere glovebox. Spectra were typically collected by averaging 20 scans at 2 cm^{-1} resolution.

Calculations. Brownian agglomeration and DLVO calculations were done using Mathematica 9. The open-source software Jmol was used to evaluate the Van der Waals volume in figure 5.6.

5.10 Future work

The next big step of this work is to demonstrate good electronic transport properties in films cast from the colloids developed here. Preliminary work on

this is underway in a soon-to-be published paper by Ryan Gresback, Nicolaas Kramer, Uwe Kortshagen, and Tomohiro Nozaki. Ting Chen and Nicolaas Kramer have also begun work investigating thin film transistors and spray-coating film deposition strategies. Ideally an optoelectronic device such as a solar cell or LED could be fabricated and optimized. Before this can be achieved, the optical properties of these materials should be better understood. This is especially the case since dopants are incorporated and active in the NCs. Ideally, the boron surface chemistry would be decoupled from dopant incorporation. Nicolaas Kramer has done some preliminary work on this by sputtering a B-rich amorphous film after the Si NCs have been synthesized in an upstream plasma. A strategy of this nature is promising.

If the first layer of solvent remains on the Si NC surface after film deposition, then it likely be should be removed when cast into a film for optimal transport. An interesting area of investigation, however, would be instead to use a conductive molecule at the NC surface. A first order attempt should be with acetophenone, which is the only conjugated, and thus conductive, molecule of the ones explored in this work.

An accurate calculation for the electrical double layer potential will be important for a more quantitative evaluation of electrostatic stability of NC systems. This work is currently underway to be included with a version of this work submitted for publication. My brother, Vincent Wheeler, is an expert at numerical solutions to nonlinear differential equations. We are working together to develop a general two-dimensional finite elements code to solve the Poisson-Boltzmann equation. This will be a valuable tool for future research in the analysis of NC colloidal stability in addition to what was explored here.

Chapter 6

Germanium Nanocrystal Surface Passivation

> "*The real purpose of the scientific method is to make sure Nature hasn't mislead you into thinking you know something you don't actually know.*"
> -Robert M. Pirsig

6.1 Introduction

Until this chapter, we have considered surface chemistry in regards to interaction with molecules for colloidal stability. However, the original motivation for this work is for applications in optoelectronics. Quantum-confinement effects on the optical absorption and emission properties of Silicon, with a bulk bandgap of 1.1 eV, are well-established[14,58,60]. However, narrow bandgap semiconductor nanocrystals (NCs) have gained increasing interest. In particular, emerging strategies for solar energy conversion, such as multiple exciton generation[163] and hot electron transfer[164], require a narrower bandgap than conventional devices to maximize efficiency. Light emission properties are also important for bio-imaging applications[165], and emission from Ge NCs can potentially be tuned to operate

from longer telecommunications wavelengths out to visible wavelengths.

The bulk bandgap of germanium of 0.67 eV and its relatively large exciton Bohr radius of ∼24 nm make it sensitive to quantum confinement effects and an excellent candidate for such applications. Quantum confinement is commonly observed in the absorption properties of Ge NCs in solution[67], embedded in a matrix[11,166], as well as free-standing Ge NCs assembled into films[66]; however, room temperature size-tunable bandgap photoluminescence (PL) from Ge NCs remains elusive, and only a few instances have been reported[9–11].

Non-radiative trap states at the Ge NC surface are a likely source of this difficulty. When emission is observed, it is often caused by surface trap state emission[167,168]. In light of this, several schemes have been adopted for chemical passivation of the Ge surface. Ge-H surface groups will react with alkenes and alkynes to form a Ge-C-R surface termination. This has been demonstrated for planar Ge[82,169] as well as nanowires[170] and nanocrystals[65]. Ge-S-R functionality can be achieved using alkanethiols in a similar reaction[170,171]. Alkylation is also realized using a two-step approach where the Ge surface is first terminated with a halide for subsequent reaction with an alkyllithium or Grignard reagent[170–173]. A single-step method using Grignard chemistry has also been demonstrated following colloidal synthesis of Ge NCs from halogenated precursors[174,175].

In this work, surface chemistry control provided by nonthermal plasma synthesis allows for a similar single-step approach to chemical passivation of the Ge NC surface. The strategy is summarized in figure 6.1. Ge NCs are terminated with chlorine as a result of gas-phase decomposition of $GeCl_4$ in the presence of H_2[55]. As-synthesized Cl-terminated Ge NCs are dispersible in select solvents[83] but exhibit no measurable PL. However, near infrared (NIR) bandgap emission is achieved after employing a simple surface passivation scheme, in which a Grignard reaction between native Ge-Cl surface groups and alkyl magnesium bromide yields a Ge NC surface terminated with alkyl groups. The passivation is applied to Ge NC sizes ranging from 4.8 nm to 10.2 nm, and peak bandgap emission is thus tuned between 0.71 eV and 1.03 eV with narrow

emission widths on the order of 0.2 eV.

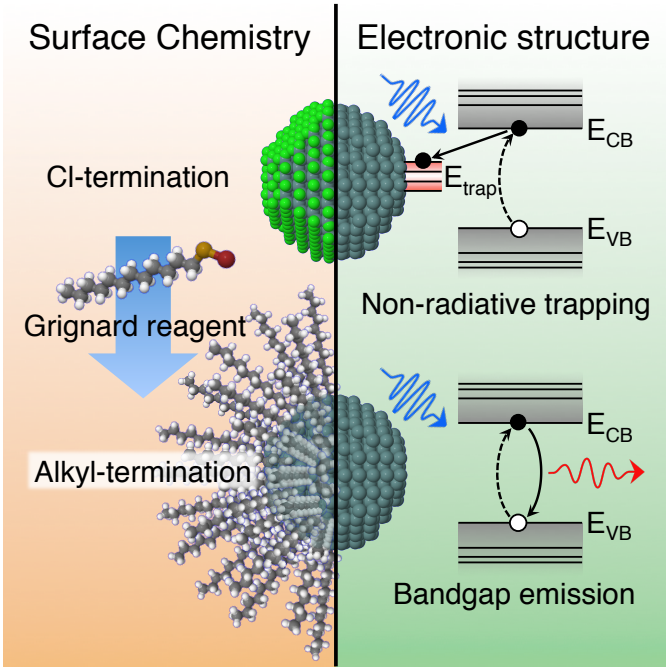

Figure 6.1: **Surface passivation strategy.** A cartoon illustrating the effect of surface chemistry on the electronic structure of the Ge NCs. Proper surface passivation is necessary to achieve tunable bandgap emission.

6.2 Surface passivation chemistry

Figures 6.2a and b show the Fourier transform infrared (FTIR) spectrum of 6.8 nm Ge NCs immediately following synthesis (black spectrum). The dominant feature of of this spectrum is at 483 cm^{-1}, which corresponds to the stretching mode of the Ge-Cl_x bonds. Ge-H_x stretching modes are also present and centered at 2100 cm^{-1}. The shoulder at 1900 cm^{-1} is likely due to lower energy vibrations of Ge-H_x modes in the presence of Cl. Bonds between 500 cm^{-1} and 1000 cm^{-1} are higher order Ge-Cl_x and Ge-H_x deformations.

Exposing as-synthesized Ge NCs to an alkyl magnesium bromide solution results in immediate bubbling of the solution, which indicates the onset of

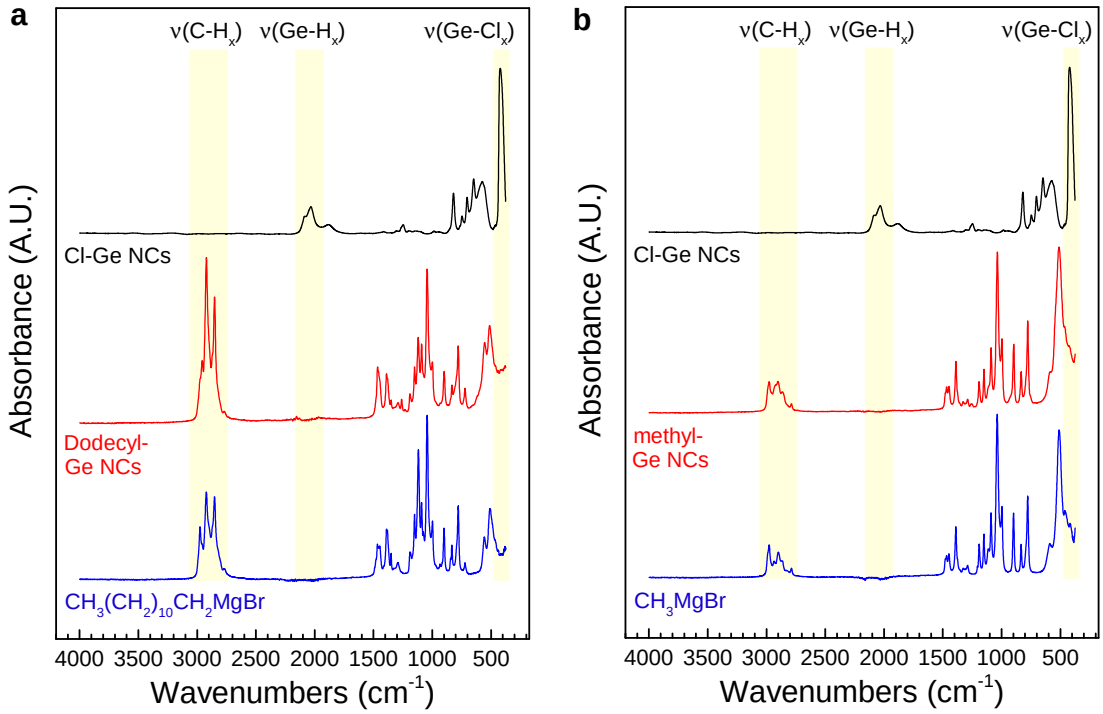

Figure 6.2: **FTIR spectra of dodecylmagnesium bromide chemistry.** The dominant features in the FTIR spectrum of as-synthesized Ge NCs (black) is the stretching vibration of the the Ge-Cl$_x$ and Ge-H$_x$ surface groups. This feature is no longer observed after chemical passivation to yield dodecyl-terminated Ge NCs (**a**) or methyl-terminated Ge NCs (**b**), and the C-H$_x$ stretching modes become the dominant feature. The spectrum of unreacted $CH_3(CH_2)_{10}CH_2MgBr$ (blue) is included for reference. The peaks between 600 cm^{-1} and 1500 cm^{-1} are due to vibrational modes of diethyl ether and deformation modes of the C-H$_x$ groups. Spectra are normalized and offset for clarity.

exothermic reaction without activation. When using dodecylmagnesium bromide, a transparent brown solution is formed as the dodecyl groups bond to the surface and provide a steric barrier to agglomeration for colloidal stability (figure 6.2a). FTIR suggests successful reactions with methyl magnesium bromide were also achieved (figure 6.2b), but the methyl termination does not afford a significant barrier to agglomeration and a stable colloid is not attained. Subsequent PL and absorption studies are thus carried out on dodecyl-terminated Ge NCs in solution. For both reagents, the solution is refluxed in excess diethyl ether at 80 °C for an additional two hours to ensure complete reaction.

The red FTIR spectrum of figures 6.2a and b show the Ge NCs after reaction with alkylmagnesium bromide. The disappearance of the Ge-Cl_x modes is an indication of a complete reaction. The Ge-C stretching mode should appear at 700 cm^{-1}[1176], but the absorption features from the unreacted Grignard reagent dominate the fingerprint region of the spectrum. However, increase of the C-H_x vibrational modes relative to those in the fingerprint region of the alkylmagnesium bromide (Fig. 6.2a and b, blue) is also an indication of a successful reaction. In particular, the sharp feature at 1090 cm^{-1} decreases in absorption intensity relative to the C-H_x modes. This is the C-O-C stretching mode of diethyl ether that is complexed to the magnesium atom of unreacted $CH_3(CH_2)_{10}CH_2MgBr$ precursor.

Interestingly, the Ge-H_x vibrational modes are not present in the resulting dodecyl-terminated Ge NC spectrum. Alkylization of Si-H groups with Grignard reagents has been observed[177] and is attributed to a radical reaction pathway in which alkyl halide impurities lead to the generation of reactive alkyl radicals.[178]. The observation of a passivated Ge NC surface that leads to PL suggest this chemistry also takes place at Ge-H groups of the Ge NC surface. The importance of a Ge-C covalent bond was hypothesized in previous work[9]. Indeed, the only instances of room temperature bandgap emission from free-standing Ge NCs feature Ge-C-R surface groups[9,10].

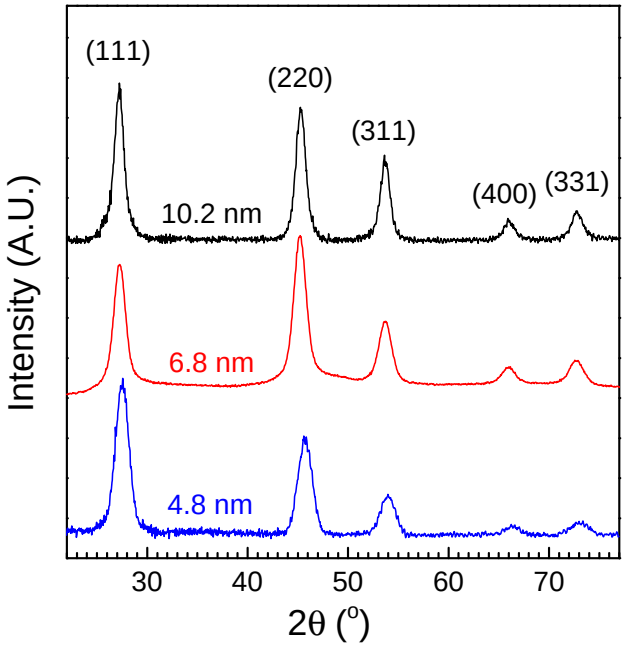

Figure 6.3: **X-ray diffraction spectra of Ge NC samples**. Diameters labeling each spectra were determined from the Scherrer broadening of the peaks. Spectra are normalized and offset for clarity.

6.3 Bandgap emission

Alkyl passivation chemistry was performed on Ge NCs that were 10.2 nm, 6.8 nm, and 4.8 nm in diameter. NC size is determined by residence time in the plasma, which is experimentally controlled by varying flow rates and reactor pressure. Average NC diameter is then evaluated by Scherrer broadening of the x-ray diffraction (XRD) spectra shown in figure 6.3.

UV-Vis absorption and PL spectroscopies were performed on solutions of dodecyl-terminated Ge NCs. The results are presented in figure 6.2. The peak PL emission of 10.2 nm Ge NCs (solid black spectrum) resides at 1610 nm, which is blue-shifted from the bulk Ge bandgap. Decreasing NC diameter to 6.8 nm (maroon spectrum) and 4.8 nm (red spectrum) blue-shifts emission to shorter wavelengths of 1360 nm and 1200 nm, respectively. This is consistent

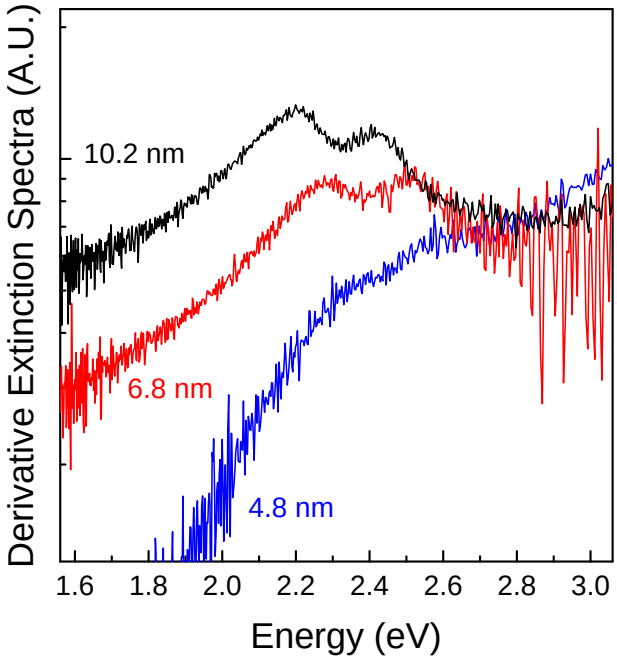

Figure 6.4: **Confinement in Ge NC absorption** Derivative of the extinction spectra. A blue-shift of the E_1 direct transition at the L point with decreasing size due quantum-confinement effects is observed. Spectra are normalized and offset for clarity.

with quantum confinement models[179] as well as previous reports of bandgap PL[9–11]. PL due to radiative surface states are typically observed at much shorter wavelengths[11]. Moreover, previous observations likely due to surface trap emission have shown PL emission dependence on excitation energy[174]. The PL emission shown in this work is independent of excitation energy.

Unfortunately, corroborating PL emission with the onset of absorption was not achieved. This is likely due to by-products of the Grignard reaction that dominate the longer wavelengths of the spectrum. However, evidence of expected confinement effects can be observed in the first derivative of the extinction spectra by a shift in the direct band E_1 transition peak as predicted by Mie theory[180,181]. Figure 6.4 shift of the E_1 transition is observed between 2.0 and 2.7 eV, which

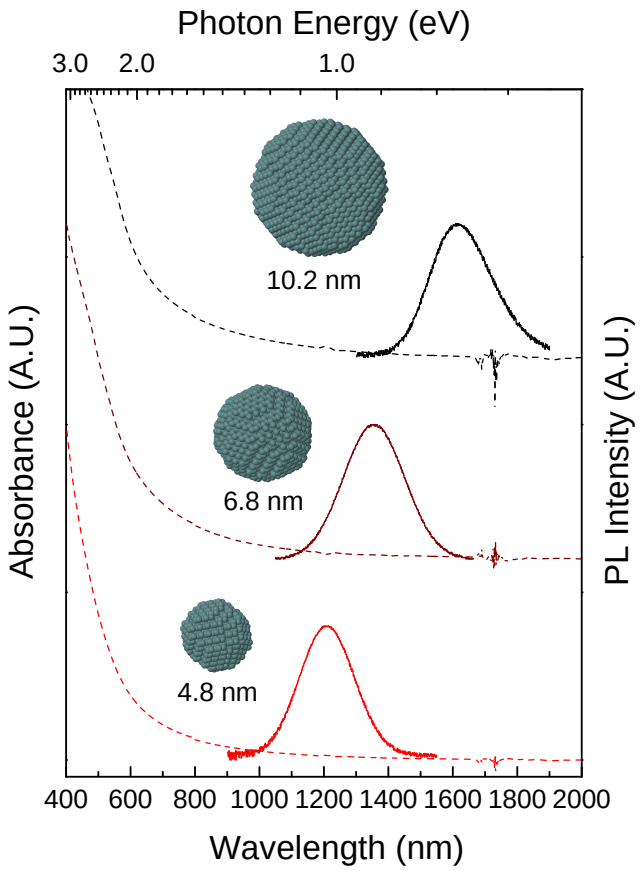

Figure 6.5: **Optical properties of surface-passivated Ge NCs.** Absorption (dashed) and PL (solid) spectra are plotted as a function of wavelength and photon energy. At 10.2 nm, the PL emission is blue-shifted from the bulk Ge value of 0.67 eV to 0.77 eV. Bandgap emission due quantum confinement is confirmed, as 6.8 nm and 4.8 nm Ge NCs are shifted to higher energies of 0.93 eV and 1.03 eV, respectively. Quantum confinement effects are correspondingly observed in absorption spectra. The absorption feature near 1730 nm arises due to subtraction of a strong solvent peak. PL peak location was independent of excitation energy. Spectra are normalized and offset for clarity.

is consistent with previous measurements on ligand-free colloidal solutions of Ge NCs.[67].

6.4 Literature comparison

Perhaps the most notable achievements of this work are the Gaussian shape and narrow width of PL emission. A narrow emission line width will be important for Ge NC optoelectronic device integration. This is especially the case for telecommunication applications. Figure 6.6 provides perspective by plotting our work along with previous reports of bandgap emission. Each point represents the peak emission energy. The error bars correspond to the full width at half maximum (FWHM) of the emission curve.

Emission curves observed in this work are Gaussian, which suggests the shape of the peak is solely due to the Gaussian size distribution of plasma-synthesized Ge NCs, which typically 10% to 15% in this size range[53]. The FWHMs of the emission curves are at least a factor of 2 narrower than previous reports and are comparable to the high PL quantum yield (PLQY) emission observed in Si NC synthesized using a similar technique[14]. Indeed, surface passivation of Si NCs, has been shown to play a pivotal role in achieving efficient PL as well[14,58]. Experiments are currently underway to evaluate the PLQY of Ge NCs in this work.

It is also worth noting that we are reporting the largest diameter Ge NCs to exhibit bandgap emission. Though Ruddy *et al.* were able to synthesize Ge NCs ranging in size from 2.3 nm to 11.3 nm in diameter, negligible PL was observed for the larger 6.6 nm and 11.3 nm samples[10]. In addition to the narrow Gaussian emission, we believe this is a testament to the high-quality crystal provided by nonthermal plasma synthesis as well as an effective surface passivation scheme.

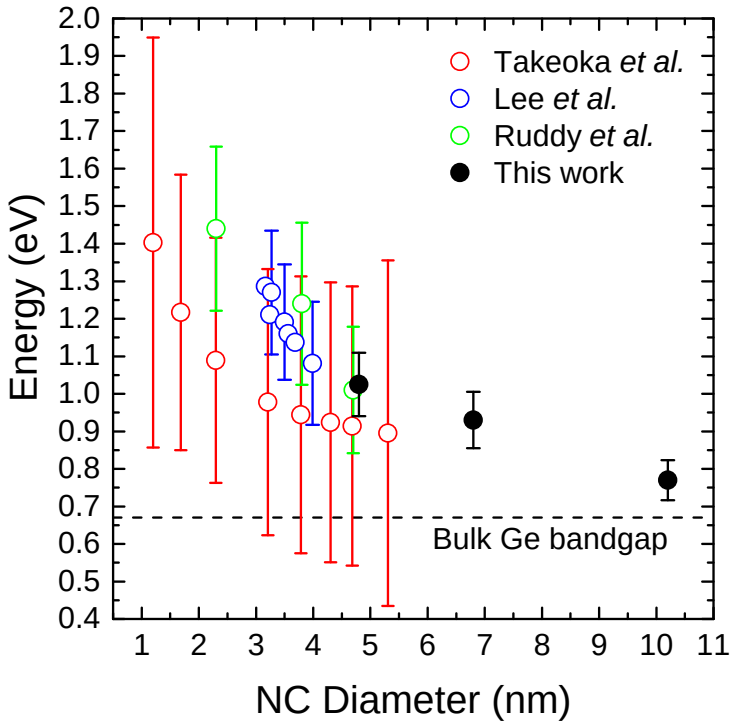

Figure 6.6: **Literature comparison.** Optical bandgap energy as a function of Ge NC diameter determined by PL emission peaks. Bandgap peak emission energies determined in this work are plotted with Ge NCs synthesized from colloidal methods[9,10] and Ge NCs embedded in SiO_2[11]. Error bars represent the FWHM determined from a Gaussian fit to the PL spectra. For comparison, PL spectra from Takeoka *et al.*[11], Lee *et al.*[9], and Ruddy *et al.*[10] were digitized and also fit with a Gaussian curve to determine FWHMs.

6.5 Conclusion

In conclusion, we demonstrate tunable room temperature bandgap emission from quantum-confined Ge NCs. By employing a simple Grignard reaction scheme to the native Ge-Cl surface groups, Cl is exchanged for alkyl termination to achieve an electronic structure that is favorable for radiative recombination. PL emission curves are Gaussian and feature FWHMs that are a dramatic improvement over previous reports, which signifies an important step in the development of

free-standing Ge NCs for bio-imaging and optoelectronic device applications.

6.6 Experimental methods

Ge NC plasma synthesis. Ge NCs are synthesized in a nonthermal plasma reactor by decomposing $GeCl_4$ vapor in the presence H_2, which serves as a reducing environment. Vapor is drawn from a room temperature ampule filled with $GeCl_4$. 10.2 nm NCs are synthesized at 930 Pa by flowing 1.5 standard cubic centimeter (sccm) of $GeCl_4$, 30 sccm of H_2, and 40 sccm of Ar and applying 50 W of radio frequency power through a custom matching network to a set of copper ring electrodes separated by 1 cm and secured to a 2.54 cm outer diameter glass tube. 6.8 nm NCs are synthesized at 269 Pa by flowing 1 sccm of $GeCl_4$, 20 sccm of H_2, and 30 sccm of Ar and applying 40 W of radio frequency power. 4.8 nm NCs are synthesized at 261 Pa by flowing 1 sccm of $GeCl_4$, 20 sccm of H_2, and 30 sccm of Ar and applying 40 W of radio frequency power. A more detailed description of the synthetic method can be found in Gresback *et al.*[55].

Surface passivation chemistry. 10.2 nm and 6.8 nm Ge NCs were collected downstream of the synthesis plasma using gas-phase inertial impaction onto a glass substrate[182]. 4.8 nm Ge NCs were collected *via* diffusion onto a stainless steal mesh. Ge NCs deposited onto a glass substrate or stainless steel mesh are moved air-free from the reactor to a N_2-purged glovebox where they are transferred into a glass test tube and sealed with a rubber septum. Ge NC surface passivation chemistry was performed air-free using a Schlenk line. The Grignard reagent was diluted to 0.11 M in diethyl ether and added to the glass vial *via* cannula transfer. Even before heating, reaction of the Ge-Cl surface groups with the Grignard reagent is immediately observable as bubbling due the release of HCl gas. The mixture is sonicated for few minutes to form a dense slurry. The slurry is transfered *via* cannula to a round-bottom flask in a

temperature-controlled sand bath. Excess diethyl ether is added to bring the total volume of the reaction mixture to roughly 25 ml. The mixture is refluxed at 80 °C under continuous N_2 purge for 2 hours yielding an optically-transparent solution. Surface-passivated Ge NCs are dried under N_2 purge and transferred back into N_2-purged glovebox for further characterzation and sample preparation.

Fourier transform infrared spectroscopy. Cl-terminated Ge NC samples were obtained by depositing a Ge NC film on to a gold-coated silicon wafer substrate *via* gas-phase impaction downstream of the synthesis plasma. Spectra were taken using the diffuse reflectance attachment for a Bruker Alpha FTIR spectrometer inside a N_2-atmosphere glovebox. Dodecyl-terminated Ge NCs and the $CH_3(CH_2)_{10}CH_2MgBr$ precursor samples were drop-cast onto a diamond attenuated total reflectance crystal attached to the same FTIR spectrometer. Spectra were typically collected by averaging 24 scans at 2 cm^{-1} resolution.

PL and UV-Vis spectroscopy. Samples were extracted from the reaction flask to a glass cuvette sealed with a screw-cap and vacuum grease and diluted in diethyl ether to a concentration of approximately 0.25 mg/ml. PL spectra are obtained by exciting the sample with 900 nm light mechanically chopped from a Xenon lamp light source. A cooled InGaAs photodiode (800-2100 nm) was used for PL detection. The PL signal was amplified using a lock-in amplifier referenced to a chopper driver, and spectra were collected by scanning the wavelength range using a monochromator and averaging 12 to 15 accumulations. Background and scatter were accounted for by subtracting a spectrum obtained under identical conditions but with only solvent present in the cuvette. Similarly, UV-visible absorption spectra are obtained using Cary 5E UV-Vis spectrophotometer by scanning the wavelength range using a monochromator.

X-ray diffraction. X-ray diffraction (XRD) was performed on Ge NC impacted

onto a glass substrate using a Bruker-AXS microdiffractometer with a 2.2 kW sealed Cu X-ray source. The Ge NC diameter was calculated from the Scherrer equation using Jade 8.0 software.

6.7 Future work

Germanium has many advantages over silicon for optoelectronics. The band gap can be tuned from telecommunications wavelengths out to the visible. Due to a significantly larger exciton radius, even blue emission can presumably be achieved without going to to the extremely small sizes (<3 nm), which is the unfortunate case for Si. The observation of band edge emission indicates the Ge NCs explored here are likely of the best electronic crystal quality to date. As such, quantum yield measurements should be a priority to evaluate the efficiency of the observed photoluminescence. Just as recommended with the Si-Cl surface chemistry in the previous section, a systematic study on the effects of ligand termination on optical emission should be undertaken. Again, the Ge-C-R, Ge-S-R, and Ge-N-R functionalities are now readily accessible. More advanced optical measurements are also in order. For instance, Si has be shown to be extremely efficient at generating multiple excitons[183], but there are no results on Ge NCs. Previous attempts have failed due to the high trap density, but this should no longer be an issue.

Another obvious avenue of research is integration of Ge NCs as the absorber material of a photovoltaic device. The transistor mobilities of Ge NC thin films[64] have been shown to be competitive with the best performing NC-based solar cells[5]. Moreover, the absorption coefficient of Ge is considerably higher than Si. This allows for a thinner absorber layer and more efficient charge extraction. A simple bilayer TiO_2 heterojunction device should have favorable band alignment, and the fabrication of such a device is well known in the literature[36]. A similar device based on Si NCs will alway be more difficult and limited by the long diffusion lengths mandated by the thick films needed for an optically opaque device. One

concern is the scarcity, and thus cost, of Ge, which makes Si more appealing. However, the now-prevalent use of CdSe NCs in a variety of commercial devices perhaps trumps this downfall.

References

1. X. D. Pi, R. W. Liptak, J. D. Nowak, N. P. Wells, C. B. Carter, S. A. Campbell, and U. Kortshagen. Air-stable full-visible-spectrum emission from silicon nanocrystals synthesized by an all-gas-phase plasma approach. *Nanotechnology*, 19(24):245603, 2008.

2. M. C. Beard, J. M. Luther, O. E. Semonin, and A. J. Nozik. Third generation photovoltaics based on multiple exciton generation in quantum confined semiconductors. *Accounts of Chemical Research*, 46(6):1252–1260, 2012.

3. W. Tisdale, K. Williams, B. Timp, D. J. Norris, E. Aydil, and X. Zhu. Hot-electron transfer from semiconductor nanocrystals. *Science*, 328(5985):1543–1547, 2010.

4. A. Jocelyn. History of the processes of manufacture, 1864. used under CC BY.

5. A. H. Ip, S. M. Thon, S. Hoogland, O. Voznyy, D. Zhitomirsky, R. Debnath, L. Levina, L. R. Rollny, G. H. Carey, A. Fischer, and E. H. Sargent. Hybrid passivated colloidal quantum dot solids. *Nature Nanotechnology*, 7(9):577–582, 2012.

6. M. Kovalenko, M. Scheele, and D. Talapin. Colloidal nanocrystals with molecular metal chalcogenide surface ligands. *Science*, 324(5933):1417–1420, 2009.

7. O. E. Semonin, J. M. Luther, S. Choi, H. Y. Chen, J. Gao, A. J. Nozik, and M. C. Beard. Peak external photocurrent quantum efficiency exceeding 100% via meg in a quantum dot solar cell. *Science*, 334(6062):1530–1533, 2011.

8. J.-S. Lee, M. V. Kovalenko, J. Huang, D. S. Chung, and D. V. Talapin. Band-like transport, high electron mobility and high photoconductivity in all-inorganic nanocrystal arrays. *Nature Nanotechnology*, 6(6):348–352, 2011.

9. D. C. Lee, J. M. Pietryga, I. Robel, D. J. Werder, R. D. Schaller, and V. I. Klimov. Colloidal synthesis of infrared-emitting germanium nanocrystals. *Journal of Organic Chemistry*, 131(10):3436–3437, 2009.

10. D. A. Ruddy, J. C. Johnson, E. R. Smith, and N. R. Neale. Size and bandgap control in the solution-phase synthesis of near-infrared-emitting germanium nanocrystals. *ACS Nano*, 4(12):7459–7466, 2010.

11. S. Takeoka, M. Fujii, S. Hayashi, and K. Yamamoto. Size-dependent near-infrared photoluminescence from Ge nanocrystals embedded in SiO_2 matrices. *Physical Review B*, 58(12):7921, 1998.

12. A. Smith. Smartphone ownership–2013 update. *Pew Research Center: Washington DC*, 2013.

13. L. E. Brus. Electron–electron and electron-hole interactions in small semiconductor crystallites: The size dependence of the lowest excited electronic state. *The Journal of Chemical Physics*, 80(9):4403–4409, 1984.

14. D. Jurbergs, E. Rogojina, L. Mangolini, and U. Kortshagen. Silicon nanocrystals with ensemble quantum yields exceeding 60%. *Applied Physics Letters*, 88(23):233116, 2006.

15. M. S. Hybertsen. Absorption and emission of light in nanoscale silicon structures. *Physical Review Letters*, 72(10):1514, 1994.

16. C. Delerue, G. Allan, C. Reynaud, O. Guillois, G. Ledoux, and F. Huisken. Multiexponential photoluminescence decay in indirect-gap semiconductor nanocrystals. *Physical Review B*, 73(23):235318, 2006.

17. W. Shockley and H. J. Queisser. Detailed balance limit of efficiency of p-n junction solar cells. *Journal of Applied Physics*, 32(3):510–519, 2004.

18. A. J. Nozik. Spectroscopy and hot electron relaxation dynamics in semiconductor quantum wells and quantum dots. *Annual Review of Physical Chemistry*, 52(1):193–231, 2001.

19. R. D. Schaller and V. I. Klimov. High efficiency carrier multiplication in pbse nanocrystals: implications for solar energy conversion. *Physical Review Letters*, 92(18):186601, 2004.

20. R. T. Ross and A. J. Nozik. Efficiency of hot-carrier solar energy converters. *Journal of Applied Physics*, 53(5):3813–3818, 1982.

21. M. Beard. Multiple exciton generation in semiconductor quantum dots. *The Journal of Physical Chemistry Letters*, 2(11):1282–1288, 2011.

22. D. Timmerman, J. Valenta, K. Dohnalová, W. D. A. M. de Boer, and T. Gregorkiewicz. Step-like enhancement of luminescence quantum yield of silicon nanocrystals. *Nature Nanotechnology*, 6(11):710–713, 2011.

23. D. Timmerman, I. Izeddin, P. Stallinga, I. Yassievich, and T. Gregorkiewicz. Space-separated quantum cutting with silicon nanocrystals for photovoltaic applications. *Nature Photonics*, 2(2):105–109, 2008.

24. J. B. Sambur, T. Novet, and B. A. Parkinson. Multiple exciton collection in a sensitized photovoltaic system. *Science*, 330(6000):63–66, 2010.

25. E. D. Williams, R. U. Ayres, and M. Heller. The 1.7 kilogram microchip: Energy and material use in the production of semiconductor devices. *Environmental Science & Technology*, 36(24):5504–5510, 2002.

26. C. Murray, D. Norris, and M. Bawendi. Synthesis and characterization of nearly monodisperse CdE (E = sulfur, selenium, tellurium) semiconductor nanocrystallites. *Journal of the American Chemical Society*, 115(19):8706–8715, 1993.

27. R. Marom, S. F. Amalraj, N. Leifer, D. Jacob, and D. Aurbach. A review of advanced and practical lithium battery materials. *Journal of Materials Chemistry*, 21(27):9938–9954, 2011.

28. J. M. Pietryga, R. D. Schaller, D. Werder, M. H. Stewart, V. I. Klimov, and J. A. Hollingsworth. Pushing the band gap envelope: mid-infrared emitting colloidal PbSe quantum dots. *Journal of the American Chemical Society*, 126(38):11752–11753, 2004.

29. D. K. Kim, A. T. Fafarman, B. T. Diroll, S. H. Chan, T. R. Gordon, C. B. Murray, and C. R. Kagan. Solution-based stoichiometric control over charge transport in nanocrystalline CdSe devices. *ACS Nano*, 7(10):8760–8770, 2013.

30. J. M. Luther and J. M. Pietryga. Stoichiometry control in quantum dots: A viable analog to impurity doping of bulk materials. *ACS Nano*, 7(3):1845–1849, 2013.

31. P. Reiss, M. Protiere, and L. Li. Core/shell semiconductor nanocrystals. *Small*, 5(2):154–168, 2009.

32. Research and markets: Global quantum dots market in solid state lighting, solar cells and display applications market opportunities forecasts 2013 - 2018, 2014. http://www.cnbc.com/id/101576285.

33. F. Meinardi, A. Colombo, K. A. Velizhanin, R. Simonutti, M. Lorenzon, L. Beverina, R. Viswanatha, V. I. Klimov, and S. Brovelli. Large-area luminescent solar concentrators based on "stokes-shift-engineered" nanocrystals in a mass-polymerized pmma matrix. *Nature Photonics*, 2014.

34. Y. Yin and A. P. Alivisatos. Colloidal nanocrystal synthesis and the organic–inorganic interface. *Nature*, 437(7059):664–670, 2005.

35. M. Law, J. Luther, Q. Song, B. Hughes, C. Perkins, and A. Nozik. Structural, optical, and electrical properties of PbSe nanocrystal solids treated thermally or with simple amines. *Journal of the American Chemical Society*, 130(18):5974–5985, 2008.

36. J. M. Luther, J. Gao, M. T. Lloyd, O. E. Semonin, M. C. Beard, and A. J. Nozik. Stability assessment on a 3% bilayer PbS/ZnO quantum dot heterojunction solar cell. *Advanced Materials*, 22(33):3704–3707, 2010.

37. J. Tang, K. Kemp, S. Hoogland, K. Jeong, H. Liu, L. Levina, M. Furukawa, X. Wang, R. Debnath, D. Cha, et al. Colloidal-quantum-dot photovoltaics using atomic-ligand passivation. *Nature Materials*, 10(10):765–771, 2011.

38. D. Zhitomirsky, O. Voznyy, L. Levina, S. Hoogland, K. W. Kemp, A. H. Ip, S. M. Thon, and E. H. Sargent. Engineering colloidal quantum dot solids within and beyond the mobility-invariant regime. *Nature Communications*, 5:1–7, 2014.

39. M. V. Kovalenko, M. I. Bodnarchuk, J. Zaumseil, J.-S. Lee, and D. V. Talapin. Expanding the chemical versatility of colloidal nanocrystals capped with molecular metal chalcogenide ligands. *Journal of the American Chemical Society*, 132(29):10085–10092, 2010.

40. A. Nag, M. Kovalenko, J. Lee, W. Liu, B. Spokoyny, and D. Talapin. Metal-free inorganic ligands for colloidal nanocrystals: S_2^-, HS^-, Se^{2-}, HSe^-, Te^{2-}, HTe^-, TeS_3^{2-}, OH^-, and NH_2^- as surface ligands. *Journal of the American Chemical Society*, 133(27):10612–10620, 2011.

41. A. Nag, D. S. Chung, D. S. Dolzhnikov, N. M. Dimitrijevic, S. Chattopadhyay, T. Shibata, and D. V. Talapin. Effect of metal ions on photoluminescence, charge transport, magnetic and catalytic properties of all-inorganic

colloidal nanocrystals and nanocrystal solids. *Journal of the American Chemical Society*, 134(33):13604–13615, 2012.

42. A. T. Fafarman, W.-k. Koh, B. T. Diroll, D. K. Kim, D.-K. Ko, S. J. Oh, X. Ye, V. Doan-Nguyen, M. R. Crump, D. C. Reifsnyder, C. B. Murray, and C. R. Kagan. Thiocyanate-capped nanocrystal colloids: Vibrational reporter of surface chemistry and solution-based route to enhanced coupling in nanocrystal solids. *Journal of the American Chemical Society*, 133(39):15753–15761, 2011.

43. W.-k. Koh, S. R. Saudari, A. T. Fafarman, C. R. Kagan, and C. B. Murray. Thiocyanate-capped pbs nanocubes: Ambipolar transport enables quantum dot based circuits on a flexible substrate. *Nano Letters*, 11(11):4764–4767, 2011.

44. A. A. Cordones, M. Scheele, A. P. Alivisatos, and S. R. Leone. Probing the interaction of single nanocrystals with inorganic capping ligands: Time-resolved fluorescence from CdSe–CdS quantum dots capped with chalcogenidometalates. *Journal of the American Chemical Society*, 134(44):18366–18373, 2012.

45. J. R. Heath. Covalency in semiconductor quantum dots. *Chemical Society Review*, 27(1):65–71, 1998.

46. K. A. Pettigrew, Q. Liu, P. P. Power, and S. M. Kauzlarich. Solution synthesis of alkyl-and alkyl/alkoxy-capped silicon nanoparticles via oxidation of Mg_2Si. *Chemistry of Materials*, 15(21):4005–4011, 2003.

47. G. Ledoux, J. Gong, F. Huisken, O. Guillois, and C. Reynaud. Photoluminescence of size-separated silicon nanocrystals: Confirmation of quantum confinement. *Applied Physics Letters*, 80(25):4834–4836, 2002.

48. K. Littau, P. Szajowski, A. Muller, A. Kortan, and L. Brus. A luminescent silicon nanocrystal colloid via a high-temperature aerosol reaction. *The Journal of Physical Chemistry*, 97(6):1224–1230, 1993.

49. F. Huisken, G. Ledoux, O. Guillois, and C. Reynaud. Light-emitting silicon nanocrystals from laser pyrolysis. *Advanced Materials*, 14(24):1861–1865, 2002.

50. R. J. Walters, J. Kalkman, A. Polman, H. A. Atwater, and M. J. A. De Dood. Photoluminescence quantum efficiency of dense silicon nanocrystal ensembles in SiO_2. *Physical Review B*, 73(13):132302, 2006.

51. M. Lopez, B. Garrido, P. Pellegrino, J. R. Morante, C. Bonafos, M. Carrada, A. Claverie, et al. Elucidation of the surface passivation role on the photoluminescence emission yield of silicon nanocrystals embedded in SiO_2. *Applied Physics Letters*, 80(9):1637–1639, 2002.

52. M. Zacharias, J. Heitmann, R. Scholz, U. Kahler, M. Schmidt, and J. Bläsing. Size-controlled highly luminescent silicon nanocrystals: A SiO/SiO_2 superlattice approach. *Applied Physics Letters*, 80(4):661–663, 2002.

53. U. Kortshagen. Nonthermal plasma synthesis of semiconductor nanocrystals. *Journal of Physics D: Applied Physics*, 42(11):113001, 2009.

54. L. Mangolini, E. Thimsen, and U. Kortshagen. High-yield plasma synthesis of luminescent silicon nanocrystals. *Nano Letters*, 5(4):655–659, 2005.

55. R. Gresback, Z. Holman, and U. Kortshagen. Nonthermal plasma synthesis of size-controlled, monodisperse, freestanding germanium nanocrystals. *Applied Physics Letters*, 91(9):093119–093119–3, 2007.

56. X. D. Pi and U. Kortshagen. Nonthermal plasma synthesized freestanding silicon–germanium alloy nanocrystals. *Nanotechnology*, 20(29):295602, 2009.

57. R. Anthony and U. Kortshagen. Photoluminescence quantum yields of amorphous and crystalline silicon nanoparticles. *Physical Review B*, 80(11):115407, 2009.

58. R. J. Anthony, D. J. Rowe, M. Stein, J. Yang, and U. Kortshagen. Routes to achieving high quantum yield luminescence from gas-phase-produced silicon nanocrystals. *Advanced Functional Materials*, 21(21):4042–4046, 2011.

59. K.-Y. Cheng, R. Anthony, U. R. Kortshagen, and R. J. Holmes. Hybrid silicon nanocrystal-organic light-emitting devices for infrared electroluminescence. *Nano Letters*, 10(4):1154–1157, 2010.

60. K. Y. Cheng, R. Anthony, U. R. Kortshagen, and R. J. Holmes. High-efficiency silicon nanocrystal light-emitting devices. *Nano Letters*, 11(5):1952–1956, 2011.

61. R. J. Anthony, K.-Y. Cheng, Z. C. Holman, R. J. Holmes, and U. R. Kortshagen. An all-gas-phase approach for the fabrication of silicon nanocrystal light-emitting devices. *Nano Letters*, 12(6):2822–2825, 2012.

62. C. Liu, Z. Holman, and U. Kortshagen. Hybrid solar cells from P3HT and silicon nanocrystals. *Nano Letters*, 9(1):449–452, 2008.

63. N. Rastgar, D. J. Rowe, R. J. Anthony, B. A. Merritt, U. R. Kortshagen, and E. S. Aydil. Effects of water adsorption and surface oxidation on the electrical conductivity of silicon nanocrystal films. *The Journal of Physical Chemistry C*, 117(8):4211–4218, 2013.

64. Z. C. Holman, C.-Y. Liu, and U. R. Kortshagen. Germanium and silicon nanocrystal thin-film field-effect transistors from solution. *Nano Letters*, 10(7):2661–2666, 2010.

65. Z. Holman and U. R. Kortshagen. Solution-processed germanium nanocrystal thin films as materials for low-cost optical and electronic devices. *Langmuir*, 25(19):11883–11889, 2009.

66. Z. C. Holman and U. R. Kortshagen. Quantum confinement in germanium nanocrystal thin films. *Physica Status Solidi (RRL) - Rapid Research Letters*, 5(3):110–112, 2011.

67. Z. Holman and U. R. Kortshagen. Absolute absorption cross sections of ligand-free colloidal germanium nanocrystals. *Applied Physics Letters*, 100(13):133108–133108, 2012.

68. L. M. Wheeler, N. R. Neale, T. Chen, and U. R. Kortshagen. Hypervalent surface interactions for colloidal stability and doping of silicon nanocrystals. *Nature Communications*, 4, 2013.

69. L. M. Wheeler, L. M. Levij, and U. R. Kortshagen. Tunable band gap emission and surface passivation of germanium nanocrystals synthesized in the gas phase. *The Journal of Physical Chemistry Letters*, 4(20):3392–3396, 2013.

70. M. Filler and S. Bent. The surface as molecular reagent: organic chemistry at the semiconductor interface. *Progress in Surface Science*, 73:1–56, 2003.

71. Y. Yin and A. Alivisatos. Colloidal nanocrystal synthesis and the organic–inorganic interface. *Nature*, 437(7059):664–670, 2004.

72. W. B. Jensen. *The Lewis acid-base concepts*. an overview. John Wiley & Sons, 1980.

73. N. C. Anderson, M. P. Hendricks, J. J. Choi, and J. S. Owen. Ligand exchange and the stoichiometry of metal chalcogenide nanocrystals: Spectroscopic observation of facile metal-carboxylate displacement and binding. *Journal of the American Chemical Society*, 135(49):18536–18548, 2013.

74. S. Pokrant and K. B. Whaley. Tight-binding studies of surface effects on electronic structure of cdse nanocrystals: the role of organic ligands, surface

reconstruction, and inorganic capping shells. *The European Physical Journal D*, 6(2):255–267, 1999.

75. M. A. Caldwell, A. E. Albers, S. C. Levy, T. E. Pick, B. E. Cohen, B. A. Helms, and D. J. Milliron. Driving oxygen coordinated ligand exchange at nanocrystal surfaces using trialkylsilylated chalcogenides. *Chemical Communications*, 47(1):556–558, 2010.

76. T. Zhang, J. Ge, Y. Hu, and Y. Yin. A general approach for transferring hydrophobic nanocrystals into water. *Nano letters*, 7(10):3203–3207, 2007.

77. J. D. Holmes, K. J. Ziegler, R. C. Doty, L. E. Pell, K. P. Johnston, and B. A. Korgel. Highly luminescent silicon nanocrystals with discrete optical transitions. *Journal of the American Chemical Society*, 123(16):3743–3748, 2001.

78. A. Puzder, A. Williamson, J. C. Grossman, and G. Galli. Surface chemistry of silicon nanoclusters. *Physical Review Letters*, 88(9):097401, 2002.

79. S. E. Denmark and G. L. Beutner. Lewis base catalysis in organic synthesis. *Angewandte Chemie International Edition*, 47(9):1560–1638, 2008.

80. C. Sun and J. C. Berg. A review of the different techniques for solid surface acid-base characterization. *Advances in Colloid and Interface Science*, 105(1–3):151 –175, 2003.

81. S. Pawlenko. *Organosilicon chemistry*. de Gruyter, 1986.

82. P. W. Loscutoff and S. F. Bent. Reactivity of the germanium surface: Chemical passivation and functionalization. *Annual Review of Physical Chemistry*, 57:467–495, 2006.

83. Z. C. Holman and U. R. Kortshagen. Nanocrystal inks without ligands: Stable colloids of bare germanium nanocrystals. *Nano Letters*, 11(5):2133–2136, 2011.

84. F. Erogbogbo, T. Liu, N. Ramadurai, P. Tuccarione, L. Lai, M. Swihart, and P. Prasad. Creating ligand-free silicon germanium alloy nanocrystal inks. *ACS Nano*, 5(10):7950–7959, 2011.

85. L. Mangolini and U. Kortshagen. Selective nanoparticle heating: Another form of nonequilibrium in dusty plasmas. *Physical Review E*, 79(2):026405, 2009.

86. N. J. Kramer, R. J. Anthony, M. Mamunuru, E. S. Aydil, and U. R. Kortshagen. Plasma-induced crystallization of silicon nanoparticles. *Journal of Physics D: Applied Physics*, 47(7):075202, 2014.

87. R. N. Carlile, S. Geha, J. F. O'Hanlon, and J. C. Stewart. Electrostatic trapping of contamination particles in a process plasma environment. *Applied Physics Letters*, 59(10):1167–1169, 1991.

88. U. Kortshagen and U. Bhandarkar. Modeling of particulate coagulation in low pressure plasmas. *Physical Review E*, 60(1):887, 1999.

89. S. J. Choi and M. J. Kushner. The role of negative ions in the formation of particles in low-pressure plasmas. *Journal of Applied Physics*, 74(2):853–861, 1993.

90. R. Gresback, T. Nozaki, and K. Okazaki. Synthesis and oxidation of luminescent silicon nanocrystals from silicon tetrachloride by very high frequency nonthermal plasma. *Nanotechnology*, 22(30):305605, 2011.

91. M. Fujii, Y. Kanzawa, S. Hayashi, and K. Yamamoto. Raman scattering from acoustic phonons confined in si nanocrystals. *Physical Review-Section B-Condensed Matter*, 54(12):R8373, 1996.

92. C.-S. Yang, R. A. Bley, S. M. Kauzlarich, H. W. Lee, and G. R. Delgado. Synthesis of alkyl-terminated silicon nanoclusters by a solution route. *Journal of the American Chemical Society*, 121(22):5191–5195, 1999.

93. D. Shamiryan, M. Baklanov, M. Claes, W. Boullart, and V. Paraschiv. Selective removal of high-k gate dielectrics. *Chemical Engineering Communications*, 196(12):1475–1535, 2009.

94. R. Liptak, U. Kortshagen, and S. Campbell. Surface chemistry dependence of native oxidation formation on silicon nanocrystals. *Journal of Applied Physics*, 106(6):064313, 2009.

95. R. W. Liptak, B. Devetter, J. H. Thomas, III, U. Kortshagen, and S. A. Campbell. Sf6 plasma etching of silicon nanocrystals. *Nanotechnology*, 20(3):035603, 2009.

96. R. Pereira, D. Rowe, R. Anthony, and U. Kortshagen. Oxidation of free-standing silicon nanocrystals probed with electron spin resonance of interfacial dangling bonds. *Physical Review B*, 83(15), 2011.

97. T. Matsuura, H. Uetake, T. Ohmi, J. Murota, K. Fukuda, N. Mikoshiba, T. Kawashima, and Y. Yamashita. Directional etching of Si with perfect selectivity to SiO_2 using an ultraclean electron cyclotron resonance plasma. *Applied Physics Letters*, 56(14):1339–1341, 1990.

98. S. Rivillon, Y. J. Chabal, L. J. Webb, D. J. Michalak, N. S. Lewis, M. D. Halls, and K. Raghavachari. Chlorination of hydrogen-terminated silicon (111) surfaces. *Journal of Vacuum Science & Technology A*, 23(4):1100–1106, 2005.

99. R. Gresback, T. Nozaki, and K. Okazaki. Synthesis and oxidation of luminescent silicon nanocrystals from silicon tetrachloride by very high frequency nonthermal plasma. *Nanotechnology*, 22(30):305605, 2011.

100. O. Yasar-Inceoglu, T. Lopez, E. Farshihagro, and L. Mangolini. Silicon nanocrystal production through non-thermal plasma synthesis: a comparative study between silicon tetrachloride and silane precursors. *Nanotechnology*, 23(25):255604, 2012.

101. H. Hillhouse and M. Beard. Solar cells from colloidal nanocrystals: Fundamentals, materials, devices, and economics. *Current Opinion in Colloid & Interface Science*, 14(4):245–259, 2009.

102. V. Wood and V. Bulović. Colloidal quantum dot light-emitting devices. *Nano Reviews*, 1, 2010.

103. G. Konstantatos and E. Sargent. Nanostructured materials for photon detection. *Nature Nanotechnology*, 5(6):391–400, 2010.

104. H. Kamiya and M. Iijima. Surface modification and characterization for dispersion stability of inorganic nanometer-scaled particles in liquid media. *Science and Technology of Advanced Materials*, 11(4):044304, 2010.

105. C. Murray, C. Kagan, and M. Bawendi. Self-organization of cdse nanocrystallites into three-dimensional quantum dot superlattices. *Science*, 270(5240):1335–1338, 1995.

106. D. Talapin and C. Murray. PbSe nanocrystal solids for n-and p-channel thin film field-effect transistors. *Science*, 310(5745):86–89, 2005.

107. D. J. Norris, A. L. Efros, and S. C. Erwin. Doped nanocrystals. *Science*, 319(5871):1776–1779, 2008.

108. V. Gutmann. *The donor-acceptor approach to molecular interactions*, volume 228. Plenum Press New York, 1978.

109. R. Corriu. Hypervalent species fo silicon: structure and reactivity. *Journal of Organometallic Chemistry*, 400(1–2):81–106, 1990.

110. H. Sugimoto, M. Fujii, K. Imakita, S. Hayashi, and K. Akamatsu. All-inorganic near-infrared luminescent colloidal silicon nanocrystals–high dispersibility in polar liquid by phosphorus and boron co-doping. *The Journal of Physical Chemistry C*, 116(33):17969–17974, 2012.

111. J.-L. Abboud and R. Notari. Critical compilation of scales of solvent parameters. Part I. Pure, non-hydrogen bond donor solvents. *Pure and Applied Chemistry*, 71(4):645–718, 1999.

112. I. Landolt-Börnstein. 17: Static dielectric constants of pure liquids and binary liquid mixtures. *SpringerMaterials-The Landolt-Börnstein Database*, 2008.

113. C. Laurence and J.-F. Gal. *Lewis Basicity and Affinity Scales*. Data and Measurement. John Wiley & Sons, 2009.

114. R. Nyquist. Infrared studies of ketones: Parameters affecting the induced carbonyl stretching vibration by solute/solvent interaction. *Applied Spectroscopy*, 44(3):433–438, 1990.

115. W. Fawcett, G. Liu, and T. Kessler. Solvent-induced frequency shifts in the infrared spectrum of acetonitrile in organic solvents. *The Journal of Physical Chemistry*, 97(37):9293–9298, 1993.

116. P. Hiemenz and R. Rajagopalan. *Principles of colloid and surface chemistry, revised and expanded*, volume 14. CRC, 1997.

117. K. Matsubara, R. Kaneuchi, and N. Maekita. ^{13}C NMR estimation of preferential solvation of lithium ions in non-aqueous mixed solvents. *Journal of the Chemical Society, Faraday Transactions*, 94(24):3601–3605, 1998.

118. Since this data was unavailable, this value was calculated by a linear interpolation between hexanenitrile and octanenitrile.

119. T. Pons, H. Uyeda, I. Medintz, and H. Mattoussi. Hydrodynamic dimensions, electrophoretic mobility, and stability of hydrophilic quantum dots. *The Journal of Physical Chemistry B*, 110(41):20308–20316, 2006.

120. I. D. Morrison. Criterion for electrostatic stability of dispersions at low ionic strength. *Langmuir*, 7(9):1920–1922, 1991.

121. Y. Liang, N. Hilal, P. Langston, and V. Starov. Interaction forces between colloidal particles in liquid: Theory and experiment. *Advances in Colloid and Interface Science*, 134:151–166, 2007.

122. J. N. Israelachvili. *Intermolecular and surface forces: revised third edition*. Academic Press, 2011.

123. J. Ristein. Surface transfer doping of semiconductors. *Science*, 313(5790):1057–1058, 2006.

124. Á. Miranda, X. Cartoixà, E. Canadell, and R. Rurali. NH_3 molecular doping of silicon nanowires grown along the [112], [110], [001], and [111] orientations. *Nanoscale Research Letters*, 7(1):308, 2012.

125. E. Garrone, F. Geobaldo, P. Rivolo, G. Amato, L. Boarino, M. Chiesa, E. Giamello, R. Gobetto, P. Ugliengo, and A. Viale. A nanostructured porous silicon near insulator becomes either a p- or an n-type semiconductor upon gas adsorption. *Advanced Materials*, 17(5):528–531, 2005.

126. G. D. Yuan, Y. B. Zhou, C. S. Guo, W. J. Zhang, Y. B. Tang, Y. Q. Li, Z. H. Chen, Z. B. He, X. J. Zhang, and P. F. Wang. Tunable electrical properties of silicon nanowires via surface-ambient chemistry. *ACS Nano*, 4(6):3045–3052, 2010.

127. A. Miranda-Durán, X. Cartoixà, M. Cruz Irisson, and R. Rurali. Molecular doping and subsurface dopant reactivation in si nanowires. *Nano Letters*, 2010.

128. D. J. Rowe, J. S. Jeong, K. A. Mkhoyan, and U. Kortshagan. Phosphorus-doped silicon nanocrystals exhibiting mid-infrared localized surface plasmon resonance. *Nano Letters*, 2013.

129. A. Martínez, J. C. Alonso, L. E. Sansores, and R. Salcedo. Electronic structure of silicon nanocrystals passivated with nitrogen and chlorine. *The Journal of Physical Chemistry C*, 114(29):12427–12431, 2010.

130. R. J. P. Corriu, G. Dabosi, and M. Martineau. The nature of the interaction of nucleophiles such as $HMPT$, $DMSO$, DMF and Ph_3PO with triorganohalo-silanes, -germanes, and -stannanes and organophosphorus compounds. Mechanism of nucleophile induced racemization and substitution at metal. *Journal of Organometallic Chemistry*, 186(1):25–37, 1980.

131. E. Muthuswamy, J. Zhao, K. Tabatabaei, M. M. Amador, M. A. Holmes, F. E. Osterloh, and S. M. Kauzlarich. Thiol-capped germanium nanocrystals: Preparation and evidence for quantum size effects. *Chemistry of Materials*, 26(6):2138–2146, 2014.

132. A. Nozik. Quantum dot solar cells. *Physica E: Low-dimensional Systems and Nanostructures*, 14(1):115–120, 2002.

133. W. Liang, M. P. Shores, M. Bockrath, J. R. Long, and H. Park. Kondo resonance in a single-molecule transistor. *Nature*, 417(6890):725–729, 2002.

134. S. A. McDonald, G. Konstantatos, S. Zhang, P. W. Cyr, E. J. Klem, L. Levina, and E. H. Sargent. Solution-processed PbS quantum dot infrared photodetectors and photovoltaics. *Nature Materials*, 4(2):138–142, 2005.

135. E. L. Rosen, R. Buonsanti, A. Llordes, A. M. Sawvel, D. J. Milliron, and B. A. Helms. Exceptionally mild reactive stripping of native ligands from nanocrystal surfaces by using Meerwein's salt. *Angewandte Chemie International Edition*, 51(3):684–689, 2012.

136. A. Dong, X. Ye, J. Chen, Y. Kang, T. Gordon, J. M. Kikkawa, and C. B. Murray. A generalized ligand-exchange strategy enabling sequential surface functionalization of colloidal nanocrystals. *Journal of the American Chemical Society*, 133(4):998–1006, 2010.

137. T. Kazahaya and M. Hirose. Coordination number of doped boron atoms in photochemically-deposited amorphous silicon studied by x-ray photoelectron spectroscopy. *Japanese Journal of Applied Physics*, 25(1):L75–L77, 1986.

138. X. Pi, X. Chen, and D. Yang. First-principles study of 2.2 nm silicon nanocrystals doped with boron. *The Journal of Physical Chemistry C*, 115(20):9838–9843, 2011.

139. H. Sugimoto, M. Fujii, K. Imakita, S. Hayashi, and K. Akamatsu. Phosphorus and boron codoped colloidal silicon nanocrystals with inorganic atomic ligands. *The Journal of Physical Chemistry C*, 117(13):6807–6813, 2013.

140. E. J. W. Verwey and J. T. G. Overbeek. *Theory of the stability of lyophobic colloids*. Courier Dover Publications, 1999.

141. W. B. Russel, D. A. Saville, and W. R. Schowalter. *Colloidal dispersions*. Cambridge University Press, 1992.

142. H. C. Hamaker. The london–van der waals attraction between spherical particles. *Physica*, 4(10):1058–1072, 1937.

143. I.-E. Dzyaloshinskii, E. Lifshitz, and L.-P. Pitaevskii. The general theory of van der Waals forces. *Advances in Physics*, 10(38):165–209, 1961.

144. S. L. Carnie, D. Y. Chan, and J. Stankovich. Computation of forces between spherical colloidal particles: nonlinear poisson-boltzmann theory. *Journal of Colloid and Interface Science*, 165(1):116–128, 1994.

145. H. Ohshima and T. Kondo. Electrostatic double-layer interaction between two charged ion-penetrable spheres: An exactly solvable model. *Journal of Colloid and Interface Science*, 155(2):499–505, 1993.

146. S. Bhattacharjee, M. Elimelech, and M. Borkovec. Dlvo interaction between colloidal particles: beyond derjaguin's approximation. *Croatica Chemica Acta*, 71:883–903, 1998.

147. F. M. Fowkes, H. Jinnai, M. A. Mostafa, F. W. Anderson, and R. J. Moore. Mechanism of electric charging of particles in nonaqueous liquids. *Colloids Surface Reprographic Technology*, pages 307–324, 1982.

148. H. Kruyt, G. Jonker, and J. Overbeek. *Colloid Science. Vol. 1. Irreversible Systems*. Elsevier Publishing Co., 1952.

149. H. Reerink and J. T. G. Overbeek. The rate of coagulation as a measure of the stability of silver iodide sols. *Discussions of the Faraday Society*, 18:74–84, 1954.

150. L. Bergström. Hamaker constants of inorganic materials. *Advances in colloid and interface science*, 70:125–169, 1997.

151. C. J. Van Oss. *Interfacial forces in aqueous media*. CRC press, 2006.

152. B. Selin Tosun, B. D. Chernomordik, A. A. Gunawan, B. Williams, K. Andre Mkhoyan, L. F. Francis, and E. S. Aydil. Cu_2ZnSnS_4 nanocrystal dispersions in polar liquids. *Chemical Communications*, 49:3549–3551, 2013.

153. U. Mayer, V. Gutmann, and W. Gerger. The acceptor number—a quantitative empirical parameter for the electrophilic properties of solvents. *Monatshefte für Chemie*, 106(6):1235–1257, 1975.

154. M. J. Kamlet, J. L. M. Abboud, M. H. Abraham, and R. Taft. Linear solvation energy relationships. 23. a comprehensive collection of the solvatochromic parameters, π^*, α, and β, and some methods for simplifying the generalized solvatochromic equation. *The Journal of Organic Chemistry*, 48(17):2877–2887, 1983.

155. B. V. Velamakanni, J. C. Chang, F. F. Lange, and D. S. Pearson. New method for efficient colloidal particle packing via modulation of repulsive lubricating hydration forces. *Langmuir*, 6(7):1323–1325, 1990.

156. W. B. Jensen. *The Lewis acid-base concepts: an overview*. Wiley New York, 1980.

157. N. V. Churaev and B. Derjaguin. Inclusion of structural forces in the theory of stability of colloids and films. *Journal of Colloid and Interface Science*, 103(2):542–553, 1985.

158. D. W. Thompson and I. R. Collins. Electrolyte-induced aggregation of gold particles on solid surfaces. *Journal of Colloid and Interface Science*, 163(2):347–354, 1994.

159. J. M. Peula-García, J. L. Ortega-Vinuesa, and D. Bastos-González. Inversion of Hofmeister series by changing the surface of colloidal particles from hydrophobic to hydrophilic. *The Journal of Physical Chemistry C*, 114(25):11133–11139, 2010.

160. C. Calero, J. Faraudo, and D. Bastos-González. Interaction of monovalent ions with hydrophobic and hydrophilic colloids: Charge inversion and ionic specificity. *Journal of the American Chemical Society*, 133(38):15025–15035, 2011.

161. S. Marcelja. Hydration in electrical double layers. *Nature*, 385:689–690, 1997.

162. J. Israelachvili and H. Wennerström. Role of hydration and water structure in biological and colloidal interactions. *Nature*, 379:219–225, 1996.

163. A. Nozik, M. Beard, J. Luther, M. Law, R. Ellingson, and J. Johnson. Semiconductor quantum dots and quantum dot arrays and applications of multiple exciton generation to third-generation photovoltaic solar cells. *Chemical Reviews*, 110(11):6873, 2010.

164. A. Pandey and P. Guyot-Sionnest. Hot electron extraction from colloidal quantum dots. *The Journal of Physical Chemistry Letters*, 1(1):45–47, 2009.

165. S. Prabakar, A. Shiohara, S. Hanada, K. Fujioka, K. Yamamoto, and R. D. Tilley. Size controlled synthesis of germanium nanocrystals by hydride reducing agents and their biological applications. *Chemistry of Materials*, 22(2):482–486, 2009.

166. Y. Kanemitsu, H. Uto, Y. Masumoto, and Y. Maeda. On the origin of visible photoluminescence in nanometer–size Ge crystallites. *Applied Physics Letters*, 61(18):2187–2189, 1992.

167. K. Min, K. Shcheglov, C. Yang, H. A. Atwater, M. Brongersma, and A. Polman. The role of quantum-confined excitons vs defects in the visible luminescence of SiO_2 films containing ge nanocrystals. *Applied Physics Letters*, 68(18):2511–2513, 1996.

168. M. Zacharias and P. Fauchet. Blue luminescence in films containing Ge and GeO_2 nanocrystals: The role of defects. *Applied Physics Letters*, 71(3):380–382, 1997.

169. D. Knapp, B. S. Brunschwig, and N. S. Lewis. Chemical, electronic, and electrical properties of alkylated ge (111) surfaces. *The Journal of Physical Chemistry C*, 114(28):12300–12307, 2010.

170. T. Hanrath and B. A. Korgel. Chemical surface passivation of Ge nanowires. *Journal of the American Chemical Society*, 126(47):15466–15472, 2004.

171. G. Collins and J. D. Holmes. Chemical functionalisation of silicon and germanium nanowires. *Journal of Materials Chemistry*, 21(30):11052–11069, 2011.

172. G. W. Cullen, J. A. Amick, and D. Gerlich. The stabilization of germanium surfaces by ethylation i. chemical treatment. *Journal of The Electrochemical Society*, 109(2):124–127, 1962.

173. D. Wang and H. Dai. Germanium nanowires: From synthesis, surface chemistry, and assembly to devices. *Applied Physics A*, 85(3):217–225, 2006.

174. B. R. Taylor, S. M. Kauzlarich, H. W. H. Lee, and G. R. Delgado. Solution synthesis of germanium nanocrystals demonstrating quantum confinement. *Chemistry of Materials*, 10(1):22–24, 1998.

175. H. W. Chiu and S. M. Kauzlarich. Investigation of reaction conditions for optimal germanium nanoparticle production by a simple reduction route. *Chemistry of Materials*, 18(4):1023–1028, 2006.

176. R. Fuchs, L. O. Moore, D. Miles, and H. Gilman. Some symmetrical tetraalkyl-and tetraaralkyl-germanes. *The Journal of Organic Chemistry*, 21(10):1113–1117, 1956.

177. R. Boukherroub, S. Morin, F. Bensebaa, and D. Wayner. New synthetic routes to alkyl monolayers on the Si (111) surface. *Langmuir*, 15(11):3831–3835, 1999.

178. S. Fellah, A. Teyssot, F. Ozanam, J.-N. Chazalviel, J. Vigneron, and A. Etcheberry. Kinetics of electrochemical derivatization of the silicon surface by Grignards. *Langmuir*, 18(15):5851–5860, 2002.

179. N. A. Hill, S. Pokrant, and A. J. Hill. Optical properties of Si-Ge semiconductor nano-onions. *The Journal of Physical Chemistry B*, 103(16):3156–3161, 1999.

180. J. R. Heath, J. J. Shiang, and A. Alivisatos. Germanium quantum dots: Optical properties and synthesis. *The Journal of Chemical Physics*, 101:1607, 1994.

181. M. L. Cohen and J. R. Chelikowsky. *Electronic structure and optical properties of semiconductors*. Springer, New York, 1989.

182. Z. Holman and U. R. Kortshagen. A flexible method for depositing dense nanocrystal thin films: Impaction of germanium nanocrystals. *Nanotechnology*, 21(33):335302, 2010.

183. M. C. Beard, K. P. Knutsen, P. Yu, J. M. Luther, Q. Song, W. K. Metzger, R. J. Ellingson, and A. J. Nozik. Multiple exciton generation in colloidal silicon nanocrystals. *Nano Letters*, 7(8):2506–2512, 2007.

Appendix A

Copyright permissions